Ph.D Thesis

Experimental study and hydrodynamical description of relativistic heavy ion collisions:

Showers of forward scattered particles in the PHENIX Zero Degree Calorimeter and a hydrodynamical description of central heavy ion collisions

by **András Ster**

Supervisor: Dr. Tamás Csörgő

Eötvös Loránd University Faculty of Science
Doctorate School of Physics
Head: Dr. Horváth Zalán

Particle Physics and Astronomy Program
Head: Dr. Csikor Ferenc

MTA KFKI Reasearch Institute for Particle and Nuclear Physics
Department of Theoretical Physics
Budapest, 2007

Contents

Chapter 1

Introduction

The physics of relativistic heavy ion collisions is currently one of the most important reasearch areas of high energy physics both from theoretical and experimental aspects. The main goal of such researches is the experimental reproduction and identification of the new phase or maybe new phases of the strongly interacting matter. One of the new phases predicted by many theorists is the quark-gluon plasma (QGP), where the constituents of hadrons (e.g. protons or neutrons) the quarks and gluons exist like quasi free particles after breaking out from the confined state caused by the strong interaction. Our Universe might also have existed in such a phase a few microseconds right after the Big Bang. This cosmological connection may also be the reason for the exceptional public interest for this research.

This expectetion is based on QCD, the quantum-field theory of strong interactions predicts that the interactions among quarks is asymptotically free. It means, the closer they get to each-other, the weaker the force between them is, i.e. if the quarks get very close to each-other then they behave like free particles. For the discovery of the asymptotic freedom of the strong interactions, D. Gross, D. Politzer and F. Wilczek won the Nobel Prize in Physics in 2004. In spite of such strong expectations, the evidence for a new phase of the strongly interacting matter can be provided by experiments. Therefore, it is highly important to describe and to interpret the experimental results within a theoretical framework in this field of science.

In experiments the largest nuclei are accelerated to the highest presently available energies, so that they collide and large number of protons and neutrons (or their constituents the quarks and gluons) be pressed very close to each-other. The technological development made it possible, that in these heavy ion accelerators heavier ions with large mass number can be accelerated even to the 99.99% of the speeed of light. Having these fast heavy ions collide head on head extremely high energy and matter density can be achieved. Under natural circumstances, such a phase could have existed just a few seconds after the Big Bang. Namely, at the Relativistic Heavy Ion Collider (RHIC) at the Brookhaven National Laboratory in frontal Au+Au collisions physicists can produce minimum an energy density of 5 GeV/fm^3 about 1 fm/c in proper time after the reaction takes place [Adc04, Ars04, Bac04, Ada05]. The latest estimations suggest that 10 GeV/fm^3 is the realistic value [Csö07b]. It is much higher then the 1 GeV/fm^3 energy density theoretically needed to make quarks liberated from their hadronic prisons [Adc04, Ars04, Bac04, Ada05].

1.1 Experiments

Currently, there are two major international experimental research centers involved in such projects: RHIC in the USA and the Large Hadron Collider (LHC) at the European Organization for Nuclear Research (CERN) in Geneva, Switzerland.

At RHIC, the center of mass energy of nucleon pairs reaches the value of $\sqrt{s_{NN}} = 200$ GeV. This is more than ten times higher then the corresponding energy of earlier, fixed target Pb+Pb experiments at CERN SPS. While RHIC has been functioning since 2000, LHC is expected to start from 2007. The planned 14 TeV center of mass energy in $p + p$ collisions will probably be reached in 2008. Also, Pb+Pb collisions of $\sqrt{s_{NN}} = 5.5$ TeV energy in the LHC accelerator complex are expected to start from 2008.

1.2 Theories

Many scientists are surprised that the most successful interpretation of the data of Au+Au collisions at RHIC sofar derives from hydrodynamical description. This is the basis of our statement in 2005: in these reactions, a new type of phase is created, that behaves like a perfect fluid [Adc04, Ars04, Bac04, Ada05]. The Buda-Lund hydrodynamical model [Csö95a], partially developed at KFKI RMKI, Hungary, in a Swedish-Hungarian collaboration, has proved to be able to get detailed information from the final states of hadrons about the collective behaviour of the new matter created in high energy heavy ion collisions. For example, such information is the distribution of the temperature within the reaction zone or how large the volume is in space and time. The model gives predictions for the momentum distribution of the hadrons that freeze-out from the hot matter. Also, it is able to calculate their momentum correlations. All the predictions can be tested against experimental data. From such comparisions we could determine the characteristics of the new matter created in Au+Au collisions at RHIC. Such analyses help us answer the question whether a new type of phase of the strongly interacting matter, i.e. quark-gluon plasma has been created or not or another new phase has appeared in the collisions [Rio06].

Chapter 2

Experimental setup

2.1 Introduction to RHIC and PHENIX

2.1.1 Relativistic Heavy Ion Collider - RHIC

RHIC is located in Brookhaven National Laboratory, Upton, New York, Fig. 2.1. It is capable of accelerating a wide variety of nuclei and ions from protons to Au nuclei up to 200 GeV energy per nucleon pairs using two independent rings and colliding them at six interaction points. The design luminosities are 2 x $10^{26} cm^{-2} sec^{-1}$ for Au beams and 2 x $10^{31} cm^{-2} sec^{-1}$ for proton beams (2 x $10^{31} cm^{-2} sec^{-1}$ in an enhanced mode) at the top energy. RHIC also has a capability of accelerating polarized protons.

In Table 2.1, a comprihensive overview is given about the historical performance of the RHIC accelerator complex during the data taking runs.

Figure 2.1 shows an aerial view of the RHIC accelerator complex. The route for the acceleration is shown on Fig. 2.2: starting from the source, the ions or the protons are accelerated through Linac, Booster and AGS then injected into both rings of RHIC, whose circumference is 3.834 km. The "Blue" ring runs clockwise and the "Yellow" ring runs counterclockwise. There are currently 120 bunch buckets in each ring whose interval is 106 nsec (or 9.4 MHz frequency). Experiments are located at the interaction points where two bunches in each ring collide head on. There are six interaction points called 12, 2, 4, 6, 8, and 10 o'clock respectively starting from the north

Figure 2.1: Location of the laboratory in Long Island and the RHIC accelerator complex

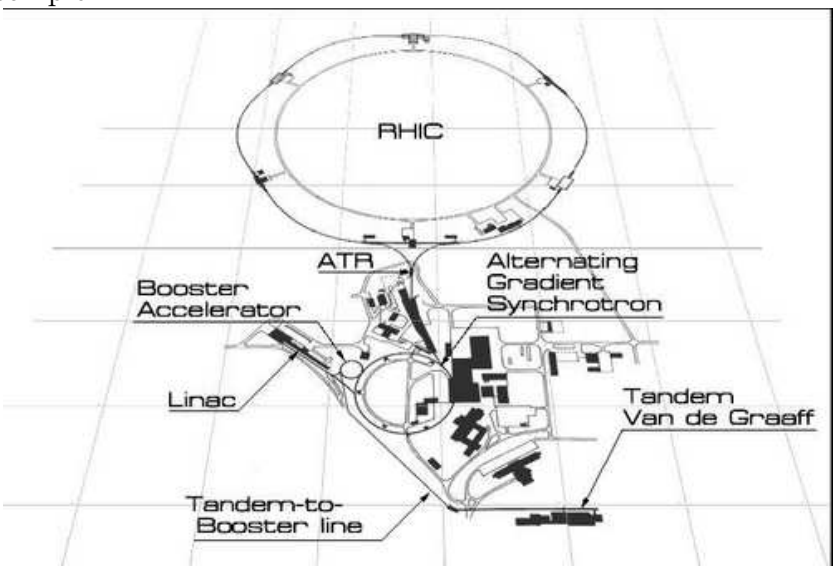

Figure 2.2: Elements of RHIC acceleration

Table 2.1: Run1 - Run6 capsule history

Run	Year	Species	$\sqrt{s}$ GeV	$\int$ Ldt	NTot	p-p Equivalent	Data Size
01	2000	Au+Au	130	1 μb^{-1}	10M	0.04 pb^{-1}	3 TB
02	2001/2002	Au+Au	200	24 μb^{-1}	170M	1.0 pb^{-1}	10 TB
		p+p	200	0.15 pb^{-1}	3.7G	0.15 pb^{-1}	20 TB
03	2002/2003	d+Au	200	2.74 nb^{-1}	5.5G	1.1 pb^{-1}	46 TB
		p+p	200	0.35 pb^{-1}	6.6G	0.35 pb^{-1}	35 TB
04	2003/2004	Au+Au	200	241 μb^{-1}	1.5G	10.0 pb^{-1}	270 TB
		Au+Au	62	9 μb^{-1}	58M	0.36 pb^{-1}	10 TB
05	2004/2005	Cu+Cu	200	3 nb^{-1}	8.6G	11.9 pb^{-1}	173 TB
		Cu+Cu	62	0.19 nb^{-1}	0.4G	0.8 pb^{-1}	48 TB
		Cu+Cu	22.5	2.7 μb^{-1}	9M	0.01 pb^{-1}	1 TB
		p+p	200	3.8 pb^{-1}	85B	3.8 pb^{-1}	262 TB
06	2006	p+p	200	10.7 pb^{-1}	230B	10.7 pb^{-1}	310 TB
		p+p	62	0.1 pb^{-1}	28B	0.1 pb^{-1}	25 TB

and going clockwise. There are 4 experiments located at the interaction points.

Each experiment has its unique feature. STAR and PHENIX are the largest experiments at RHIC each with more than 400 collaborators. STAR (Solenoid Tracker At RHIC) tracks and identifes charged particles with a time projection chamber covering a large solid angle. PHENIX (Pioneering High Energy Nuclear and Ion eXperiment) was designed to measure hadrons, leptons and photons in both high multiplicity and high rate environments. BRAHMS measures hadrons over wide ranges of rapidity and momentum using two magnetic spectrometers. PHOBOS consists of a large number of silicon detectors surrounding the interaction region to measure charged particle multiplicities even in the most central Au+Au collisions. At the present, BRAHMS and PHOBOS have finished their data taking program. PHENIX and STAR keep on measuring rare penetrating probes and continue their upgrading and data taking programs.

Common to all experiments at RHIC are two Zero Degree Calorimeters (ZDC) positioned along the beam axis. The ZDCs measure the event rate produced in RHIC. They also serve as event triggers for the experiments.

2.1.2 PHENIX Collaboration

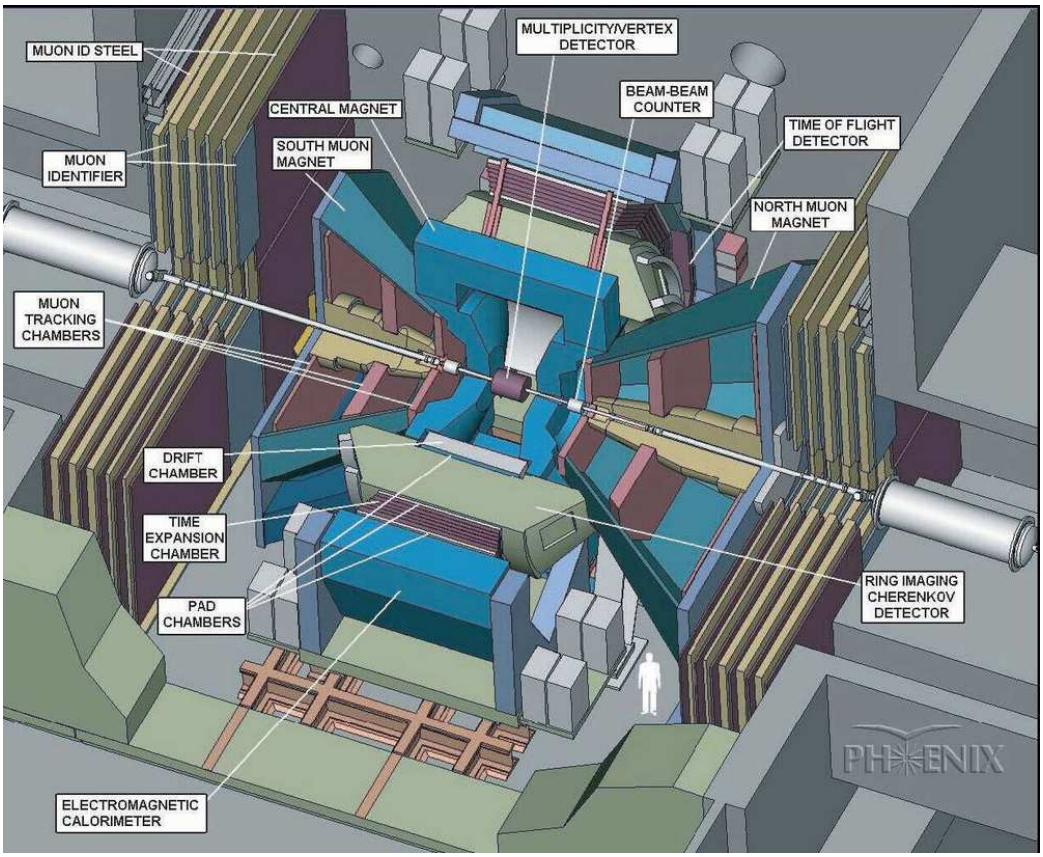

Figure 2.3: PHENIX detector

PHENIX is one of the largest experiments at RHIC, located at the 8-o'clock interaction region. Figure 2.3 shows a schematic view of the PHENIX experiment. PHENIX was designed to measure leptons, photons and hadrons in both high-multiplicity heavy-ion collisions and high event-rate p+p collisions. There are two independent spectrometers in PHENIX which cover different pseudo-rapidity regions. Two Central Arms, East and West Arms, cover the pseudo-rapidity range of $|\eta| < 0.35$ with a quarter azimuth for each Arm and measure electrons, photons and hadrons. Two Muon Arms, North and South Arms, cover $1.2 < \eta < 2.4$ and $-2.2 < \eta < -1.2$, respectively, with a full azimuth and measure muons.

There are three magnets in PHENIX. The Central Magnet provides an axial magnetic field for the Central Arms while two Muon Magnets produce a radial field for each Muon Arm.

The coordinate system in PHENIX is defined relative to the beam axis which passes through the center called z. The xyz axes follow the right-hand rule with the positive x axis pointing into the West arm and the positive z axis pointing toward North. The origin in PHENIX is the event vertex position which does not precisely coincide with the symmetry axis of the central arm detectors.

Subdetectors of PHENIX

The detectors of the PHENIX collaboration are maintained and operated by the representatives of the partcipant institutes. Their funcionalities are explained as follows:

Central Arm Detectors

These detectors are all positioned radially about the collision axis, extending from 2 m to 5 m.

Drift Chambers (DC)
They detect tracks of charged particles right after that traverse through the central arms.

Pad Chambers (PC)
They measure the position of charged particles with high precision. They are used in the global track reconstruction.

Ring Imaging Cherenkov Detector (RICH)
It identifes charged particles by Cherenkov radiation as they traverse the gas of the detector.

Time Expansion Chamber (TEC)
It measures the track positions of charged particles. It also identifies particles.

Time-of-Flight (TOF)
It is used for particle identification.

Electromagnetic Calorimeters (EMCal)
The measures the track positions and the energy of charged particles and photons. They identifies the photons and the charged particles. There are two types of the detectors: Lead scintillator (PbSc) and lead glass (PbGl). The detectors are positioned about 5 meters from the collision axis.

Muon Arm Detectors

Muon Tracker (MuTr)
It measures the track positions and the momentum of muons.

Muon Identifier (MuID)
Identifies muons.

Event Characterization Detectors

Beam-Beam Counters (BBC)
Two Beam-beam counters are located 1.4 m far away on both sides from the detector center along the beam axis. They detect charged particles produced in collisions. They are used to determine collision position and centrality. Starts the stopwatch for an event.

Zero Degree Calorimeters (ZDC)
Measures collision location and centrality.

Forward Calorimeters (FCal)
For deuteron+Au collisions, it can measure surviving neutrons and protons

from the original deuteron.

Multiplicity Vertex Detector (MVD)
This detector measures the multiplicity of charged particles. It is positioned close to the interaction point that allowis for measuring in broad pseudorapidity range. It helps measuring collision location.

Heavy Metal Detector

PHENIX Magnets
Bends charged particles so that their charge and momentum can be measured in both the central arm and the muon arm detectors.

2.2 Introduction to PHENIX ZDC and SMD detectors

2.2.1 The RHIC Zero Degree Calorimeter

The Zero Degree calorimeters (ZDC) are small transverse area hadron calorimeters located downstream of the DX dipole magnets in each of the Heavy Ion Experiments at RHIC, Fig. 2.4. The detectors measure neutral energy within a 2 mrad cone about the beam direction (since charged particles are swept away by the DX magnet). The actual detector location is 18m from the interaction point and the horizontal acceptance is to +/- 5cms. The design is based on the requirements for Au-Au runs but the dettectors are also used in p-p and d-Au runs. The detectors serve two roles: The energy measurement basically counts the number of free "spectator" neutrons. This is used for event-by-event characterization(usually in conjuction with the BBC). Also coincidence signals from detectors on either side of the interaction region are used for luminosity monitoring. During 200 GeV Au-Au running (ie in Run IV) the ZDC coincidence rate has an effective cross section of 10.4 barns (with an uncertainty of about 5The energy scale of the ZDC is determined from the inclusive spectrum obtained with RHIC data. You can usually make

out the first few peaks (ie 1n and 2n, etc) in this spectrum which gives you the best possible Energy calibration. However we try to "dead-reckon" the relative gains of the 3 PMT's- each measuring successive depth segments in the calorimeter- using cosmic ray data. Typically this has been succesful and the width of the 1-n peak is about 20The ZDC timing resolution is 100 psec depending on the electronics setup, empirical slewing corrections.. (in other words depending on which experiment you're in). Since you measure time in 2 ZDC's, on either side of the IR, you can derive 2 quantities from them- the vertex position and the event time.

The first ZDC module was installed in the RHIC tunnel on March 19th '99.

2.2.2 PHENIX ZDC Shower Maximum Detector

The PHENIX Shower Max Detectors(SMD) are layers of position sensitive hodoscopes sandwiched between the first and second module of the ZDC's. Since a ZDC module is 2 hadronic interaction lengths deep, the actual amplitude measured in the Shower Max detector will fluctuate from one shower to another (but less so in a typical event with many neutrons). The purpose of the SMD is to measure the centroid of showers in the ZDC in 2 coordinates- x and y. The first SMD layer has 21 strips of 0.5 cm *0.5 cm scintillators each with wavelength shifter fiber readout. Groups of 3 fibers are read out by a single channel of a multi-anode PMT. So the total width of the SMD, 10.5 cms, is subdivided into 7 samples. In d-Au runs (Run-3) the horizontal measurement accuracy of the centroid was about 0.1 to 0.2 mm and correlated with accelerator instrumentation beam position. Similarly, the vertical coordinate has 8 elements of 4 scintillator strips.

The ZDC's are described in the following section that is based on the NIM article [Adl00].

Some of the design considerations are based on the NA49 measurement in which we tried to understand the role of free neutron measurement as opposed the more traditional fixed target implementation.

Figure 2.4: ZDC installed in the experimental area

2.3 Design and construction of ZDC

2.3.1 Introduction

High Energy collisions of nuclei usually lead to the emission of evaporation neutrons from both "beam" and "target" nuclei. At the RHIC heavy ion collider with 100GeV/u beam energy, evaporation neutrons diverge by less than 2 milliradians from the beam axis. Neutral beam fragments can be detected downstream of RHIC ion collisions (and a large aperture Accelerator dipole magnet) if $\theta \leq 4$ mr but charged fragments in the same angular range are usually too close to the beam trajectory. In this 'zero degree' region produced particles and other secondaries deposit negligible energy when compared with that of beam fragmentation neutrons.

The purpose of the RHIC zero degree calorimeters (ZDC's) is to detect neutrons emitted within this cone along both beam directions and measure their total energy (from which multiplicity can be calculated). The ZDC coincidence of the 2 beam directions is a minimal bias selection of heavy ion collisions. This makes it useful as an event trigger and a luminosity monitor and for this reason identical detectors were built for all 4 RHIC experiments. The neutron multiplicity is also known to be correlated with event geometry and will be used to measure collision centrality in mutual beam interactions.

2.3.2 Design Goals

The RHIC ZDC's are hadron calorimeters. Their longitudinal segmentation ($2\ \lambda_I$, $50X_0$) is determined by practical, mechanical considerations. Electromagnetic energy emission into this region is predicted to be negligible so this measurement is not emphasized in the design. Since the spatial distribution of neutrons emitted in the fragmentation region carries only limited information about the collision, the calorimeters are built without transverse segmentation.

The Forward Energy resolution goal was determined by the need to cleanly resolve the single neutron peak in peripheral nuclear collisions. The

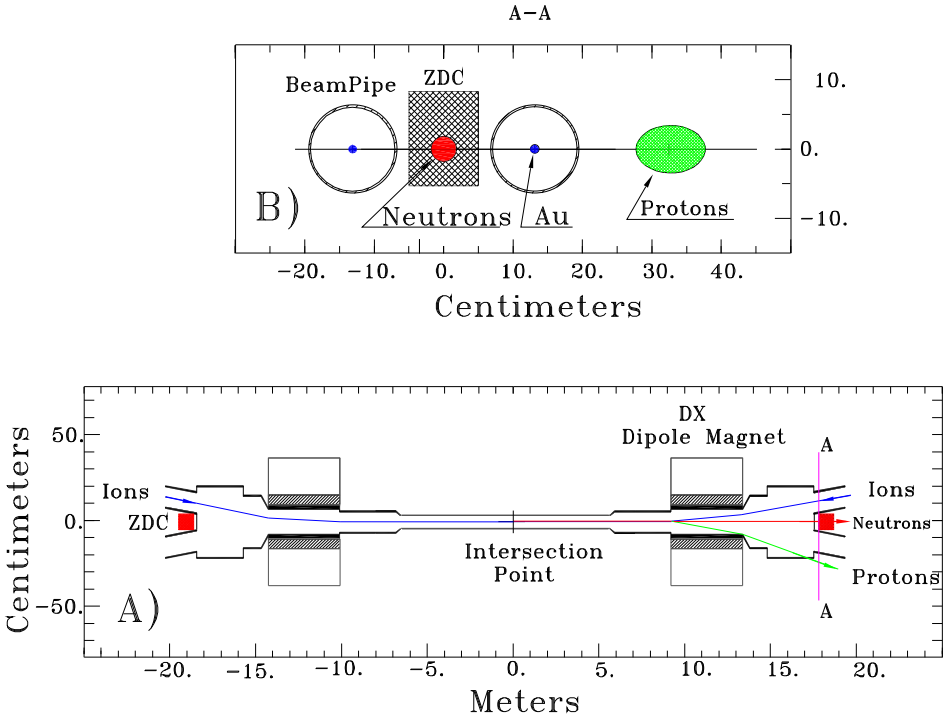

Figure 2.5: Plan view of the collision region and (section A-A) "beam's eye" view of the zdc location indicating deflection of protons and charged fragments (with Z/A$\sim$ 1 downstream of the "DX" Dipole magnet.

natural energy spread of emitted single neutrons being approximately 10% a resolution of$\frac{\sigma_E}{E} \leq 20\%$ at E_n= 100 GeVappeared reasonable.

The limited available space between the RHIC beams at the ZDC location imposes the most stringent constraint on the calorimeter design. As can be seen from Figure 2.5, the total width of the calorimeters is only cannot exceed 10 cm (equal to 1 nuclear interaction length (Λ_I) in tungsten). The ZDC's were designed to minimize the loss in energy resolution due to shower leakage, which can cause fluctuation in measured shower energy through dependence on position of impact and random fluctuations in shower development.

Finally, the ZDC's are required to withstand a dose of $\sim 10^5$ rad., which is the expected exposure during several years of RHIC operation.

2.3.3 Simulations

Simulations were performed for shower development, light production and transport in the optical components using Geant 3.21 for 2 basic sampling calorimeter designs:

1. Pb absorber with scintillator sampling
2. Pb, Cu or W absorber, each with undoped fiber optical ribbons in the sampling layer

The ZDC sampling technique which was adopted for this project, is sensitive to Cherenkov light produced by charged shower secondaries in a commercial, PMMA based communication grade optical fiber with characteristics given in a single free parameter was used to match the (wavelength dependent) optical fiber attenuation coefficient and photomultiplier quantum efficiency to the observed signal from testbeam μ 's. Hadronic shower simulation is based on Geisha with a low energy cutoff of 0.5 MeV on electrons and photons and 1 MeV on hadrons.

The fiber sampling layers, in all cases, consist of a single ribbon of 0.5mm diameter fibers. An orientation of 45^o relative to the incident beam direction was chosen which roughly coincides with the Cherenkov angle of β=1

Table 2.2: Mechanical parameters of the ZDC's

	Absorber	Space for fibers	Modules/Layers
Prototype W-ZDC	Tungsten (100x150x5 mm^3)	1.0 mm	$4(8\lambda_I;218X_0)$ 27
Prototype Cu-ZDC	Copper (100x150x10 mm^3)	1.0 mm	$8(7.5\lambda_I;79X_0)$ 10
Production ZDC	Tungsten alloy (100x187x5 mm^3)	1.4 mm	$3(5.1\lambda_I;149X_0)$ 27

Table 2.3: Characteristics of the fiber ribbon material. NA = 0.50

	Outer Diam	Material/Index
Core	0.45 mm	PMMA/1.49
Cladding	0.50	fluorine doped/1.40
Surface Prep	0.60	White Silicone Rubber/ EMA

particles in PMMA. PMMA fibers are readily available with a numerical aperture(NA) of 0.5 (defined as the fractional solid angle which is transmitted in the fiber). This aperture corresponds to a maximum angle of 30^o. Quartz fibers generally have a smaller aperture.

In the simulations it was studied:

1. the effects of transverse shower leakage

2. energy resolution dependence on sampling frequency and photostatistics

3. dependence on fiber orientation

A radius of 5 cm (the maximum space allowable at the RHIC location) contains 75% of the shower signal in the case of a Pb/Scintillator calorimeter with 10mm(Pb) and 2.5mm(Scint) layers. The same dimension Pb calorimeter with Cherenkov sampling yields 91% containment. In general the Cherenkov technique with Pb absorber achieves a given level of containment with a factor of 2 smaller radius than with scintillator.

Changing from Pb to W absorber yields almost another a factor of 2 reduction in containment radius. On the other hand, reducing the fiber

numerical aperture in the sampling layer produces only a negligible change.

Cherenkov light Production and Capture

Because the optical fibers only transport Cherenkov light emitted nearly aligned with the fiber axis, this detector is most sensitive to charged particles which cross at approximately 45^o to the fiber axis. The lower energy shower component, which is more diffuse, is therefore suppressed.

This filtering effect is reduced by multiple coulomb scattering of electrons and by the increased path length traversed by particles with less than 45^o angle to the fiber direction.

The multiple coulomb scattering has a significant effect on the response to low energy electrons. The improved angular filtering that could be obtained with lower NA fibers is largely offset by this effect and the lower light yield which results from small aperture.

Relative response to electrons and hadrons

The response to beam energy (100 GeV) protons is a factor of 2 lower than for electrons of the same energy. In this sense, the design is extremely non-compensating. This lack of compensation is the dominant source of energy resolution of the calorimeter for 100 GeV protons since the response changes with fluctuations in the energy fraction carried by π^o's in the hadronic shower.

Linearity

In the application, where the calorimeter is used to count beam energy neutrons, linearity is not a design consideration. It is clear, while the response to electrons is linear with energy, the hadron response is not. Response to neutrons and protons approaches zero at low energies. Also, the response to muons, which is energy independent up to $\sim$ 100 GeV/c at which point radiative energy loss becomes significant. Cosmic ray and beam muons were used for detector pre-calibration.

Table 2.4: Calculated energy resolution of ZDC's

Absorber	PhEls per 100Gev	"e/h" ratio	Stochastic term(%)	Constant term(%)
W (2.5mm)	1036	1.79	69.6±7.9	10.1±0.7
W(5.0mm)	518	1.78	84.6±4.8	9.1±0.5
W(10mm)	256	1.78	92.4±8.2	8.8±0.6
Cu(10mm)	611	2.01	111.7±7.0	9.3±0.6
Pb(10mm)	422	1.80	91.0±8.9	9.5±0.6

Energy resolution

The role of the main components of the energy resolution is illustrated in Table 3, where simulated calorimeter response was fitted to 50–800 GeV proton induced showers to a stochastic plus a constant term. The results are a poor fit to a quadratic sum.

If it was to increase the sampling frequency from 1/2 to twice the design value of 1 per 5mm tungsten absorber there would be a negligible change in resolution at 100 GeV. This configuration would reduce the stochastic term due to photostatistics from 6 to 3% but leave the dominant resolution term, due to non-compensation, unchanged.

2.3.4 Module Construction

For 10 cm wide modules with 5mm absorber plates, a convenient longitudinal segmentation is 1 module per 2 nuclear interaction lengths of absorber. The total fiber area matches that of a standard 2″ PMT.

For the prototype W modules 2.5 mm thick cast plates were obtained from a Russian manufacturer and bonded them in pairs. For the production modules machined plates of tungsten alloy with threaded mounting holes were obtained from a US manufacturer. The thickness uniformity of the plates is ± 0.1mm.

The fiber ribbons were wound on a mandrill and then impregnated with a low viscosity white silicone rubber glue. The glue covers the active region of the fibers (200 mm) and protects the fiber surface in the region of the

fiber/absorber sandwich. The light guide section of the remaining fibers is treated with an extramural absorber to suppress cladding modes in the fiber. The fiber ends closest to the PMT are collected into an acrylic compression fitting and impregnated with epoxy (Bicron BC-600) . After the epoxy cured the fiber bundle was polished using a diamond tipped cutting tool on a milling machine.

The far end of the fibers were rough cut and left untreated. The optical simulations assume no reflection at this end.

3 fibers were removed at random from the ribbons in each module and coupled them to a single external optical connector for PMT gain monitoring. This allowed for stable optical connections of all modules in the calorimeter stack to a single light flasher and therefore reliable tracking of relative PMT gain.

The fiber ribbons were trimmed to different lengths depending on their positions along the module. Lengths were adjusted to compensate for the difference in arrival time between the front and back of the module. The length of the acrylic fibers was kept to a minimum because the disigners were concerned about additional light production in fibers outside the absorber region- primarilly due to shower leakage at the top of the calorimeter.

A 12-stage general purpose PMT (Hamamatsu R329-2) was selected and mounted it with a 0.5mm air gap from the fiber bundles. PMT's were selected for $< 6\%$ photocathode non-uniformity over the 39mm diameter area corresponding to the fiber bundle size. Linearity of the PMT/ voltage divider combination is also an important criterion for this project since the calorimeters will be used to measure up to 40 or so beam energy neutrons in collisions of gold ions.

2.3.5 Precalibration

All modules were tested for relative light yield using cosmic muons incident along the beam axis and a standard PMT with calibrated response. Very little variation ($< 10\%$) was observed among the 24 tungsten modules we

eventually installed for this project.

During testbeam operation trigger counters were also installed to select a small contamination of muons which were present in the proton beam. Muons traversing the full calorimeter were used to adjust relative gains of the 4 PMT's in the prototype calorimeter.

2.3.6 Testbeam performance

The calorimeters were mounted on a table with remote x-y (transverse to the beam) positioning in the CERN North area, downstream of experiment NA49. The beam size and position was defined to ± 1 cm using a 1cm square scintillation counter directly upstream of the table.

The main purpose of the beam test was to study the response and resolution of the calorimeter as a function of position.

The 100 and 160 GeV/c protons were selected using a beam Cherenkov counter. The beam energy spread was typically 1%. PMT current pulses were integrated and digitized using a standard commercial ADC (LRS 2249w).

2.3.7 Results

Figure 2.6 shows the measured lineshapes with 100 and 160 GeV incident protons. The energy scale is normalized using the 100 GeV point. The expected distributions based on Geant simulation. The distributions are well represented by a gaussian resolution function and the response is linear over this limited energy range.

The position scans show essentially uniform response to within 1cm of the calorimeter edge along the horizontal direction -in good agreement with simulation. In the vertical scans there is an abrupt increase in response near the upper edge of the modules. The simulation reproduces this edge effect. It can be traced to shower leakage into the fibers above the absorber.

In order to improve module uniformity in the "beam region" the height of the module was increased in the final production design from 10 cm to 13.6 cm.

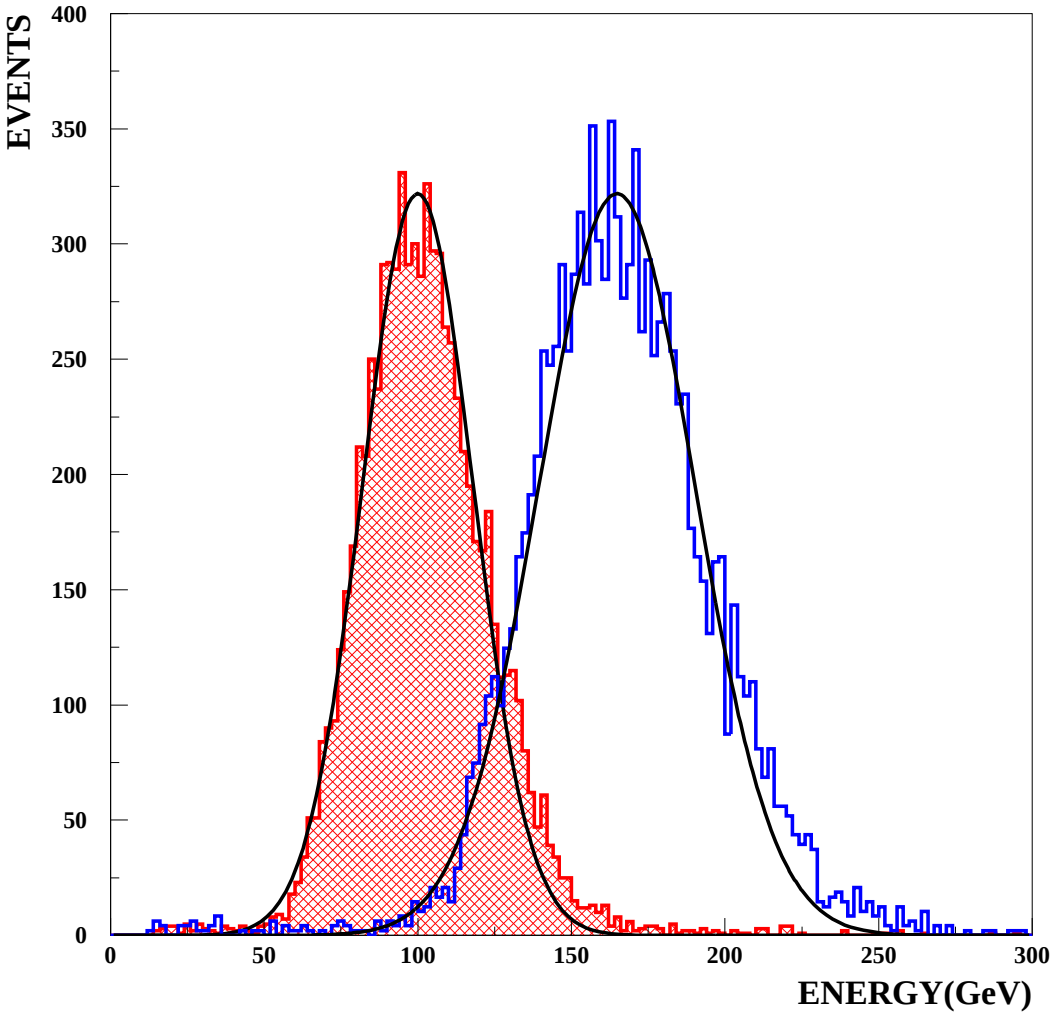

Figure 2.6: Tungsten ZDC response linshapes for 100 and 160 GeV incident protons.

The tungsten calorimeter uniformity and energy resolution were essentially unchanged when the energy deposited in the 4th module was neglected. Typically 1–2% of the energy is seen in this module. The energy resolution at 100 GeV changes from 17.6 to 19% when it is removed.

Part of the resolution of this calorimeter is due to the unequal response to electrons and photons relative to hadrons. This introduces a limiting resolution due to fluctuations in the shower composition (ie π^0 vs charged π).

The calorimeter is designed to measure beam energy neutrons incident at the front face (45^o to the fiber direction). A by-product of the directional response of the calorimeter is that it is relatively insensitive to background particles from "beam halo" and other sources. In order to demonstrate this suppression, the calorimeter was inverted in the testbeam (135^o to fiber direction).

Radiation tolerance

PMMA is not a particularly radiation tolerant plastic. It is known to lose transparency more readily than Polystyrene, for example. Earlier measurements on acrylic fibers showed about a factor of 2 decrease in attenuation length per 10^4 rad of gamma irradiation. Doses at the ZDC location in RHIC have been estimated at 10krad/yr. This is confirmed by dosimetry studies during RHIC commissioning.

The prototype modules were exposed to much higher integrated doses at a reactor. Approximately 2/3 of the total dose was due to gamma rays and the remainder was due to neutrons The module light output was measured using cosmic ray muons before and after 3 successive exposures up to a maximum of 700 krad (7000Gy).

2.3.8 Production Design Choices

The Copper and Tungsten modules both had adequate performance for the application. The tungsten module yields 1-2% better energy resolution at

100 GeV and slightly better flatness of response over the calorimeter face. It was chosen to proceed with the Tungsten module design primarily because of the $2 \times \Lambda_I$ modularity and other aspects of the mechanical design. Also the modules are more compact, which is an advantage given the limited space. The module height was increased in the production design to reduce shower leakage into the fiber bundles. Also the calorimeter depth was reduced from 8 to $6 \times \lambda_I$ since the shorter calorimeter gives essentially identical performance.

2.3.9 Discussion

Studies of the Cherenkov/fiber sampling technique with electrons and have been reported elsewhere. One device was built and operated in a fixed target experiment. Here, the first measurements iwere reported with a 45^o design hadron calorimeter and the first application of this method at a collider.

During the first colliding beam operation at RHIC, with Gold Ions accelerated to and stored at 65GeV/nucleon beam energy, the ZDC's have been used for beam tuning and as a trigger by the RHIC experiments. Figure 2.7 shows an online energy distribution from one of the calorimeters in the PHENIX experiment. The single neutron peak, which is seen clearly in this distribution, has been used to confirm the energy calibration of the calorimeters. For more details, see also refs.[Adl00, Chi02, Bal98, App98b].

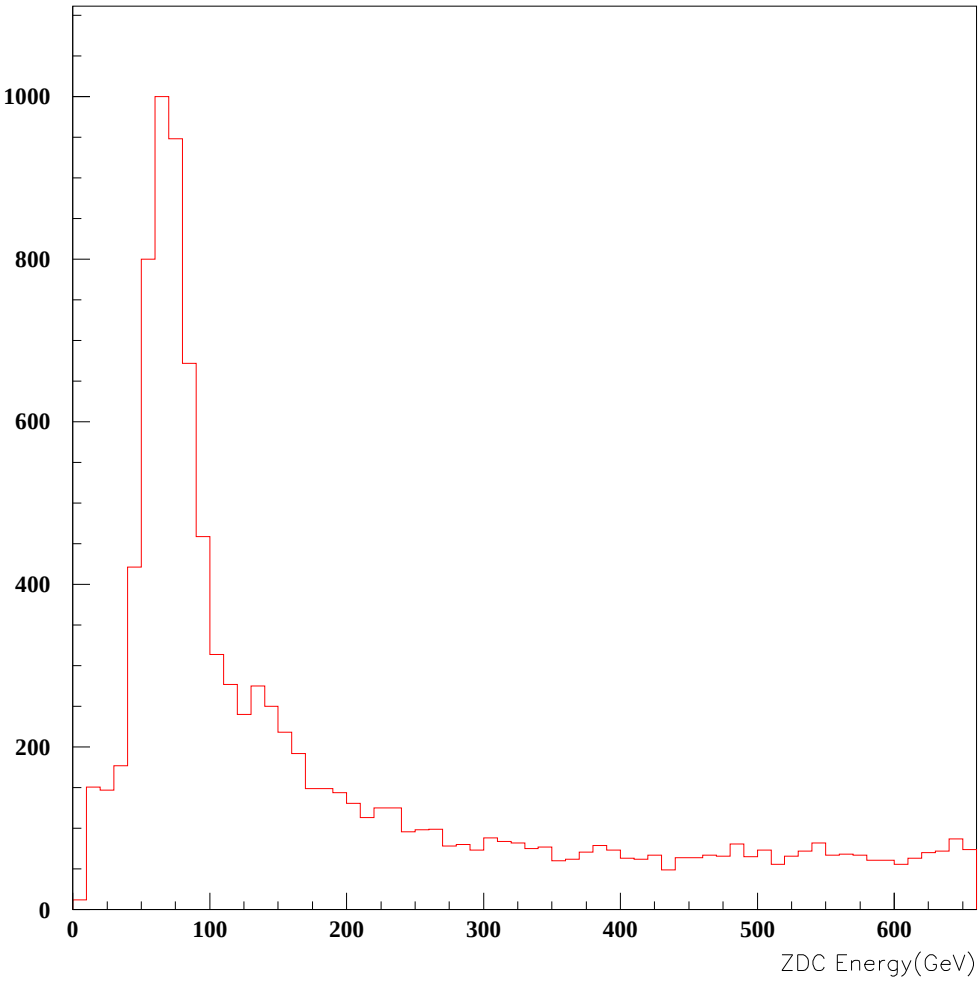

Figure 2.7: Online Zero Degree Calorimeter Energy Distribution obtained during RHIC colliding beam operation with beam energies of 65 GeV/nucleon.

2.4 My contribution: ZDC GEANT simulations for PHENIX

2.4.1 Introduction

Code for the Zero Degree Calorimeter detector has been implemented in the GEANT [Gea93] based PHENIX Integrated Simulation Application (PISA) software package. ZDC GEANT simulations aim at prediction of forward going energy distribution to determine centrality of $Au + Au$ and $Cu + Cu$ collisions at RHIC. The structure and the basic conceptions of the program are overviewed. Simulation results are presented and discussed. A guideline how to run the program under different PHENIX experimental setup conditions is provided.

2.4.2 The ZDC GEANT code

2.4.3 Construction of an ion fragmentation model

Based on a NA49 measurement specially setup for studying fragmentations after heavy ion collisions [App98] an ion fragmentation model has been developed for the simulations. This is necessary, because ZDC normally detects only neutral particles (mainly neutrons that do not participate in the reactions). Charged particles are swept away by the bendig magnets in front of them as show in Fig. 2.8. However, the neutrons associate with non-participating protons which essentially influences the number of neutrons penetrating the ZDC detector. Hence, the signal we detect strongly depend on the fragmentation picture we apply. Collision events were generated by a Hijing event generator code, whose output were modified in order to compose ion fragments from the individual non-participating nucleons according to the model.

The special model applied for the PHENIX ZDC detector simulations composes deuterons first until the number of the non-participant protons matches the number of 'extra' non-participant neutrons. The hint how many neutrons we should actually have reaching the ZDC can be obtained from

the NA49 publication. If, as usually, it is lower then tritiums are combined so that deuterons 'eat up' the pairless 'extra' non-participant neutrons. The details of the method and the first results were presented in a talk at a PHENIX Core Week 1999 December.

An additional trick had to be also applied in the method. Unfortunatelly, Geant is unable to track ions in material. To solve this difficult problem the particle bank with the composed fragments was modified so that deuterons had the name proton with double mass, tritiums with triple mass and so on, see Fig. 2.8..

2.4.4 Integration of the simulation code into PISA

Due to the large forward going energy the ZDC GEANT simulations had to be separated from the rest of the detectors. Therefore, usually by default, the ZDC code is switched off because it does not affect the signals of the other detectors. In contrary, the the whole equipment along with the beam pipeline may induce scattered secondary particles that might deposit their energies in the ZDCs. Also, the volume of the ZDCs are far much larger, therefore, tracking particles takes much more time. In summary: the large number of forward going particles, the energy they carry and the large volume to track particles make the detector simulations for the ZDCs extremely difficult (an example is shown in Fig. 2.9). In case of central Au+Au collisions, about 10 thousand particles are generated per event whose typical processing time is 20-30 minuits per event for the ZDCs.

2.4.5 Results

Fig. 2.10 show the results of about 1000 Au+Au minimum bias collisions. The ZDC signals were correlated with that of the BBC detector used also for centrality determination.

Fig. 2.12 show the consecutive 5% centrality classes as obtained from the GEANT simulations. This method is called the clockwise centrality selection. Other selections were also considered and are available for alternative

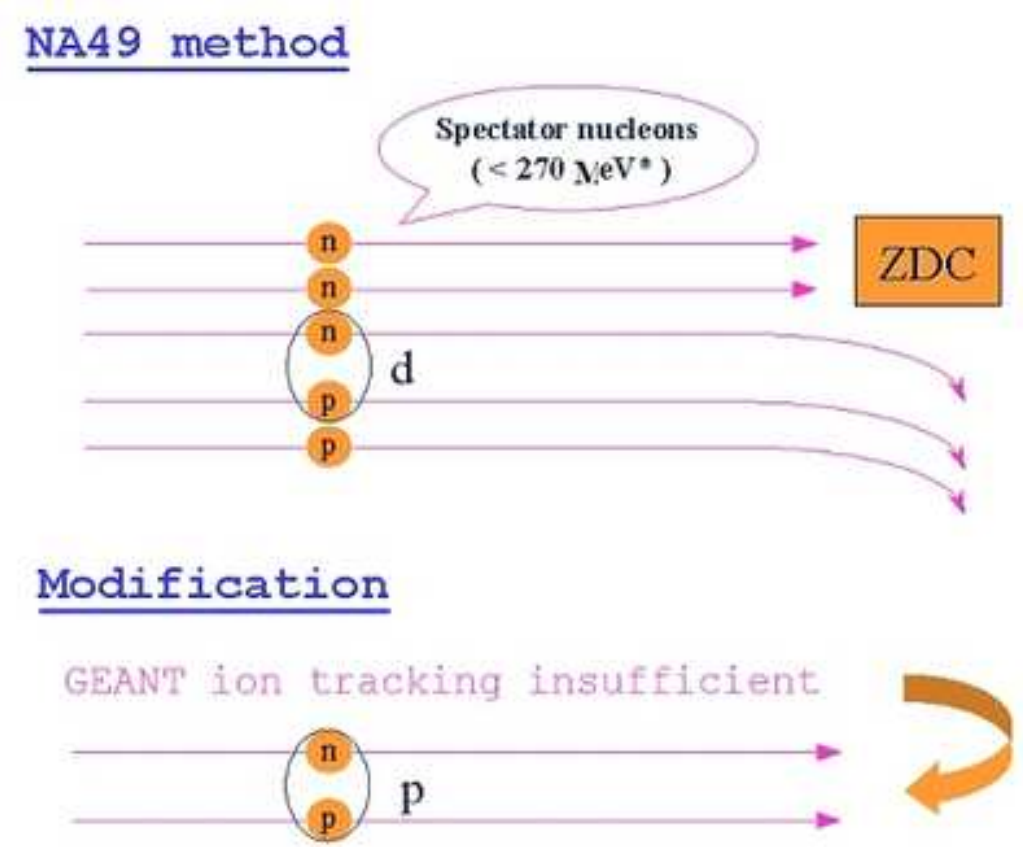

Figure 2.8: Composing ion fragments from non-participant nucleons. The figure shows how we get a deuteron. Na49 measurement data were used to estimate and extrapolate the number of non-participant neutrons penetrating the ZDC. Also, it is indicated how fragments were renamed so that their tracking was possible in GEANT.

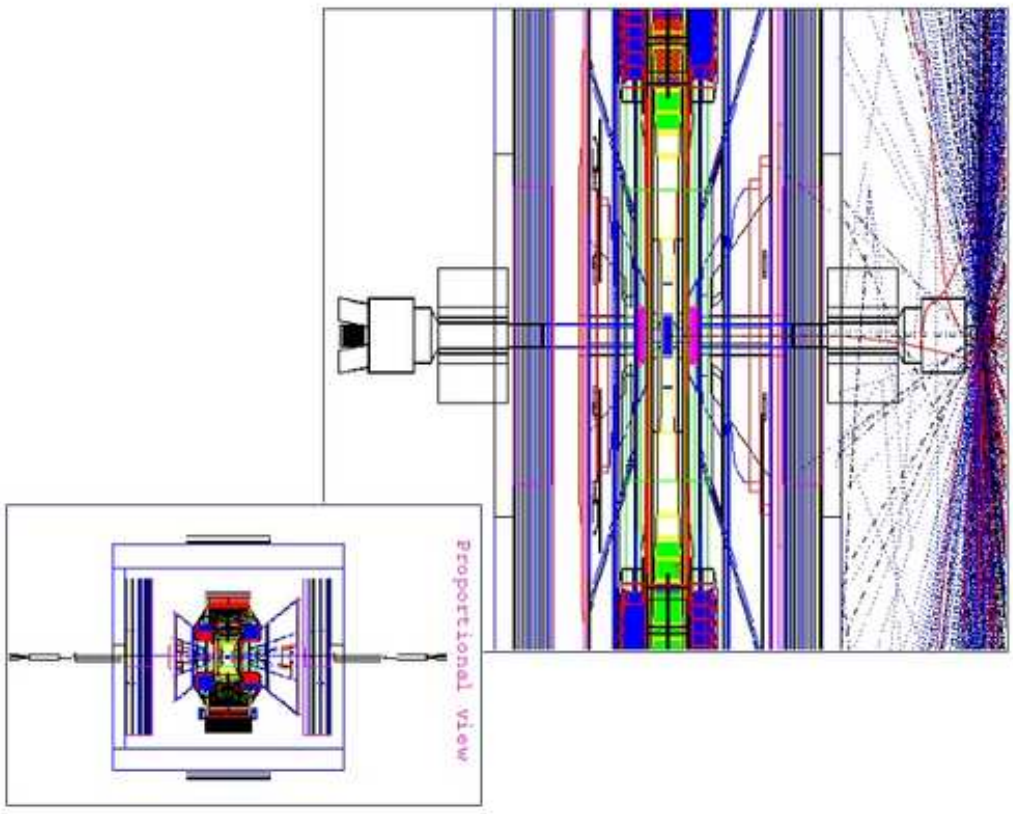

Figure 2.9: Example for the showers of particles in the ZDC. In this particular case one neutron with 100 GeV energy was shot to the detectror from the center. The larger figure was streched vertically so that the huge number of tracks are visible. In the left corner a proportional view of the PHENIX detector with all the subdetectors is shown as GEANT sees it.

analyses.

Further figures are show at the end of the next section where the usage of the program and its parameteres are explained in detail.

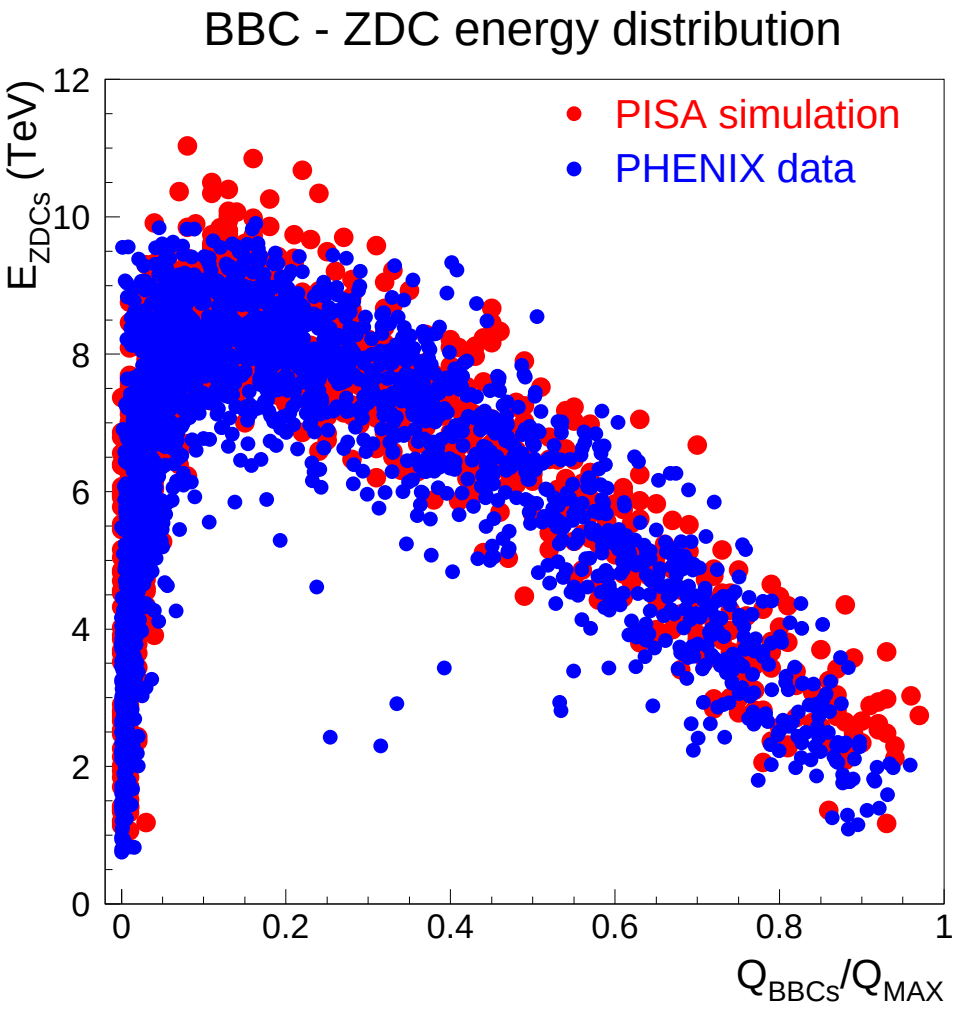

Figure 2.10: Measured and simulated ZDC vs BBC detector response data plotted onto each other for comparision. Simulation statistics of 1000 events were taken in 3 weeks in the PHENIX computer farm. The data represent Run2 Au+Au collisions

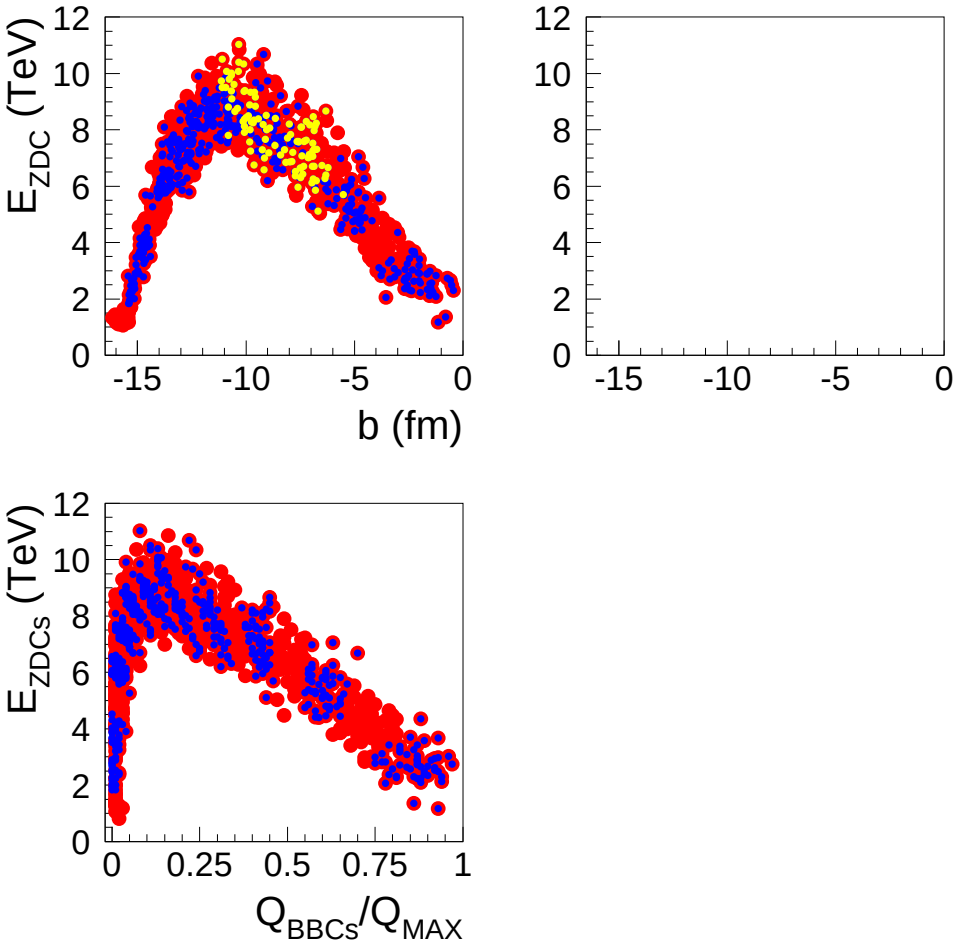

Figure 2.11: GEANT simulations of the ZDC. Below: centrality classes of 5% separated by colours according to the ZDC vs BBC detector response correlation. Above: the same centrality classes are indicated in function of the impact parameter 'b'. The impact parameters are provided by the event generator 'Hijing'. This way, we can assosiate the detector data and the frontality of the collisions.

2.4.6 How to run ZDC simulation in PISA

To make an executable program from the latest version of PISA carry out the following procedures and commands at your terminal prompt (>).

Downloading files

Download the latest version of PISA from the official site. Get your access permission to PISA code:

```
> klog <username>
> password:  <AFS user password>
```

Copy the the source and data files to your own directory. The example below creates the directory `simulation/pisa2000` in your current directory into which a complete copy of the PISA file system will be transferred.

```
> cvs co simulation/pisa2000
```

Making executable

In the directory `simulation/pisa2000` created above go into `lib` and give the command `gmake` (like the example below) to compile and link the files into one executable program.

```
> cd simulation/pisa2000/lib
> gmake -f pisa.mk
```

Before each run of the program set the enviroment variables, if not yet set. For example:

```
> setenv CERNLIB /cern/pro/lib
> setenv DISPLAY rxterm.rhic.bnl.gov:0.0
```

Running a simulation

Change to the working directory as shown below. Specify your computer platform and the program name (`linux` and pisa in this case). Before starting the program edit the input file (see in Appendix A) entries belonging to ZDC. Set 'HBOO' in `pisa.kumac` to get histograms like that in Appendix B

```
> cd simulation/pisa2000/wrk
> linux/pisa
```

Inputs

Input file parameters to set for ZDC

Files listed in the subsection titles can be found in the working directory `pisa2000/wrk` of PISA. Lines containing !!! comment indicate ZDC related information.

`gffgo.dat`

This is the standard Geant input file for PISA. Change the 2nd parameter of line 'GEOM' to set the experimental hall definitions (2 means ZDC is included). Set it to 0 if ZDC should be excluded from particle trackings (a smaller hall will be defined).

```
GEOM    1 2 0 0 0 0 0        !!!  INIT, ZDC, ....
AUTO    1                      !  GEANT automatic TMED parameter
SWIT    5 0 1 0 0 0 0 0 0      !  Compressed output
```

`pisa.kumac`

This is the standard kumac file for PISA. The last line belongs to ZDC. The example below shows a full setup configuration. Set any of the ON parameters to OFF if the corresponding detector should not be defined in Geant.

Set the 'HBOO' parameter of ZDC to ' ' if hbooking is not required during the simulation (PISA creates a separate hbook file `gintphnx.hbk` at the end of run). The last parameter in the ZDC line defines the magnetic field of the DX magnets in Tesla. Currently 1 fragmentation model is implemented in the program that is represented by the value 'FRG1' of the 6th parameter.

```
   * Random number seeds
   *
   RNDM 001 0
   *
   * Tracking thresholds
   *
   CUTS  .001 .001 .010 .010 .010 .001 .001 1.e+4 1.e+4 .010 4.e-7
   *
   FOUT 'phnx.dat.cZ'              ! Name of output hits file
   FPAR 'phnx.par'                 !  Namelist parameter file for
geometry
   STEE 'KINE' 'HITS' 'DIGI' 'JXYZ'! Output data structure control
   DOUT 'DIGI'                     ! Output data structure control
   MAGF 'QUAD' 1.00 0001 0.  0.  0.    !  Magnetic field map control
   GEOP 'PIPE'
   ANNI  1                         !  GEANT for annihilation on
   BREM  1                         !  GEANT for bremsstrahlung on
   COMP  1                         !  GEANT for Compton scattering
on
   LOSS  2                         !  GEANT for Landau fluct.  on
   DRAY  0                         !  GEANT for Delta no ray
   HADR  4                         !  GEANT for hadrons using FLUKA
   MULS  1                         !  GEANT for mult.  scattering
on
   PAIR  1                         !  GEANT for pair production on
   PHOT  1                         !  GEANT for photoel.  effect
on
   ************************************************************************
   *
   *       To install a detector turn the switch 'ON'
   *
   ************************************************************************
   VER 'ON' 'FULL' 'P-ID' 'FULL' 'VCAL' 'STCK' ! MVD on with track
stack
   BBC 'ON' 'FULL' 'ETOT' 'FULL' 'BCAL' 'STCK' ! BBC on with track
stack
   ITR 'ON' 'IT96' 'ETOT' 'FULL' 'TRKS'        ! Latest Dch, PC1
vers.
   CRK 'ON' 'FULL' 'P-PZ' 'FULL' 'CCAL' 'CO2 ' !  RICH with CO2 gas
```

```
   PAD 'ON' 'PC98' 'P-ID' 'FULL' 'PCAL'        ! Latest version of
PC2/PC3
   TRD 'ON' 'FULL' 'P-ID' 'FULL' 'TCAL'        ! This is the TEC
   TOF 'ON' 'FULL' 'P-ID' 'FULL' 'FCAL' 0.0 0.0!  Time of Flight
   EMC 'ON' 'FULL' 'FULL' 'FULL' 'ECAL' 'AUAU' ! EMCal, H.I. with
Cerenkov
   MUM 'ON' 'FULL' 'ETOT' 'FULL' 'MCAL' 0.  0.  0.  'STCK' 'NNEU'
!
   MUI 'ON' 'FULL' 'ETOT' 'FULL' 'NCAL' 0.  0.  0.  'STCK' 'NNEU'
!
   ZDC 'ON' 'FULL' 'ETOT' 'FULL' 'ZCAL' 'FRG1' 'HBOO' 42.7 !!!
```

`event.par`

This is the standard event parameter file for PISA. ZDC has introduced line1 and 2 (`b_min, b_max`) to allow selection of impact parameter ranges (in fm's). Set parameter `north_south` to 0 or 1, according to only north or both directions are considered in the analysis. Rapidity, momentum, azimuthal and tilte angles below are set to usual values. This is a typical set of parameters that allow for almost the whole momentum domain of the produced or (event) generated particles.

```
   $epar
   b_min =  0.0,
   b_max = 15.0,
   y_min = -1.e+20,
   y_max = +1.e+20,
   p_min =  0.03,
   p_max = +1.e+20,
   pt_min = 0.00,
   pt_max = +1.e+20,
   the_min =0.00,
   the_max =+180.00,
   phi_min =-180.00,
```

```
phi_max =+180.00,
xyz0_input = 0.0, 0.0, 0.0,
vrms = 0.025, 0.025, 0.0,
north_south = 1,
nskip_evt = 0,
t0cent = 0.0,
t0width = 0.0,
$end
*************************************************************************
*
* Lines below show how one "includes" only pions using GEANT IDs
*
* iincl = +3,   (0 means all particles to include
* include = 8, 9, 7, 17*0,
*
*************************************************************************
```

Results

Output files of ZDC

The output files that are related to the ZDC detector are the standard ROOT and HBOOK files of PISA (`PISAEvent.root` and `gintphnx.hbk`, respectively). The `.root` file contains all the hit information that belong to an event of a charged particle crossing a Cherenkov fiber, i.e., position, number of photoelectrons produced, momentum, time of flight, particle ID. The figure below has been created by PAW from the HBOOK file `gintphnx.hbk`.

To correlate ZDC results to the ones of other detectors contact the person responsible for the code of that detector.

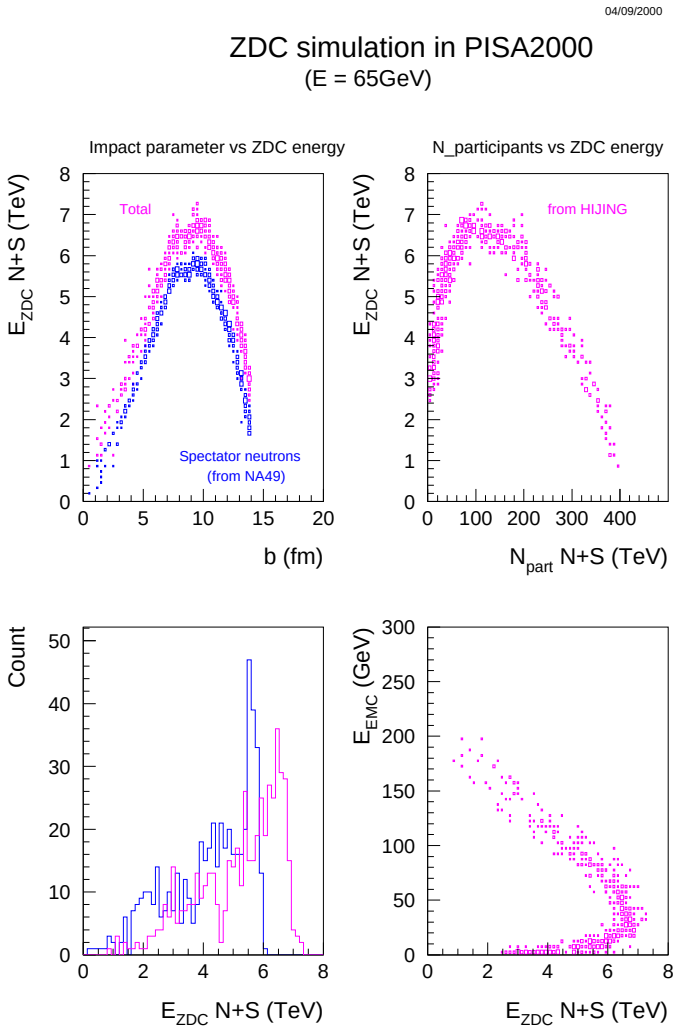

Figure 2.12: Various plots of ZDC response simulations. See labels for explonations.

Chapter 3

Hydrodynamical modelling

3.1 Non-relativistic hydrodynamics

3.1.1 Introduction

The equations of hydrodynamics reflect the local conservation of charge, momentum and energy. These equations are well suited to study problems related to flows in various fields ranging from evolution of galaxies in astrophysics to heavy-ion and elementary-particle collisions in high-energy physics. The finding of exact self-similar hydro solutions sometimes represents essential progress in physics, as the discovery of the Hubble flow of our Universe or the Bjorken flow of ultrarelativistic heavy-ion collisions.

In this section we consider the case of a non-relativistic hydrodynamical problem with ellipsoidal symmetry. Our goal is to demonstrate the influence of initial conditions on the final state observables, utilizing an explicit, exact and simple analytic solution of fireball hydrodynamics. In particular, we attempt to understand the relationship between the initial conditions (the ellipsoidal asymmetry and the tilt of the major axis) and the final observables. This section is based on ref. [Csö01]

A self-similar solution of non-relativistic hydrodynamics with ideal gas equation of state and a generalized (direction-dependent) Hubble flow, a three-dimensional ellipsoidal Gaussian density profile and a homogeneous, space-indepenent temperature profile has been found in ref. [Akk01]. This

solution has many interesting properties, e.g. the partial differential equations of hydrodynamics are reduced to ordinary differential equations corresponding to a Hamiltonian motion of a massive particle in a non-central repulsive potential. These results correspond to the generalization of earlier, data motivated hydrodynamical parameterizations and/or solutions of refs. [Bon78, Csö94b, Csi98, Csö98, Hel97, Csö95b, Csö95a, Jde78] to ellipsoidal symmetry and non-central heavy-ion collisions with homogeneous temperature profile.

Below let us summarize the hydrodynamic solution of ref. [Akk01] for some fairly wide family of thermodynamically consistent equations of state, and calculate analytically all the observables of non-central collisions. It allows, in principle, to solve an inverse problem, namely, given an (in general non-ideal) equation of state, to restore the initial conditions from the observables. However, we do not aim here to apply directly the new hydro solution to data fitting in high-energy heavy-ion physics. In order to reach the level of data fitting, generalizations to relativistic flow patterns, more realistic equations of state and temperature profiles are needed. Some of these generalizations seem to be straightforward and are in progress [Csö01b, Csö02], and will be discussed in Section 3.2.

3.1.2 The equations of non-relativistic hydrodynamics

Consider the non-relativistic hydrodynamical problem, as given by the continuity, Euler and energy equations:

$$\partial_t\, n + \nabla \cdot (n\mathbf{v}) = 0\,, \tag{3.1}$$

$$\partial_t\, \mathbf{v} + (\mathbf{v}\cdot\nabla)\mathbf{v} = -(\nabla p)/(mn)\,, \tag{3.2}$$

$$\partial_t\, \epsilon + \nabla \cdot (\epsilon\mathbf{v}) = -p\nabla\cdot\mathbf{v}\,, \tag{3.3}$$

where n denotes the particle number density, $\mathbf{v}$ stands for the non-relativistic (NR) flow velocity field, ϵ for the NR energy density, p for the pressure and in the following the temperature field is denoted by T. This set of equations are closed by some equation of state (EoS). We have chosen analytically solvable

generalization of NR ideal gas equations of state:

$$p = nT\,, \qquad \epsilon = \kappa(T)nT, \tag{3.4}$$

which allow to study the solutions of NR hydro equations for any temperature dependent ratio of pressure to energy density, $p/\epsilon = 1/\kappa(T)$. The EoS (3.4) are thermodynamically consistent for any function $\kappa(T)$, as can be checked by using the free energy density $f(T,n)$ and the relations

$$p = n\frac{\partial f}{\partial n} - f\,, \qquad \epsilon = f - T\frac{\partial f}{\partial T}\,. \tag{3.5}$$

The function $\kappa(T)$ characterizes the p/ϵ ratio for a broad variety of materials: e.g. a non-relativistic ideal gas yields $\kappa(T) = 3/2$. Note, that for finite-size systems phase transition can occupy certain temperature interval similar to a crossover. Then one can model such a change of the pressure to energy density ratio at phase transition from deconfined quark matter to hadronic one by means of smooth variations of the values of $\kappa(T)$ in certain temperature domain. Note also that it is usual to introduce the speed of sound as $c_s^2 = dp/d\epsilon = 1/\kappa(T)$, so we model the change in the equation of state essentially with the help of a temperature dependent speed of sound. Such a structure, a temperature dependent, but nearly chemical potential independent $\kappa(T)$ is consistent with lattice QCD equation of state calculations [Aok06].

3.1.3 Ellipsoidal solutions

For reasons of convenience we choose n, $\mathbf{v}$ and T as the independent hydrodynamic variables. The NR hydro equations are solved refCso01, similarly as it was done for the case of NR ideal gas EoS in ref. [Akk01], by the following self-similar, ellipsoidally symmetric density and flow profiles:

$$n(t,\mathbf{r}') = n_0\frac{V_0}{V}\exp\left(-\frac{r_x'^2}{2X^2} - \frac{r_y'^2}{2Y^2} - \frac{r_z'^2}{2Z^2}\right), \tag{3.6}$$

$$\mathbf{v}'(t,\mathbf{r}') = \left(\frac{\dot{X}}{X}\,r_x', \frac{\dot{Y}}{Y}\,r_y', \frac{\dot{Z}}{Z}\,r_z'\right), \tag{3.7}$$

where the variables are defined in a center of mass frame K', but with the axes pointing to the principal directions of the expansion. The time dependent scale parameters are denoted by $(X, Y, Z) = (X(t), Y(t), Z(t))$, the typical volume of the expanding system is $V = XYZ$, and the initial temperature and volume are $T_0 = T(t_0)$ and $V_0 = V(t_0)$, and n_0 is a constant. The time evolution of the radius parameters X, Y, Z and temperature T are governed by the ordinary differential equations

$$\ddot{X}X = \ddot{Y}Y = \ddot{Z}Z = \frac{T}{m}\,, \tag{3.8}$$

$$\dot{T}\frac{d}{dT}(\kappa T) + T\left(\frac{\dot{X}}{X} + \frac{\dot{Y}}{Y} + \frac{\dot{Z}}{Z}\right) = 0\,. \tag{3.9}$$

Note that the equation for the time dependence of the temperature can be integrated in a straigthforward manner to find

$$\frac{V_0}{V} = \exp\left[\kappa(T) - \kappa(T_0)\right] \exp\int_{T_0}^{T} \frac{dT'}{T'}\kappa(T')\,, \tag{3.10}$$

and this equation further simplified, in the case of a temperature independent κ, as

$$T = T_0\left(\frac{V_0}{V}\right)^{1/\kappa}. \tag{3.11}$$

3.1.4 Observables from the solutions

In order to evaluate the measurable quantities, any hydrodynamical solution has to be supplemented with an additional freeze-out criterion, that specifies the end of the hydrodynamical evolution. Here we assume sudden particle freeze-out at a constant temperature $T(t_f, \mathbf{r}) = T_f$ where EoS corresponds approximately to ideal gas ($\kappa(T_f) = 3/2$). This freeze-out condition is reached everywhere at the same time in the considered class of exact hydrodynamical solutions and it is motivated by the simplicity of the results. Then, the emission function is proportional to

$$S(t, \mathbf{r}', \mathbf{k}') \propto \mathrm{e}^{-\frac{(x\mathbf{k}' - m\mathbf{v}')^2}{2mT_f} - \frac{r_x'^2}{2X_f^2} - \frac{r_y'^2}{2Y_f^2} - \frac{r_z'^2}{2Z_f^2}}\,\delta(t - t_f)\,. \tag{3.12}$$

3.1.5 Single particle spectrum

The single-particle spectrum and the two-particle correlation function can be evaluated similarly to that of ref. [Csö94b, Csi98]:

$$E\frac{d^3n}{d\mathbf{k}'} \propto E\exp\left(-\frac{k_x'^2}{2mT_x'}-\frac{k_y'^2}{2mT_y'}-\frac{k_z'^2}{2mT_z'}\right), \tag{3.13}$$

$$T_x' = T_f + m\dot{X}_f^2 , \tag{3.14}$$

$$T_y' = T_f + m\dot{Y}_f^2 , \tag{3.15}$$

$$T_z' = T_f + m\dot{Z}_f^2 . \tag{3.16}$$

Here $E = m + \mathbf{k}'^2/(2m)$ in the non-relativistic limit we are considering, $\mathbf{k}' = (k_x', k_y', k_z')$ stands for the momentum vector in K', $X_f = X(t_f)$, etc. In the spherically symmetric case of $X = Y = Z = R$, we recover the earlier results [Csö94b, Csi98], with $\langle u\rangle = \dot{R}$ and $T_{\rm eff} = T_f + m\langle u\rangle^2$.

The observables are determined in the center of mass frame of the collision, K, where the r_z axis points to the direction of the beam and the r_x axis to that of the impact parameter. In this frame, the coordinates and the momenta are denoted by $\mathbf{x}$ and $\mathbf{k}$. We assume that the initial state of the hydrodynamic evolution corresponds to a rotated ellipsoid in K. The tilt angle θ represents the rotation of the major (longitudinal) direction of expansion, r_z' from the beam axis r_z. Hence the event plane is the (r_x', r_z') plane, which is the same as the (r_x, r_z) plane. The (zenithal) angle between directions r_z and r_z' is θ, while the (azimuthal) angle between the transverse momentum $\mathbf{k}_t$ and the event plane is ϕ.

The ellipsoidal spectrum of eq. (3.13) generates the following ϕ averaged single-particle spectrum in the K frame:

$$\frac{d^2n}{2\pi k_t dk_t dk_z} \propto \exp\left(-\frac{k_t^2}{2mT_{\rm eff}}-\frac{k_z^2}{2mT_z}\right) f(v,w) , \tag{3.17}$$

$$\frac{1}{T_z} = \frac{\cos^2\theta}{T_z'}+\frac{\sin^2\theta}{T_x'} , \tag{3.18}$$

$$\frac{1}{T_x} = \frac{\cos^2\theta}{T_x'}+\frac{\sin^2\theta}{T_z'} , \tag{3.19}$$

$$\frac{1}{T_{\rm eff}} = \frac{1}{2}\left(\frac{1}{T_x}+\frac{1}{T'_y}\right), \tag{3.20}$$

$$w = \frac{k_t^2}{4m}\left(\frac{1}{T'_y}-\frac{1}{T_x}\right), \tag{3.21}$$

$$v = -\frac{k_t k_z}{2m}\sin(2\theta)\left(\frac{1}{T'_x}-\frac{1}{T'_z}\right), \tag{3.22}$$

$$f(v,w) \approx I_0(w)+\frac{v^2}{4}\left[I_0(w)+I_1(w)\right] , \tag{3.23}$$

where $f(v,w)$ is calculated for $|v| \ll 1$ and $I_n(w) = \frac{1}{\pi}\int_0^\pi dz\cos(nz)\exp[w\cos(z)]$ is the modified Bessel function of order n ($n = 0, 1, ...$). For small ellipsoidal asymmetries, $w \ll 1$, $I_0(w) \simeq 1$ and the effective temperature parameter in the transverse direction is the harmonic mean of the temperature parameters of the principal directions of expansion (projected to the transverse plane). As $T'_z \geq T'_x \geq T'_y$ is expected from the initial conditions, we obtain $T_x \geq T'_x$ and $T_z \leq T'_z$.

The flow coefficients v_n are defined as

$$\frac{d^3n}{dk_z k_t dk_t d\phi} = \frac{d^2n}{2\pi dk_z k_t dk_t}\left[1+2\sum_{n=1}^{\infty} v_n\cos(n\phi)\right]. \tag{3.24}$$

Here v_1 is called the directed flow, v_2 the elliptic flow and v_3 the third flow. The transverse- and longitudinal- momentum dependence of the v_n flow components can be written in terms of v and w. Assuming that the tilt angle θ or the anisotropy is small, $|v| \ll 1$, the directed, elliptic and third flow components are evaluated as

$$v_1 = \frac{v}{2}\left[1+\frac{I_1(w)}{I_0(w)}\right], \tag{3.25}$$

$$v_2 = \frac{I_1(w)}{I_0(w)}+\frac{v^2}{8}\left[1+\frac{I_2(w)}{I_0(w)}-2\left(\frac{I_1(w)}{I_0(w)}\right)^2\right], \tag{3.26}$$

$$v_3 = \frac{v}{2}\frac{I_2(w)+I_1(w)}{I_0(w)} . \tag{3.27}$$

An angular tilt $\theta \neq 0$ is evidenced by the rise of the directed and third flows as a function of rapidity $y = 0.5\ln[(E+k_z)/(E-k_z)]$ and by a minimum of the elliptic flow at mid-rapidity, see Fig. 3.1.7. This and other features are

in qualitative agreement with most of the data on intermediate- and high-energy heavy-ion collisions [Dan01, Bäc99, Ack01, Cse99], suggesting that in non-central collisions the dominant longitudinal direction of expansion is perheps slightly deviating from the beam direction. A more straightforward proof of the ellipsoidal nature of the flow can be obtained by determining the mass dependence of the parameters T'_x, T'_y and T'_z, cf. eqs. (3.14-3.16) and Fig. 3.1.7. Note, that in the recent PHOBOS $v_2(\eta)$ measurements a maximum is seen at midrapidity, which indicates the tilt angle (θ) is small, nearly 0, and $v_2 = I_1(w)/I_0(w)$

3.1.6 Two-particle correlations

The two-particle Bose-Einstein correlation function (BECF) is related to a Fourier-transform of the emission (or source) function $S(t, \mathbf{r}', \mathbf{k}')$ of eq. (3.12), see e.g. refs. [Csö94b, Csi98, Hel97]. If the core-halo picture [Csö94a] is valid, an effective intercept parameter $\lambda \equiv \lambda(\mathbf{k}) = [N_c(\mathbf{k})/N(\mathbf{k})]^2$ appears, that measures the fraction of particles emitted directly from the core. The two-particle BECF is diagonal in K', as

$$
\begin{aligned}
C(\mathbf{K}', \mathbf{q}') &= 1 + \lambda \exp\left(-q_x'^2 R_x'^2 - q_y'^2 R_y'^2 - q_z'^2 R_z'^2\right), && (3.28)\\
\mathbf{K}' &= \mathbf{K}'_{12} = 0.5(\mathbf{k}'_1 + \mathbf{k}'_2), && (3.29)\\
\mathbf{q}' &= \mathbf{q}'_{12} = \mathbf{k}'_1 - \mathbf{k}'_2 = (q'_x, q'_y, q'_z), && (3.30)\\
R_x'^{-2} &= X_f^{-2}\left(1 + \frac{m}{T_f}\dot{X}_f^2\right), && (3.31)\\
R_y'^{-2} &= Y_f^{-2}\left(1 + \frac{m}{T_f}\dot{Y}_f^2\right), && (3.32)\\
R_z'^{-2} &= Z_f^{-2}\left(1 + \frac{m}{T_f}\dot{Z}_f^2\right). && (3.33)
\end{aligned}
$$

These radius parameters measure the lengths of homogeneity [Sin94]. They are dominated by the shortest of the geometrical scales (X_f, Y_f, Z_f) and the corresponding thermal scales defined by $(X_T, Y_T, Z_T) = \sqrt{\frac{T_f}{m}}(\frac{X_f}{\dot{X}_f}, \frac{Z_f}{\dot{Z}_f}, \frac{Z_f}{\dot{Z}_f})$, generalizing the results of refs. [Csö94b, Hel97, Csö95b, Csö95a] to ellipsoidal flows. The geometrical scales characterize the spatial variation of the fugac-

ity term $\mu(t,\mathbf{r}')/T(t,\mathbf{r}')$, while the thermal scales characterize the spatial variations of the Boltzmann term $E'_{\rm loc}(t,\mathbf{r}')/T(t,\mathbf{r}')$, both of them evaluated at the point of maximal emittivity. In the K' frame, cross-terms [Cha95] vanish, $R^2_{i\neq j}=0$, if the emission is sudden.

If the particle emission is gradual, but it happens in a narrow interval Δt centered at t_f, then the BECF can be evaluated using the replacement $\delta(t-t_f)\ \to\ (2\pi\Delta t^2)^{-1/2}\exp[-(t-t_f)^2/2\Delta t^2]$ in eq. (3.12), if $\Delta t\dot{X}_f << X_f$, etc. Hence all the previous radius components, including the cross-terms, are extended with an additional term $\delta R'^2_{ij}=\beta'_i\beta'_j\Delta t^2$, where $\boldsymbol{\beta}'=(\mathbf{k}'_1+\mathbf{k}'_2)/(E'_1+E'_2)$ is the velocity of the pair in K'.

The BECF's are usually given in the side-out-longitudinal or Bertsch-Pratt (BP) parameterization. The longitudinal direction, $r_{\rm long}\equiv r_{\rm l}$ in BP coincides with the beam direction. The plane orthogonal to the beam is decomposed to a direction parallel to the mean transverse momentum of the pair, $r_{\rm out}\equiv r_{\rm o}$, and the one perpendicular both to this and the beam direction, $r_{\rm side}=r_{\rm s}$. The mean velocity of the particle pair can be written in BP as $\boldsymbol{\beta}=(\beta_{\rm o},0,\beta_{\rm l})$, where $\beta_{\rm o}=\beta_t$. Let ϕ denote the angle of the event plane and the mean transverse momentum of the measured pair. The result is

$$
\begin{aligned}
C_2(\mathbf{K},\mathbf{q}) &= 1+\lambda\exp\left(-\sum_{i,j={\rm s,o,l}} q_iq_jR^2_{ij}\right), && (3.34)\\
R^2_{\rm s} &= R'^2_y\cos^2\phi+R^2_x\sin^2\phi\,, && (3.35)\\
R^2_{\rm o} &= R^2_x\cos^2\phi+R'^2_y\sin^2\phi+\beta_t^2\Delta t^2, && (3.36)\\
R^2_{\rm l} &= R'^2_z\cos^2\theta+R'^2_x\sin^2\theta+\beta_{\rm l}^2\Delta t^2, && (3.37)\\
R^2_{\rm ol} &= (R'^2_x-R'^2_z)\cos\theta\sin\theta\cos\phi+\beta_t\beta_{\rm l}\Delta t^2, && (3.38)\\
R^2_{\rm os} &= (R^2_x-R'^2_y)\cos\phi\sin\phi\,, && (3.39)\\
R^2_{\rm sl} &= (R'^2_x-R'^2_z)\cos\theta\sin\theta\sin\phi\,, && (3.40)
\end{aligned}
$$

where an auxiliary quantity is introduced as

$$
R^2_x=R'^2_x\cos^2\theta+R'^2_z\sin^2\theta\ . \qquad (3.41)
$$

These results imply that all the radius parameters oscillate in the K frame. In particular, a ϕ dependent oscillation appears in the radius parameters indexed either by the *side* or the *out* direction, as illustrated in Fig. 3.1.7. These oscillations are similar to those obtained in ref. [Wie98], corresponding to $\theta = 0$. We find that the radius parameters indexed by the *longitudinal* direction depend also on the zenithal angle θ. A toy model for tilted ($\theta \neq 0$) ellipsoidal static pion sources was introduced in refs. [Lis00], to understand the ϕ dependent oscillations of measured HBT radii at AGS energies. In our case, the amplitude of the oscillations is reduced for heavier particles due to the hydrodynamic expansion, which results in a decrease of the lengths of homogeneity with increasing mass. The oscillations of the radius parameters were not related before either to hydrodynamic flow with ellipsoidal symmetry and tilt of the major axis or connected to the initial conditions of a hydrodynamic expansion.

A check of the applicability of our hydrodynamic solution is that the BECF and the single particle spectrum become diagonal (after removing a term of $\beta_i\beta_j\Delta t^2$ from all the HBT radius parameters) in the *same* frame, see eqs. (3.13,3.14-3.16) and eqs. (3.28,3.31-3.33). This frame is K', the natural System of Ellipsoidal Expansion or SEE.

3.1.7 Connections of initial freez-out conditions in non-relativistic hydrodynamics

Single-particle spectrum and the two-particle Bose-Einstein correlation function have analytically been evaluated for a self-similarly expanding, exact, ellipsoidal solution of the non-relativistic hydrodynamical equations, assuming a constant freeze-out temperature.

The parameters of the hydro solution at freeze-out time T_f, (X_f, Y_f, Z_f) and $(\dot{X}_f, \dot{Y}_f, \dot{Z}_f)$, can be reconstructed from the measurement of the single particle spectrum and the two-particle correlation functions. The direction of the major axis of expansion in the center of mass frame of the collision is characterized by the polar angles $(\theta, 0)$. With the exception of R_l, all the

radius parameters oscillate as function of ϕ, while the radius parameters $R_{\rm l}^2$, $R_{\rm ol}^2$, $R_{\rm sl}^2$ depend also on θ. All the radius parameters decrease with increasing mass, including all the cross terms. If $\theta \neq 0$, the effective temperature in the transverse direction is increased by a contribution from the longitudinal expansion.

The initially more compressed longitudinal and impact parameter directions (the r_z and r_x directions) expand more dynamically [Akk01, Csö01b], that implies $T'_z \geq T'_x \geq T'_y$. The initial time t_0 can be identified from the requirement that $\dot{Y}(t_0) = 0$. *The initial conditions for this hydrodynamical system can be uniquely reconstructed from final state measurements, for a given EoS.* The function $\kappa(T)$ in the EoS influences only the time evolution of the scales (X, Y, Z) and temperature T. So, for a given EoS, one can uniquely reconstruct the initial conditions of hydrodynamic evolution from final ones. However, it is also clear that the same FO conditions can be reached froma large class of initial conditions, i.e. $(T_f, X_f, Y_f, Z_f, \dot{X}_f, \dot{Y}_f, \dot{Z}_f)$ is a functional of the EoS, $\kappa(T)$ and the freez-out conditions $(T_0, X_0, Y_0, Z_0, \dot{X}_0, \dot{Y}_0, \dot{Z}_0)$. Hence, EoS and IC can be co-varied to yield exactly the same FO, hence, exactly the same hadron observables. Therefore, it is not necessary to know the initial conditions if we want to reconstruct the final state of high energy heavy ion collisions. But, once we know the EoS from independent calculations the question can be answered.

We have deliberately chosen the presentation as simple as possible, which limits the direct applicability of our results in high-energy heavy-ion collisions only to sufficiently small transverse momentum, $p_t \ll m$, at midrapidity. But the scheme permits generalization in many points and still the qualitative features of our results may survive even in the relativistic regime. Generalizations to some relativistic flows have been described in ref. [Csö02]. Ref. [Csö01b] includes another extension to an arbitrary, inhomogeneous, ellipsoidally symmetric initial temperature profile, which does not change the time evolution of the scale parameters. It turns out that each of these generalizations is essentially straightforward.

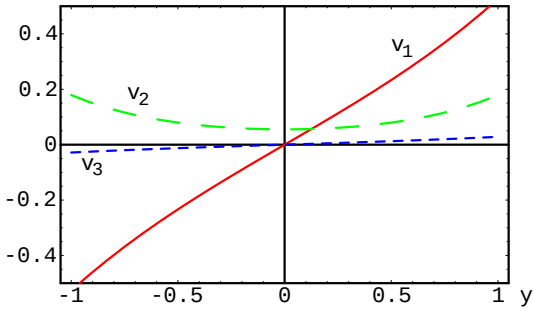

Figure 3.1: The directed, elliptic and third flows v_1, v_2, v_3 are illustrated, respectively with solid, long-dashed and short-dashed lines, as a function of rapidity, for $m = 940$ MeV, $T'_x = 200$ MeV, $T'_y = 150$ MeV, $T'_z = 700$ MeV, at a fixed $k_t = 500$ MeV and $\theta = \pi/5$, see eqs. (3.25-3.27).

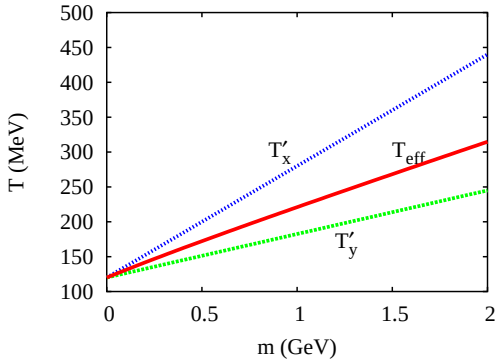

Figure 3.2: The linear mass dependence of the effective temperatures in the transverse directions, T'_x, T'_y and their (harmonic) average $T_{\rm eff}$ for non-central heavy-ion collisions, if $T_f = 120$ MeV, $\dot{X} = 0.4$, and $\dot{Y} = 0.25$ and $\theta = 0$.

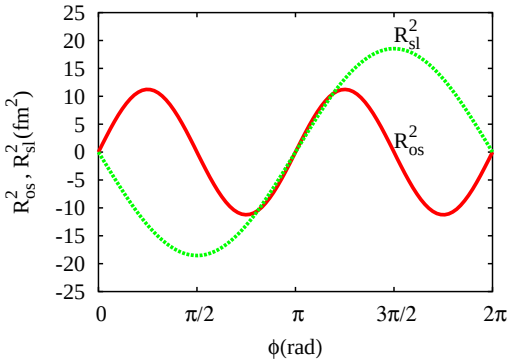

Figure 3.3: The out-side and the side-long cross terms are plotted as a function of the polar angle ϕ, for $R'_x = 5$ fm, $R'_y = 4$ fm, $R'_z = 8$ fm and $\theta = \pi/5$. Note that $R^2_{\rm sl} \propto \sin(\phi)$ while $R^2_{\rm os} \propto \sin(2\phi)$. See eqs. (39) and (40).

3.2 Relativistic hydrodynamics

3.2.1 Introduction

Recently, new families of exact analytic solutions of relativistic hydrodynamics have been found in a Hungarian-Brazilian collaboration. The simplest case corresponds to the (1+1)-dimensional expansions [Csö02d]: it consists of a class of 1-dimensional scaling flows with a proper-time dependent pressure, but characterized with an arbitrary rapidity distribution and a temperature field that is coupled to the rapidity distribution, thus overcoming one of the shortcomings of the well-known Hwa-Bjorken solution [Bjo83], which has a flat rapidity distribution. Physically, the situation described in [Csö02d] may characterize e.g. soft collisions of hadrons at high bombarding energies. These solutions are obtained for a broad class of equations of state that may include massive particles and an arbitrary constant of proportionality between the kinetic energy density and the pressure. The (1+1)-dimensional solutions have been generalized to the case of cylindrical symmetry in ref. [Csö02d], describing a physical situation that may correspond to central collisions of heavy ions at ultra-relativistic colliding energies, thus, overcoming another shortcoming of Hwa-Bjorken solution, which contains no transverse flow. These exact analytic solutions, reported in refs. [Csö02d], are associated to each non-negative scaling function $\mathcal{V}(s)$ that satisfies the normalization condition $\mathcal{V}(0) = 1$, where the argument s is a scaling variable that guarantees the self-similarity of the solutions. Here we present a broader class of solutions belonging to this new family of exact solutions. In particular, we shall describe two classes of ellipsoidally symmetric solutions of relativistic hydrodynamics, that may be relevant for the study of non-central collisions of heavy ions at relativistic bombarding energies.

Recently, new exact solutions were obtained with relativistic acceleration, but their detailed discussion go beyond the scope of this PhD thesis. Let us note, that acceleration implies work, and work leads to a factor of 2 correction in the estimate of the initial energy density: the accelerationless Bjorken

estimate yield $\epsilon_0 = 5GeV/fm^3$, while the accelerating solutions fitted to BRAHMS dn/dy data provide $\epsilon_0 = 10GeV/fm^3$ in Au+Au collisions at RHIC at $\tau_0 \approx 1fm/c$

In general, exact analytic resolution of 3 dimensional relativistic hydrodynamics is a difficult task due to the highly non-linear nature of these equations. The complications are sometimes simplified by assuming idealized boundary conditions and simplified equations of state (e.g. infinite bombarding energy and a massless relativistic gas in the case of Hwa-Bjorken's solution [Cse94]). A more realistic but analytically more complicated solution had been found by Khalatnikov [Kha54], following Landau's basic ideas [Lan53], that gave rise to the hydrodynamical approach in high-energy physics. Both of these solutions are frequently utilized as the basis for estimations of various observables in ultra-relativistic nucleus-nucleus collisions [Cse94].

Analytic solutions of relativistic hydrodynamics were also reported recently in refs. [Bir00a, Bir00b]. However, these solutions are valid only at the softest point of the equation of state. For more realistic situations, the (1+3)-dimensional relativistic hydrodynamical equations are frequently solved using various numerical methods, for example, recent solutions were obtained with the help of smoothed-particle hydrodynamics in refs. [Agu01, Agu02].

The exact analytic solutions, reported here, are generalizations of the results of refs. [Csö02d] to the case of 3-dimensional relativistic expansions with less and less symmetry. However, we emphasize that these results also correspond to generalizations of earlier analytic solutions of non-relativistic hydrodynamics. The first solutions of this kind have been found by Zimányi, Bondorf and Garpman (ZBG) in 1978 [Bon78]. The key aspect of the ZBG solution is its self-similarity, this property is kept in all the subsequent generalizations including cylindrical or ellipsoidal symmetries and relativistic flows. The ZBG solution has been generalized to the case of spheroidally symmetric expansions in ref. [Jde78], to spherically symmetric Gaussian expansions in ref. [Csi98]. From the point of view of the relativistic generalizations, an im-

portant stepping stone was made in ref. [Csö98] when a scaling function has been introduced for the spherically symmetric non-relativistic solutions of hydrodynamics. This was the first case when a whole new family of solutions has been found, that assigned an independent solution for every (differentiable and integrable) scaling function that satisfied the requirement of positivity $\mathcal{T}(s) > 0$ and normalized as $\mathcal{T}(0) = 1$. The ZBG and the spherical Gaussian solutions appeared as special choices for the functional form of the scaling function $\mathcal{T}(s)$. The Gaussian family of *spherical* solutions has been generalized to Gaussian *ellipsoidal* expansions in refs. [Akk01, Csö01c]. Recently, the whole family of self-similar ellipsoidally symmetric non-relativisitic solutions of hydrodynamics has been found in ref. [Csö01b]. In the present paper, we report on the generalization of this family of solutions to the case of relativistic expansions with ellipsoidal symmetry and introduce new families of relativistic solutions with even less than ellipsoidal symmetry. All the solutions reported here have non-trivial non-relativistic limiting behaviour.

3.2.2 The equations of relativistic hydrodynamics

Let us adopt the following notational conventions: the coordinates are $x^\mu = (t, \mathbf{r}) = (t, r_x, r_y, r_z)$, $x_\mu = (t, -r_x, -r_y, -r_z)$ and the metric tensor is $g^{\mu\nu} = g_{\mu\nu} = \mathrm{diag}(1, -1, -1, -1)$. The relativistic continuity and energy-momentum-conservation equations are

$$\partial_\mu (n u^\mu) = 0\,, \tag{3.42}$$

$$\partial_\nu T^{\mu\nu} = 0\,, \tag{3.43}$$

where $n \equiv n(x)$ is the conserved number density, $u^\mu \equiv u^\mu(x) = \gamma(1, \mathbf{v})$ is the four-velocity, with $u^\mu u_\mu = 1$, and $T^{\mu\nu}$ is the energy-momentum tensor. We assume perfect fluid,

$$T^{\mu\nu} = (\epsilon + p) u^\mu u^\nu - p g^{\mu\nu}, \tag{3.44}$$

where ϵ stands for the relativistic energy density and p is the pressure.

From general thermodynamical considerations and the perfectness of the fluid one can show that the expansion is adiabatic,

$$\partial_\mu(\sigma u^\mu) = 0\,, \tag{3.45}$$

where σ stands for the entrophy density.

For the equations of state, we assume a gas that may contain massive conserved quanta,

$$\epsilon = mn + \kappa p\,, \tag{3.46}$$

$$p = nT. \tag{3.47}$$

These equations have two free parameters, m and κ. Non-relativistic hydrodynamics of ideal gases corresponds to the limiting case of $\mathbf{v}^2 \ll 1$ and $\kappa = \frac{3}{2}$. Our solutions, presented below, exist for all values of $m \geq 0$ and $\kappa > 0$.

Using the continuity equation (3.42) and the equations of state (3.46,3.47), the energy-momentum-conservation equations, (3.43) can be transformed to the Euler and temperature equations,

$$u_\nu u^\mu \partial_\mu p + (\epsilon + p) u^\mu \partial_\mu u_\nu - \partial_\nu p = 0\,, \tag{3.48}$$

$$u^\mu \partial_\mu T + \frac{1}{\kappa} T \partial_\mu u^\mu = 0\,. \tag{3.49}$$

Expressing the energy density and the pressure in the 3 independent components of the relativistic Euler equation in terms of n and T with the help of the equations of state, (3.46,3.47), one obtains a closed system of 5 equations (the continuity, the Euler and the temperature equations) in terms of 5 variables, n, T and $\mathbf{v} = (v_x, v_y, v_z)$.

3.2.3 Ellipsoidally symmetric solutions

We discuss self-similar solutions in which the isotherms at each instant are ellipsoidal surfaces, where the number density is also constant. We do not discuss here how the major axes of these ellipsoids may be rotated in the

frame of observation. We describe the solution in the natural System of Ellipsoidal Expansion (SEE) [Akk01, Csö01c], where the coordinate axes point to the pricipal directions of the expansion, similarly to the previous section on non-relativistic hydrodynamics. Let us now define the following scaling variable

$$s = \frac{r_x^2}{X^2} + \frac{r_y^2}{Y^2} + \frac{r_z^2}{Z^2}\,, \tag{3.50}$$

where the scale parameters $X = X(t)$, $Y = Y(t)$ and $Z = Z(t)$ are assumed to depend only on the time variable t. The condition $s = const.$, at each instant t, defines the isotherms mentioned above. As these surfaces are ellipsoids, the solutions belonging to this class will be characterized by ellipsoidal symmetry. We assume a self-similar expansion of Hubble type, with possibly different Hubble constants in all the pricipal directions of the expansion:

$$v_x(t,\mathbf{r}) = \frac{\dot{X}}{X} r_x, \tag{3.51}$$

$$v_y(t,\mathbf{r}) = \frac{\dot{Y}}{Y} r_y, \tag{3.52}$$

$$v_z(t,\mathbf{r}) = \frac{\dot{Z}}{Z} r_z. \tag{3.53}$$

where $\dot{A} = dA(t)/dt$ stands for the derivative of the scale parameter $A = \{X, Y, Z\}$ with respect to time t.

As a straightforward generalization of the results derived in refs [Csö02d], we find the following new family of ellipsoidally symmetric, exact analytic solutions of relativistic hydrodynamics:

$$s = \frac{r_x^2}{\dot{X}_0^2 t^2} + \frac{r_y^2}{\dot{Y}_0^2 t^2} + \frac{r_z^2}{\dot{Z}_0^2 t^2}\,, \tag{3.54}$$

$$\mathbf{v} = \frac{\mathbf{r}}{t} \qquad \text{or} \qquad u^\mu = \frac{x^\mu}{\tau}\,, \tag{3.55}$$

$$n(t,\mathbf{r}) = n_0 \left(\frac{\tau_0}{\tau}\right)^3 \mathcal{V}(s), \tag{3.56}$$

$$p(t,\mathbf{r}) = p_0 \left(\frac{\tau_0}{\tau}\right)^{3+3/\kappa}, \tag{3.57}$$

$$T(t,\mathbf{r}) = T_0 \left(\frac{\tau_0}{\tau}\right)^{3/\kappa} \frac{1}{\mathcal{V}(s)}, \tag{3.58}$$

where $\tau = \sqrt{t^2 - \mathbf{r}^2}$, $p_0 = n_0 T_0$, $\dot{X}_0$, $\dot{Y}_0$, $\dot{Z}_0$ are constants and $\mathcal{V}(s)$ is an arbitrary positive, differentiable function of the scaling variable s normalized such that $\mathcal{V}(0) = 1$. The temperature distribution also depends on the scaling variable s through a scaling function $\mathcal{T}(s)$, which happens to be $\mathcal{T}(s) = 1/\mathcal{V}(s)$. Note that the pressure p depends only on τ.

An interesting property of this solution is that the flow and the pressure fields are spherically symmetric, however, the other thermodynamical quantities such as the temperature or density distributions are characterized by ellipsoidal symmetry.

The lack of acceleration is reflected by the equations

$$X = \dot{X}_0 t\,, \tag{3.59}$$

$$Y = \dot{Y}_0 t\,, \tag{3.60}$$

$$Z = \dot{Z}_0 t\,. \tag{3.61}$$

In this family of new solutions, the flow is three-dimensional, accelerationless Hubble-type, $u^\mu = x^\mu/\tau$, which gives

$$u^\mu \partial_\mu u_\nu = 0. \tag{3.62}$$

This property, together with the s-independence of pressure fields, guarantees that the Euler equation be satisfied regardless of the mass m and the value of κ. We have found new, self-similar, scaling solutions to the continuity and the temperature equations with ellipsoidal symmetry. Thus a new hydrodynamical solution is assigned to each scaling function $\mathcal{V}(s) = 1/\mathcal{T}(s)$, similarly to the cases of the ellipsoidally symmetric, non-relativistic solutions of ref. [Csö01b].

3.2.4 Phase transitions and freeze-out

The simplest case of the previously discussed new family of exact solutions of relativistic hydrodynamics is given by the choice of $\mathcal{V}(s) = 1$. In this case, the temperature is constant on a hypersurface characterized by a constant proper-time, and all the other thermodynamical parameters are constants on

these surfaces as well. Thus these parameters depend on τ only, similarly to the Hwa-Bjorken solution [Bjo83].

It is possible to generalize the equations of state, (3.46,3.47)to characterize a new phase of matter and then describe the rehadronization of a "Quark Matter" (QM) state to a Hadron gas (H) in a model similar to that of Gyulassy and Matsui [Gyu84]. For simplicity, from now on we refer to the the equations of state (3.46,3.47), describing massive, conserved quanta, as that of a hadron gas and index the variables with subscript $_H$. To phenomenologically describe a new phase, which includes constituent quarks and anti-quarks (Q), characterized by their mass and by a vacuum pressure, we generalize the equations of state to

$$\varepsilon_Q = m_Q n_Q + \lambda_\varepsilon n_Q T + B, \tag{3.63}$$

$$p_Q = \lambda_p n_Q T - B, \tag{3.64}$$

where λ_ε and λ_p are constants. Let us introduce the notation $\kappa_Q = \lambda_\varepsilon/\lambda_p$. With this simple ansatz, the form of the relativistic Euler and temperature equations does not change and we obtain the same form of the solutions for n, T and $\mathbf{v}$ as before, however, with modified boundary conditions corresponding to modified constants of integration. We may refer to this new phase as a kind of quark matter, providing simple model equations of state for massive quarks, and a bag constant corresponding to color deconfinement. The gluons are assumed to be integrated out, providing mass for the quarks. Such a picture is qualitatively supported by phenomenological fits to the lattice QCD equation of state with quarks that pick up the constitutent mass around T_c and gluons that carry big effective mass in the same temperature domain [1].

Using the above ansatz for the equations of state, we obtain the following solution for the pressure:

$$p_Q = (p_{0,Q} + B)\left(\frac{\tau_0}{\tau}\right)^{3+3/\kappa_Q} - B. \tag{3.65}$$

If we chose $B > 0$ and $\lambda_p > 1$, then at low temperatures the state consisting of non-relativistic massive ideal gas will be stable, and at some critical

temperature T_c the pressure of the two phases is balanced. However, at high temperatures, the pressure of the new phase will be larger than that of the hadronic matter, as $\lambda_p > 1$, hence at high temperatures this phase will be the stable one.

The critical temperature, T_c is defined by

$$n_H T_c = \lambda_p n_Q T_c - B. \tag{3.66}$$

For the hydrodynamical description, the specification of n_H and n_Q as a function of e.g. a temperature and chemical potential is not necessary, any thermodinamically consistent form can be included into the hydro solutions that we focus on. Hence the above equation may indicate, if n_H and n_Q are expressed as a function of the temperature and the (baryo)chemical potential, that the critical temperature may become density dependent.

One can show that the expansion is adiabatic if the matter consists of only one of the phases. We may assume, that the expansion is adiabatic also during the period of phase coexistence, and describe the phase transition with the help of a Maxwell construction. This case is similar to the construction discussed by Gyulassy and Matsui in case of a massless ideal gas [Gyu84]. Let us denote the entrophy density of the two phases by s_Q and s_H, and the volume fraction of the two phases by f_Q and $f_H = 1 - f_Q$, respectively. The proper-time dependence of the entrophy density is then given by

$$s(\tau) = f_Q(\tau) s_{Q,c} + (1 - f_Q(\tau)) s_{H,c}. \tag{3.67}$$

At the beginning of the phase transition, at $\tau = \tau_{Q,c}$ the whole system consists of "Quark Matter", that is $f_Q(\tau_{Q,c}) = 1$. By the time the phase transition ends, one obtains $f_Q(\tau_{H,c}) = 0$. As the well known steps of the Maxwell construction can be copied from the case without conserved charges, for further details we simply refer to section 6.2.3 of ref. [Cse94].

Starting the hydrodynamical expansion from a quark matter initial state, the form of our hydrodynamical solution becomes unmodified even during the phase transition, and the coasting type of hydrodynamical evolution can

be continued at a fixed T_c, from $\tau_{Q,c}$ to $\tau_{H,c}$ untill all matter is transformed to hadronic matter. Then one can continue the same kind of coasting solution untill the hadronic matter freezes out.

This expansion takes usually a long time, which is difficult to justify by experimental evidences. However, the same kind of hydrodynamical solution can be matched with a non-equilibrium type of phase transition, the sudden rehadronization and a simultaneous freeze-out of hadrons from a supercooled Quark Matter, as described in greater details in refs. [Csö94c, Cse95]. Then in the same model one may reach a deeply supercooled Quark Matter state, and the transition to the hadron gas may proceed via a mechanical instability, associated with a negative pressure state, governed by the conservation of matter, energy and momentum and the impossibility of an entrophy decrease in a deflagration through a hypersurface with a time-like normal vector at $\tau = \tau_{TD}$,

$$[T^{\mu\nu} df n_\nu] = 0, \tag{3.68}$$

$$[n u^\nu df n_\nu] = 0, \tag{3.69}$$

$$[s u^\nu df n_\nu] \geq 0, \tag{3.70}$$

where $df n_\nu \equiv d\sigma_\nu$ is the normal-vector of the $\tau = \tau_{TD}$ hypersurface. These equations and inequality can be solved very similarly to ref. [Csö94c], that discussed the case of a transition from a massless ideal quark-gluon plasma (QGP) to a massless hadron gas. The lack of acceleration, and the invariance of the equations of state for rescaling the temperature and for adding a vacuum energy term are the essential reasons why earlier considerations that discussed phase transitions for massless particles can be straigthforwardly implemented to our new family of exact hydrodynamical solutions that describe the phase transitions and expansions of massive quanta.

Recently, a new method has been proposed to evaluate particle emission from hydrodynamically evolving, locally thermalized sources, that generalizes the Cooper-Frye freeze-out conditions for systems with volume emission [Sin02, Gra95]. This method, based on the method of escaping proba-

bilities, can also be applied to evaluate the particle spectra and correlation functions from the new hydrodynamical solutions, as the non-relativistic form of the solutions corresponds to the limiting behaviour that was discussed in ref. [Sin02].

3.2.5 Factorized solutions

From the structure of the new family of solutions presented above, it is obvious how to generate further new solutions of relativistic hydrodynamics.

Observe that a modified version of the scaling variable of eq. (3.54) can be defined, and another family of the same kind of ellipsoidal solutions can be generated by introducing

$$s' = \frac{r_x^2}{\dot{X}_0^2\tau^2} + \frac{r_y^2}{\dot{Y}_0^2\tau^2} + \frac{r_z^2}{\dot{Z}_0^2\tau^2}\,, \tag{3.71}$$

$$X' = \dot{X}_0\tau, \tag{3.72}$$

$$Y' = \dot{Y}_0\tau, \tag{3.73}$$

$$Z' = \dot{Z}_0\tau, \tag{3.74}$$

where the dots should be understood as derivatives with respect to τ. Mathematically, the modified scaling variable solves the relativistic hydro equations, because it also satisfies the requirement

$$u^\mu\partial_\mu s = u^\mu\partial_\mu s' \;=\; 0\,, \tag{3.75}$$

if the flow is scaling. This condition can be considered also as the criterium of a "good" scaling variable, and satisfied by the following independent sets of variables:

$$s_x = \frac{r_x^2}{t^2}\,, \tag{3.76}$$

$$s_y = \frac{r_y^2}{t^2}\,, \tag{3.77}$$

$$s_z = \frac{r_z^2}{t^2}\,, \tag{3.78}$$

or alternatively,

$$s'_x = \frac{r_x^2}{\tau^2}\,, \tag{3.79}$$

$$s'_y = \frac{r_y^2}{\tau^2}\,, \tag{3.80}$$

$$s'_z = \frac{r_z^2}{\tau^2}\,. \tag{3.81}$$

All of the 6 scale variables defined above satisfy eq. (3.75) if the flow profile is of a 3-dimensional scaling type, $u^\mu = x^\mu/\tau$.

As the relationship $\mathcal{V}(s) = 1/\mathcal{T}(s)$ holds in the class of solutions we present here, if we assume a factorized form for the scaling function of the density, we automatically generate a factorized form for the scaling function of the temperature, hence it becomes easy to generate further new solutions. Let us define the scaling functions $\mathcal{V}_x(s_x)$, $\mathcal{V}_y(s_y)$ and $\mathcal{V}_z(s_z)$ that are positive, differentiable and satisfying $\mathcal{V}_x(0) = \mathcal{V}_y(0) = \mathcal{V}_z(0) = 1$, otherwise being abritrary and independent from each other. Then, a new type of hydro solutions reads

$$\mathbf{v} = \frac{\mathbf{r}}{t} \qquad \text{or} \qquad u^\mu = \frac{x^\mu}{\tau}\,, \tag{3.82}$$

$$n(t,\mathbf{r}) = n_0 \left(\frac{\tau_0}{\tau}\right)^3 \mathcal{V}_x(s_x)\mathcal{V}_y(s_y)\mathcal{V}_z(s_z)\,, \tag{3.83}$$

$$(t,\mathbf{r}) = p_0 \left(\frac{\tau_0}{\tau}\right)^{3+3/\kappa}\,, \tag{3.84}$$

$$T(t,\mathbf{r}) = T_0 \left(\frac{\tau_0}{\tau}\right)^{3/\kappa} \frac{1}{\mathcal{V}_x(s_x)} \frac{1}{\mathcal{V}_y(s_y)} \frac{1}{\mathcal{V}_z(s_z)}\,. \tag{3.85}$$

Note that this form of solution is invariant for a change of the scaling variables and the scales as $(s_x, s_y, s_z) \to (s'_x, s'_y, s'_z)$ and $(X, Y, Z) \to (X', Y', Z')$, with the time derivatives in the definitions of the Hubble flow field, eqs. (3.51-3.53) understood as derivations with respect to τ as in eqs. (3.71-3.74).

3.2.6 General solutions

The key point in checking that the above factorized forms indeed solve the equations of relativistic hydrodynamics is that the comoving derivatives of

the scaling functions, $u_\mu \partial^\mu \mathcal{V}_i(s_i)$, are proportional to $u^\mu \partial_\mu s_i$, hence vanish. This is, together with $u^\mu \partial_\mu u_\nu = 0$, the essential property of the scaling solutions.

We find that the most general form of the scaling variable is

$$\overline{s} = F(s_x, s_y, s_z) \equiv G(s'_x, s'_y, s'_z)\,, \tag{3.86}$$

which means that any function of scaling variables (s_x, s_y, s_z) or (s'_x, s'_y, s'_z) can be utilized as a new scaling variable. Indeed, we have

$$u_\mu \partial^\mu F(s_x, s_y, s_z) = \sum_{i=x,y,z} \frac{\partial F}{\partial s_i}\, u_\mu \partial^\mu s_i = 0\,. \tag{3.87}$$

which yields the generalized form of the new family of solutions of relativistic hydrodynamics:

$$\mathbf{v} = \frac{\mathbf{r}}{t} \qquad \text{or} \qquad u^\mu = \frac{x^\mu}{\tau}\,, \tag{3.88}$$

$$n(t,\mathbf{r}) = n_0 \left(\frac{\tau_0}{\tau}\right)^3 \mathcal{V}(\overline{s})\,, \tag{3.89}$$

$$p(t,\mathbf{r}) = p_0 \left(\frac{\tau_0}{\tau}\right)^{3+3/\kappa}, \tag{3.90}$$

$$T(t,\mathbf{r}) = T_0 \left(\frac{\tau_0}{\tau}\right)^{3/\kappa} \frac{1}{\mathcal{V}(\overline{s})}\,, \tag{3.91}$$

with the constraint that $\mathcal{V}(0) = 1$. For example, if we choose $\overline{s} = s_x + s_y + s_z$, we obtain solutions with ellipsoidal symmetry, however, one may choose $\overline{s} = s_x + s_y - s_z$ to obtain solutions where the isotherms are one-sheeted hyperboloids, or $\overline{s} = -s_x - s_y + s_z$ where the temperature and the density are constants on two-sheeted hyperboloids. In fact the possibilities are infinitely rich.

3.2.7 Non-relativistic limiting behaviour

As the considered equation of state contains mass as a free parameter, it is possible to study the non-relativistic limiting case of these new relativistic solutions. The local thermal motion is non-relativistic if $m \gg T$, the flow is non-relativistic in the region of $|\mathbf{r}| \ll t$, which implies $\tau \approx t$ and relates

the relativistic solutions with ellipsoidal symmetry to the asymptotic, large time behaviour of the ellipsoidally symmetric, non-relativistic solutions of refs. [Akk01, Csö01c, Csö01b]. Let us recapitulate here the general form of the non-relativistic solutions of fireball hydrodynamics [Csö01b].

The definition of the scaling variable s coincides with that of eq. (3.50). The solution for the flow field coincides with that of eqs. (3.51-3.53). The scaling function for the temperature, $\mathcal{T}(s)$ is utilized to express the solution for the NR density and temperature fields as

$$n = n_0 \frac{X_0 Y_0 Z_0}{XYZ} \frac{1}{\mathcal{T}(s)} \exp\left[-\frac{m(\dot{X}_{\rm as}^2 + \dot{Y}_{\rm as}^2 + \dot{Z}_{\rm as}^2)}{T_0} \int_0^s du \frac{1}{\mathcal{T}(u)} \right], \quad (3.92)$$

$$T = T_0 \left(\frac{X_0 Y_0 Z_0}{XYZ} \right)^{1/\kappa} \mathcal{T}(s)\,. \quad (3.93)$$

The large time behaviour of these non-relativistic, self-similar, ellipsoidal solutions of hydrodynamics is characterized by constant values of $(\dot{X}_{\rm as}, \dot{Y}_{\rm as}, \dot{Z}_{\rm as})$, which implies that for asymptotically long times a scaling flow field develops also in these non-relativistic solutions, $\mathbf{v} \approx \mathbf{r}/t$. In the exponential factor that appears in this non-relativisitic solution for n we may expand the inverse scaling function $1/\mathcal{T}(u)$ as a polinomial in u. Keeping the leading order terms, and performing the integration, we find that the exponential factor will be approximately a Gaussian factor. However, the widths of the Gaussians in all the directions will be proportional to the time. As we have assumed that $|\mathbf{r}| \ll t$, this exponential factor yields a factor of $1 + \mathcal{O}(\mathbf{r}^2/t^2)$, hence we find the general asymptotic behaviour of the non-relativistic solutions to be the *same form* as the general solution of the *relativistic* solution of the hydrodynamical equations:

$$n_{\rm as} \approx n_{\rm as} \frac{t_0^3}{t^3} \frac{1}{\mathcal{T}(s)}\,, \quad (3.94)$$

$$T_{\rm as} \approx T_{\rm as} \left(\frac{t_0}{t} \right)^{3/\kappa} \mathcal{T}(s)\,. \quad (3.95)$$

Due to the rescaling, the constants of normalization $n_{\rm as}$ and $T_{\rm as}$ are different from n_0 and T_0.

3.2.8 Summary on exact results in 3d relativistic hydrodynamics

Recently found family of relativistic hydrodynamics solutions have been generalized to the case of expanding fireballs with ellipsoidal symmetry. The solutions contain an arbitrary scaling function $\mathcal{V}(s)$, restricted only by non-negativity and by the requirement of $\mathcal{V}(0) = 1$, a very rich set of possible scaling variabes s, and 5 important parameters, the mass m, the parameter κ of the equation of state, the scale parameters $\dot{X}_0$, $\dot{Y}_0$ and $\dot{Z}_0$. Furthermore, we generalized the equations of state to describe a phase transition from a deconfined state consisting of massive (constituent) quarks and antiquarks to a state consisting of massive hadrons. Based on the scaling properties of the equations of state, as well as on the coasting nature of the expansion, we have shown that both the usual adiabatic Maxwell construction as well as the fast, non-equilibrium time-like deflagrations can be constructed and described within the considered class of exact, parametric, relativistic, hydrodynamical solutions.

Chapter 4

The Buda-Lund hydrodynamical model

4.1 Introduction

In this section analytic and numeric approximations are studied in detail for a hydrodynamic parameterization of single-particle spectra and two-particle correlation functions in high energy hadron-proton and heavy ion reactions. Two very different sets of model parameters are shown to result in similarly shaped correlation functions and single particle spectra in a rather large region of the momentum space. However, the *absolute normalization* of the single-particle spectra is found to be highly sensitive to the choice of the model parameters. For data fitting the analytic formulas are re-phrased in terms of parameters of direct physical meaning, like mean transverse flow. The difference between the analytic and numeric approximations are determined as an analytic function of source parameters.

In 1994-95, a series of papers were written by the Buda-Lund collaboration on the study of particle correlations and single-particle spectra for non-relativistic, three-dimensionally expanding as well as for relativistic, one-dimensionally expanding or three-dimensionally expanding finite systems [Csö94b, Csö95e, Csö95a]. In these papers, it has been emphasized for the first time, that observation of the "true" sizes of particle sources is possible only if the single-particle spectra and the two-particle correlation functions

are simultaneously analyzed. The reason was also given: the HBT radii (effective sizes measured by correlation techniques) were found to be dominated by the shorter of the geometrical and the thermally induced lenght-scales, while the width of the rapidity distribution or the slope of the transverse mass distribution is found to be dominated by the longer of the geometrical and the thermal scales. The appearance of the thermal lenght-scales is related to flow and temperature gradients, i.e. to the change of the mean momentum of the emitted particles with changing the coordinates of the particle emission. Within a thermal radius, these changes are not bigger than the width of the local momentum distribution.

This important effect has been re-discovered by various other groups, as a consequence of the emerging simultaneous analysis of particle correlations and spectra, proposed first in 1994 by the Buda-Lund collaboration. The question arizes: Is it possible to uniquely determine the geometrical source radii ("true" source sizes) from a simultaneous analysis of particle correlations and spectra? This question is basically the same as the analogous question in the momentum space: Is it possible to uniquely determine the freeze-out temperature and the transverse flow from a simultaneous analysis of particle spectra and correlations?

We prove by an example that if the absolute normalization of particle spectra is *not* given, then it may be impossible to select from among different minima based only on the shape of the single-particle momentum-distribution and on the two-particle correlation functions.

We perform the analysis with the help of an analytically as well as numerically well studied model, the hydrodynamical parameterization of the Buda-Lund collaboration [Csö95a]. The domain of applicability of the analytical approximations is determined numerically in ref. [Csö95a] for this model. In ref. [Aga97], this model is shown to describe the single-particle spectra and the two-particle correlations at $(\pi/K) + p$ reactions at CERN SPS simultaneously.

The same model was tested in refs. [Csö95b, Csö95a] against the *prelim-*

inary NA44 data on $S + Pb$ reactions at CERN SPS, however, it was shown there that it is difficult to find unique, reliable values of the fit parameters. The sources of the difficulty are the lack of absolute normalization of spectra and the experimental difficulty of proper estimate of systematic errors. We know from earlier fitting of this model to spectra without absolute normalization [Csö95a], that the final results are rather sensitive to errors and normalizations. In fact, we compare here the two physically different minima, found by fitting the Buda-Lund hydro model of ref. [Csö95a] to NA44 preliminary data on $S + Pb$ central reactions at 200 AGeV. In ref. [Ste98] results were reported on fitting simultaneously the recently obtained absolutely normalized but still preliminary particle spectra and final correlations data for the same reaction as analysed in ref. [Csö95a].

In the next section the hydrodynamic model is presented, along with a new reparameterization of the basic formulas. An approximate analytic solution to this model is formulated in a new manner. For a comparision, a numerical approximation method is also schemed up. In the subsequent section, radius parameters and single particle spectra are calculated using the analytic and numeric methods. The transverse mass and the rapidity dependence of the results are shown for a substantial range of momentum space. The results are also used to make estimations to the systematic errors introduced by the particular approximations. Finally, we summarize and emphasize the importance of the experimental determination of the absolutely normalized single particle spectra.

4.2 The model and its re-parameterization

The hydrodynamic model of ref. [Csö95a] is briefly recapitulated below, in a general form. The analytic results are then reformulated with new notation. A numerical evaluation scheme is also summarized afterwards.

4.2.1 The model

The Buda-Lund model [Csö95a] model makes a difference between the central (core) and the outskirts (halo) regions of high energy reactions. The pions that are emitted from the core consist of two types: a) They could be emitted directly from the hadronization of wounded, string-like nucleons, rescattering with a typical 1 fm/c scattering time as they flow outwards. b) Alternatively, they could be produced from the decays of short-lived resonances such as ρ, N^*, Δ or K^*, whose decay time is also of the order of 1-2 fm/c. This core region of the particle source is resolvable by Bose-Einstein correlation measurements. In contrast, the halo region consists of decay products of long-lived resonances such as the ω, η, η' and K^0_S, whose decay time is greater than 20 fm/c. This halo is not resolvable by Bose-Einstein measurements with the present techniques, however, it is affecting the Bose-Einstein correlation functions by suppressing their strength.

In general, the following emission function $S_c(x,p)$ applies to a hydrodynamically evolving core of particle source:

$$S_c(x,p)\, d^4x \;=\; \frac{g}{(2\pi)^3} \frac{d^4\Sigma^\mu(x) p_\mu}{\exp\left(\dfrac{u^\mu(x)p_\mu}{T(x)} - \dfrac{\mu(x)}{T(x)}\right) + s}, \qquad (4.1)$$

where the subscript $_c$ refers to the core, the factor $d^4\Sigma^\mu(x)p_\mu$ describes the flux of particles through a finite, narrow layer of freeze-out hypersurfaces. The statistics is encoded by s, Bose-Einstein statistics corresponds to $s = -1$, Boltzmann approximation to $s = 0$ while the Fermi-Dirac statistics corresponds to $s = +1$. The four-momentum reads as $p = p^\mu = (E_{\mathbf{p}}, \mathbf{p})$. The four-coordinate vector reads as $x = x^\mu = (t, r_x, r_y, r_z)$. For cylindrically symmetric, three-dimensionally expanding, finite systems it is assumed that any of these layers can be labelled by a unique value of $\tau = \sqrt{t^2 - r_z^2}$, and the random variable τ is characterized by a probability distribution, such that

$$d^4\Sigma^\mu(x)p_\mu \;=\; m_t \cosh[\eta - y]\, H(\tau) d\tau\, \tau_0 d\eta\, dr_x\, dr_y. \qquad (4.2)$$

Here $m_t = \sqrt{m^2 + p_x^2 + p_y^2}$ stands for the transverse mass, the rapidity y and the space-time rapidity η are defined as $y = 0.5 \log\left[(E + p_z)/(E - p_z)\right]$ and $\eta = 0.5 \log\left[(t + r_z)/(t - r_z)\right]$ and the duration of particle emission is characterized by $H(\tau) \propto \exp(-(\tau - \tau_0)^2/(2\Delta\tau^2))$. Here τ_0 is the mean emission time, $\Delta\tau$ is the duration of the emission in (proper) time. The four-velocity and the local temperature and density profile of the expanding matter is given by

$$u^\mu(x) = \left(\cosh[\eta]\cosh[\eta_t],\, \sinh[\eta_t]\frac{r_x}{r_t},\, \sinh[\eta_t]\frac{r_y}{r_t},\, \sinh[\eta]\cosh[\eta_t]\right), \tag{4.3}$$

$$\sinh[\eta_t] = b\frac{r_t}{\tau_0}, \qquad r_t = \sqrt{r_x^2 + r_y^2}, \tag{4.4}$$

assuming a linear transverse flow profile. The inverse temperature profile is characterized by the central value and its variance in transverse and temporal direction, and we assume a Gaussian shape of the local density distribution:

$$\frac{1}{T(x)} = \frac{1}{T_0}\left(1 + a^2\,\frac{r_t^2}{2\tau_0^2}\right)\left(1 + d^2\,\frac{(\tau - \tau_0)^2}{2\tau_0^2}\right), \tag{4.5}$$

$$\frac{\mu(x)}{T(x)} = \frac{\mu_0}{T_0} - \frac{r_x^2 + r_y^2}{2R_G^2} - \frac{(\eta - y_0)^2}{2\Delta\eta^2}, \tag{4.6}$$

where $\mu(x)$ is the chemical potential and $T(x)$ is the local temperature characterizing the particle emission.

4.2.2 Core/halo correction

The effective intercept parameter $\lambda_*(y, m_t)$ of the Bose-Einstein correlation function measures the fraction of pions from the core versus the total number of pions at a given value of $\mathbf{p}$, when interpreted in the core/halo picture [Bol93, Csö94a, Csö97]. With this factor the total invariant spectrum in y rapidity and transverse mass m_t follows as

$$\frac{d^2n}{dy\,dm_t^2} = \frac{1}{\sqrt{\lambda_*}}\frac{d^2n_c}{dy\,dm_t^2} = \frac{1}{\pi\sqrt{\lambda_*}}\int S_c(x,p)\,d^4x. \tag{4.7}$$

The momentum dependence of λ_* parameter is to be measured by the experimental collaborations. The experimental determination of $\lambda_*(p)$ is very important not only because it gives a measure of the contribution of the core to the total number of particles at a given momentum, but also as it provides a measure of the mean transverse flow and a new signal of partial $U_A(1)$ symmetry restoration [Van98]. Therefore it is strongly recommended that experiments report this $\lambda_*(\mathbf{p})$ parameter of the Bose-Einstein correlation function and not just present partial fit results, like the momentum dependence of the radius parameters.

4.2.3 Re-parameterization

The original version of the core model contains 3 dimensionless parameters, a, b and d, that control the transverse decrease of the temperature field, the strength of the (linear) transverse flow profile and the temporal changes of the temperature field, respectively, keeping only the mean and the variances of the inverse temperature distributions. These are very useful in obtaining simple formulas, however, they make the interpretation of the fit results less transparent. Hence we re-express them with new parameters with more direct physical meaning.

The surface temperature is introduced as $T_r = T(r_x = r_y = R_G, \tau = \tau_0)$ and the "post-freeze-out" temperature denotes the local temperature after most of the freeze-out process is over, $T_t = T(r_x = r_y = 0; \tau = \tau_0 + \sqrt{2}\Delta\tau)$. Here R_G stands for the transverse geometrical radius of the source, τ_0 denotes the mean freeze-out time, $\Delta\tau$ is the duration of the particle emission and we denote the temperature field by $T(x)$. The central temperature at mean freeze-out time is denoted by $T_0 = T(r_x = r_y = 0; \tau = \tau_0)$.

Then the relative transverse and temporal temperature decrease can be introduced as

$$\langle \Delta T/T \rangle_r \;=\; \frac{T_0 - T_r}{T_r}, \tag{4.8}$$

$$\langle \Delta T/T \rangle_t \;=\; \frac{T_0 - T_t}{T_t}, \tag{4.9}$$

and it is worthwhile to introduce the mean transverse flow as the transverse flow at the geometrical radius as

$$\langle u_t \rangle = b\,\frac{R_G}{\tau_0}. \tag{4.10}$$

The dimensionless model parameters can thus be expressed with these new, physically more straightforward parameters as

$$a^2 \;=\; \frac{\tau_0^2}{R_G^2}\,\langle \Delta T/T \rangle_r, \tag{4.11}$$

$$b \;=\; \frac{\tau_0}{R_G}\,\langle u_t \rangle, \tag{4.12}$$

$$d^2 \;=\; \frac{\tau_0^2}{\Delta\tau^2}\,\langle \Delta T/T \rangle_t. \tag{4.13}$$

Note, that eqs. (4.8) and (4.10) were introduced earlier in ref. [Aga97] also to simplify the interpretation of data fitting. We present the complete re-parameterization herewith, including egs. (4.9) and the re-parameterization of both the radius parameters and single-particle spectra.

Note:

$$\frac{1}{\tau_0} \;=\; H_l, \tag{4.14}$$

$$\frac{\langle u_t \rangle}{R_G} \;=\; H_t. \tag{4.15}$$

This way the longitudinal and transverse Hubble constants can be introduced, but they are not used in this chapter.

4.2.4 Analytic approximations

In Ref. [Csö95a], the Boltzmann approximation to the above emission function was evaluated in an analytical manner, applying approximations around the saddle point of the emission function. The resulting formulas express the Invariant Momentum Distribution (IMD) and the Bose-Einstein correlation

function (BECF). Now we re-express the formulas given in ref. [Csö95a] with the help of our new parameters.

The particle spectra can be expressed in the following simple form:

$$N(\mathbf{p}) = \frac{g}{(2\pi)^3}\,\overline{E}\,\overline{V}\,\overline{C}\,\exp\left(-\frac{p\cdot u(\overline{x})-\mu(\overline{x})}{T(\overline{x})}\right), \tag{4.16}$$

$$\overline{E} = m_t\cosh(\overline{\eta}), \tag{4.17}$$

$$\overline{V} = (2\pi)^{(3/2)}\,\overline{R_\parallel}\,\overline{R_\perp}^2\,\frac{\overline{\Delta\tau}}{\Delta\tau}, \tag{4.18}$$

$$\overline{C} = \frac{1}{\sqrt{\lambda_*}}\,\exp\left(\frac{\overline{\Delta\eta}^2}{2}\right). \tag{4.19}$$

Here the quantity $\overline{x}$ stands for the average value of the space-time four-vector parameterized by $(\overline{\tau},\overline{\eta},\overline{r_x},\overline{r_y})$, denoting longitudinal proper-time, space-time rapidity and transverse directions. These values are given as

$$\overline{\tau} = \tau_0, \tag{4.20}$$

$$\overline{\eta} = \frac{y_0-y}{1+\Delta\eta^2\dfrac{m_t}{T_0}}, \tag{4.21}$$

$$\overline{r_x} = \langle u_t\rangle R_G\frac{p_t}{T_0+\overline{E}\,(\langle u_t\rangle+\langle\,\Delta T/T\rangle_r)}, \tag{4.22}$$

$$\overline{r_y} = 0. \tag{4.23}$$

$\overline{E}$ denotes the energy of a particle from the center of particle emission, measured in the Longitudinal Center of Mass System (LCMS) frame. The effective volume is denoted by $\overline{V}$, see below for details, and the correction factor $\overline{C}$ takes into account the effects of long-lived resonances and the deviation of the saddle-point result from the more possible naive expectation, which would be the same expression with $\overline{C}=1$. The notation $\overline{a}$ denotes an invariant quantity a, that depends on $y-y_0$, m_t, T and the other parameters of the model in a boost-invariant manner. In ref. [Csö95a] this was denoted by $\overline{a_*}$, for example, $\overline{\Delta\eta}$ in the present paper was denoted by $\overline{\Delta\eta_*}$. The average

invariant volume of particle emission in eqs. (4.16,4.18) is given by $\overline{V}$ that is in our case the product of the average (momentum-dependent) transverse area ($2\pi\overline{R_\perp}^2$), the average (momentum-dependent) longitudinal source size $(2\pi)^{1/2}\overline{R_\parallel}$. The averaging of the size of the effective volume over the duration of particle emission is expressed by the factor $\dfrac{\overline{\Delta\tau}}{\Delta\tau}$. These quantities read as

$$\overline{\Delta\tau}^2 = \frac{\Delta\tau^2}{1+\langle\Delta T/T\rangle_r\dfrac{\overline{E}}{T_0}}, \tag{4.24}$$

$$\overline{\Delta\eta}^2 = \frac{\Delta\eta^2}{1+\Delta\eta^2\dfrac{\overline{E}}{T_0}}, \tag{4.25}$$

$$\overline{R_\parallel}^2 = \overline{\tau}^2\,\overline{\Delta\eta}^2, \tag{4.26}$$

$$\overline{R_\perp}^2 = \frac{R_G^2}{1+\left(\langle u_t\rangle^2+\langle\Delta T/T\rangle_r\right)\dfrac{\overline{E}}{T_0}}. \tag{4.27}$$

$$\tag{4.28}$$

This completes the specification of the shape of particle spectrum. These results correspond to the equations given in ref. [Csö95a] although they are re-expressed with new combination of the variables. Please note that the Boltzmann-factor can be expressed approximately as

$$\exp\left(-\frac{p\cdot u(\overline{x})-\mu(\overline{x})}{T(\overline{x})}\right) \simeq \exp\left[\frac{\mu_0}{T_0}-\frac{(y-y_0)^2}{2(\Delta\eta^2+T_0/m_t)}\right]\exp\left[-\frac{m_t}{T_0}\right]\times \times\exp\left[\frac{\langle u_t\rangle^2(m_t^2-m^2)}{2T_0\left[T_0+m_t(\langle u_t\rangle^2+\langle\Delta T/T\rangle_r)\right]}\right]. \tag{4.29}$$

The HBT radius parameters were evaluated in ref. [Csö95a] in the following way: the space-time rapidity η_s was defined as the solution of the equation

$$\frac{\partial S(\eta_s)}{\partial\eta}=0. \tag{4.30}$$

The Longitudinal Saddle Point System (LSPS) was introduced as the frame where $\eta_s = 0$. At the so-called saddle-point one has

$$\frac{\partial S}{\partial \tau} = \frac{\partial S}{\partial \eta} = \frac{\partial S}{\partial r_x} = \frac{\partial S}{\partial r_y} = 0. \tag{4.31}$$

This resulted in a set of transcendental equations for the position of the saddle-point. These equations for the positions were solved approximatelly with the help of an expansion of the transcendental equation in terms of small parameters, like the deviation of η_s from the mean rapidity of the pair. The calculation resulted in the following value for η_s:

$$\eta_s = y + \frac{y_0 - y}{1 + \Delta\eta^2(\frac{m_t}{T_0} - 1)}. \tag{4.32}$$

Hence the relative rapidity of the LSPS frame as compared to the LCMS frame is

$$\eta_s^L = \frac{y_0 - y}{1 + \Delta\eta^2(\frac{m_t}{T_0} - 1)}. \tag{4.33}$$

Note that LCMS is the frame where the rapidity belonging to the mean momentum of the pair vanishes, $y = 0$ [Csö91]. In ref. [Csö95a] this quantity was denoted by the slightly more complicated notation $\eta_s^{LCMS} = \eta_s^L$, and the maximum of the Boltzmann factor, which in our present notation reads as $\overline{\eta} = \overline{\eta_s}$ and stands for a modified saddle-point, used for the calculation of the particle spectra in ref. [Csö95a]. Note that η_s^L may deviate from $\overline{\eta}$ substantially at low values of m_t, especially if $T > m$.

This frame, defined by the maximum of the Boltzmann factor, given by $\overline{\eta}$ in the LCMS, plays a key role in the calculations. Hence this frame, introduced in ref. [Csö95a] without a name, deserves a name. We suggest Longitudinal Boltzmann Center System (LBCS). In general, this LBCS frame is defined by the solution of the

$$\frac{\partial f_B(\overline{\eta})}{\partial \eta} = 0 \tag{4.34}$$

equation, where $f_B = \exp\left(-[pu(x) - \mu(x)]/T(x)\right)$ stands for the Boltzmann factor only, but does not include the Cooper-Frye flux term.

In ref. [Csö95a] the spectrum was evaluated in the LBCS frame, while the correlation functions in the LSPS frame. Let us recapitulate the results for the two-particle correlation functions: The mean momentum is denoted by $K = (p_1 + p_2)/2$, its components are $(K_0, K_L, K_t, 0)$ in the (t, r_z, r_x, r_y) reference frame. The transverse velocity β_t reads as

$$\beta_t = \frac{K_t}{K_0} = \frac{K_t}{M_t}\frac{1}{\cosh(y)} = \frac{V_t}{\cosh(y)}. \tag{4.35}$$

The effective source parameters are obtained as

$$\frac{1}{\Delta\eta_*^2} = \frac{1}{\overline{\Delta\eta}^2(\overline{\eta} \to \eta_s^L)} - \frac{1}{\cosh^2(\eta_s^L)}, \tag{4.36}$$

$$R_\parallel^2 = \tau_s^2\Delta\eta_*^2 = \tau_s^2\overline{\Delta\eta}^2(\overline{\eta} \to \eta_s^L), \tag{4.37}$$

$$R_\perp^2 = R_*^2 = \overline{R_\perp}^2(\overline{\eta} \to \eta_s^L), \tag{4.38}$$

$$R_\tau^2 = \Delta\tau_*^2 = \overline{\Delta\tau}^2(\overline{\eta} \to \eta_s^L). \tag{4.39}$$

The modified position of the maximal emissivity is given in the LCMS frame by $(\tau_s, \eta_s, r_{x,s}, 0)$, where

$$r_{x,s} = \overline{r_x}(\overline{\eta} \to \eta_s^L), \tag{4.40}$$

$$\tau_s = \overline{\tau} = \tau_0. \tag{4.41}$$

This notation means that, for example, $\Delta\eta_*$ corresponds to the function $\overline{\Delta\eta}$ when the variable $\overline{\eta}$ is replaced by the quantity η_s^L. Note, that $\Delta\eta_*$ corresponds to the effective space-time rapidity width of the particle emission function in an LSPS calculation, while $\overline{\Delta\eta}$ corresponds to the width of the Boltzmann-factor only in the LBCS frame. Similar relations hold for $\overline{R}$ and R_*, $\overline{\Delta\tau}$ and $\Delta\tau_*$. The Bose-Einstein correlation functions can be written in the so-called Bertsch-Pratt side-out-long ref. frame as

$$C(\Delta k, K) = 1 + \lambda_* \exp\left(-R_{side}^2 Q_{side}^2 - R_{out}^2 Q_{out}^2 - R_L^2 Q_L^2\right) \times \times \exp\left(-R_{out,L}^2 Q_L Q_{out}\right), \tag{4.42}$$

$$\tag{4.43}$$

$$R_{side}^2 = R_\perp^2 = R_*^2, \tag{4.44}$$

$$R_{out}^2 = R_{side}^2 + \delta R_{out}^2, \tag{4.45}$$

$$\delta R_{out}^2 = \frac{V_t^2}{\cosh^2(y)} \left[\cosh^2(\eta_s) R_\tau^2 + \sinh^2(\eta_s) R_\parallel^2\right], \tag{4.46}$$

$$R_L^2 = \frac{1}{\cosh^2(y)} \left[\cosh^2(\eta_s^L) R_\parallel^2 + \sinh^2(\eta_s^L) R_\tau^2\right], \tag{4.47}$$

$$R_{out,L}^2 = -\frac{V_t}{\cosh^2(y)} \left[\cosh(\eta_s)\sinh(\eta_s^L) R_\tau^2 + \sinh(\eta_s)\cosh(\eta_s^L) R_\parallel^2\right]. \tag{4.48}$$

Here we have utilized the form of equations given in ref. [Csö95a] and the transformation of K_L to $M_t \cosh(y)$ as introduced in ref. [Vol96].

Although the two-particle Bose-Einstein correlation function is manifestly covariant [Vol96], its Bertsch-Pratt parameterization is frame-dependent. A possible covariant parameterization [Yan78, Pod83], was applied to the particle interferometry by the Regensburg group [Cha95b, Wu98]. We find that the simplest possible covariant generalization is not exactly the YKP parameterization, but the formulation given by the Buda-Lund collaboration in ref. [Csö95a], see especially eqs. (44) and (21-26) of ref. [Csö95a]. Here we repeat only the results after Gaussian approximation to the source function:

$$C(\Delta k, K) = 1 + \lambda_* \exp(-Q_\tau^2 R_\tau^2 - Q_\eta^2 R_\parallel^2 - Q_t^2 R_*^2), \tag{4.49}$$

$$Q_t^2 = Q_{side}^2 + Q_{out}^2, \tag{4.50}$$

$$Q_\tau = Q \cdot n(x_s^L) = Q_0 \cosh(\eta_s^L) - Q_z \sinh(\eta_s^L), \tag{4.51}$$

$$Q_\eta = \sqrt{Q \cdot Q - (Q \cdot n(x_s^L))^2 - Q_t^2} = Q_0 \sinh(\eta_s^L) - Q_z \cosh(\eta_s^L). \tag{4.52}$$

where $n(x_s^L) = (\cosh(\eta_s^L), 0, 0, \sinh(\eta_s^L))$ is a normal-vector at x_s in LCMS. Note, that this formulation is equivalent with the YKP formulation, however the correlation function is given by a simple purely quadratic form in the present formulation, in contrast to the YKP expression, where the invariant relative momentum combination Q_η is written out explicitely in terms of its non-invariant components.

4.2.5 Numeric approximations

Approximate single particle spectra and Bose-Einstein correlation functions can be calculated by numerical integration of equation (1), as well, expressing the means and the variances of the hydrodynamically evolving core of particle emission. The original method of 'means and variances' was proposed first by the Regensburg group in ref. [Cha95]. We shall utilize herewith the core/halo corrected version of these relations as given recently in ref. [Nic97]. The limitation of these approximations is discussed in refs. [Csö95a, Nic97]. For example, possible double-Gaussian structures or non-Gaussian features are neglected in this approximation. The analytic approximation yields Gaussian functions in proper time τ and space-time rapidity η, hence includes a deviation from Gaussian shape in t and z. The numerical approximation assumes Gaussian forms in t and z that is not so well suited to the kinematics of ultra-relativistic reactions as Gaussians in τ and η. The spectra and the HBT radius parameters are defined in the Gaussian core/halo model approximation as follows:

$$C(\mathbf{K},\mathbf{\Delta k}) = 1+\lambda_*(\mathbf{K})\,\exp\left(-R^2_{i,j}(\mathbf{K})\mathbf{\Delta k}_i\mathbf{\Delta k}_j\right), \tag{4.53}$$

$$\lambda_*(\mathbf{K}) = [N_{\mathbf{c}}(\mathbf{K})/N(\mathbf{K})]^2, \tag{4.54}$$

$$R^2_{i,j}(\mathbf{K}) = \langle(x_i-\beta_i t)(x_j-\beta_j t)\rangle_{\mathbf{c}} - \langle(x_i-\beta_i t)\rangle_{\mathbf{c}}\langle(x_j-\beta_j t)\rangle_{\mathbf{c}} \tag{4.55}$$

$$\langle f(x,\mathbf{K})\rangle_{\mathbf{c}} = \int d^4x f(x,\mathbf{K})S_{\mathbf{c}}(x,\mathbf{K}), \tag{4.56}$$

where $i,j = side, out$ or $long$ as before, and $S_{\mathbf{c}}(x,\mathbf{K})$ is the emission function that characterizes the central core, as given by eq. 4.1. The mean momentum is defined as $\mathbf{K} = 0.5(\mathbf{p}_1+\mathbf{p}_2)$, the relative momentum is given by $\mathbf{\Delta k} = \mathbf{p}_1-\mathbf{p}_2$. The spectra of all the bosons and the spectra of the bosons from the core described as

$$N(\mathbf{p}) = \langle 1\rangle = \int d^4x\left[S_{\mathbf{c}}(x,\mathbf{p})+S_{halo}(x,\mathbf{p})\right], \tag{4.57}$$

$$N(\mathbf{p})_{\mathbf{c}} = \langle 1\rangle_{\mathbf{c}} = \int d^4x S_{\mathbf{c}}(x,\mathbf{p}). \tag{4.58}$$

In this picture, the reduction of the intercept parameter is the only effect on the correlation function that stems from the halo, the variances of the core correspond to the Gaussian core/halo model radii of the measured correlation function. Although the above expressions are formally similar to the original version of Gaussian model-independent radii of ref. [Cha95], they cannot be obtained with an expansion around $Q = 0$, as they correspond to a large Q expansion of the Bose-Einstein correlation function [Mis96, Nic97].

4.3 Calculating observables

Both analytic and numeric approximations were used to calculate and show the momentum dependence of the observables from the hydrodynamical model of ref. [Csö95a]. These observables are the effective radius parameters (HBT radii), the shape and the slope of the single-particle spectra. Figures are drawn for two very different sets of source parameters (or model parameters). To recall, the particle source is characterized by the means and the variances of the density distribution, the inverse temperature distribution and a linear flow. This yields 9 free parameters, μ_0, T_0, τ_0, R_G, $\Delta\tau$, $\Delta\eta$, $\langle\Delta T/T\rangle_r$, $\langle u_t\rangle$, $\langle\Delta T/T\rangle_t$, respectively.

The examined momentum space is divided into 40x40 sub-intervals in m_t and y dimensions, respectively, that allowed for fine resolution of the distributions. As a drawback, with such a resolution the numeric integration version takes much longer time than the analytic one. In the presented case generation of data took 10 hours for one run. Scales on the pictures are kept the same for the same kind of distributions except for the average emisson rate that differs remarkably for the two sets of model parameters. The actual parameter set values (with $\mu_0 = 0$) used in the particular calculations are indicated below each drawing and they are denoted by names Source Parameters Set 1 and Source Parameter Set 2. Parameter Set 1 was obtained from a ref. [Ste98] , fitting absolutely normalized spectra in the NA44 acceptance, while Parameter Set 2 was obtanined in ref. [Csö95a], fitting unnormalized preliminary particle spectra together with correlation data. Note that one

can distinguish between different model parameters only if the value of μ_0 is known from other observations than the ones already exploited in the present analysis.

4.3.1 Analytic results

The two model parameter sets mentioned above were applied to the analytic expressions formulated in the previous section by eqs. (4.16) to (4.48). See Figs. 4.1 and 4.2 for details of the momentum space distributions of the observables. Notice the substantial difference of the particle spectra for Parameter Set 1 and Parameter Set 2. Also notice the deviations of the radius parameters at small m_t and at large relative rapidities to midrapidity for the two different source parameter sets. Along with the comparision to the numeric results later this reflects the limitations of this kind of approximation.

4.3.2 Numeric results

The numerically evaluated HBT radius parameters and single particle spectra are obtained from the eqs. (4.53,4.55,4.57,4.58), utilizing the Boltzmann approximation to the source function of eq. (4.1). Note that this scheme is not an exact calculation, but an approximation in a different way than the analytic approach, therefore it is suitable to estimate the systematic errors of the model parameters and to cross-check the uniqueness of the minimum in fitting the model to experimental data. See Figs. 4.3 and 4.4 for details of HBT radius parameter distributions as well as single particle spectra in this approximation scheme.

4.3.3 Differencies between the analytic and the numeric results

The differencies between the observables as calculated from the two sorts of model approximations are presented on Figs. 4.5 and 4.6. From these drawings one can learn the critical ranges where the two approximation schemes differ from each other beyond a given tolerance level.

Figs. 4.5 and 4.6 show the rapidity and transverse mass dependence of the relative deviations between the analytic and the numeric approximations. For example, let us consider the top left panel of Figs. 4.5. On this panel, the relative deviation of the numerical and analytic approximations for the side radius component is evaluated in the following manner: The analytical result for a (y, m_t) bin i is denoted by a_i, the numerical result is denoted by n_i. Then the relative deviation between the two approximation schemes is defined as

$$\frac{\delta^2 a_i}{a_i^2} = \frac{(a_i - n_i)^2}{a_i^2}, \tag{4.59}$$

which is plotted on the top left panel for the side radius parameter and in subsequent panels for the out, long and cross term, the spectra and the slope of the spectra on the subsequent panels. This quantity will be understood and estimated in the next subsection as a function of some small expansion parameters, that are analytically obtainable for any set of source parameters. In turn, this result can be utilized to improve the fits of the analytic expressions to measured data.

4.3.4 Estimating systematic errors of approximations

The aim of the present subsection is to analytically understand the systematic errors on the analytic approximations that we utilize to evaluate the spectra and the HBT radius parameters.

In a fit with the analytic approximations, the χ^2 of the fit is given as

$$\chi_a^2 = \sum_i \frac{(d_i - a_i)^2}{e_i^2}, \tag{4.60}$$

where d_i denotes the measured data point at a given bin, for example, $R_{side}(y_i, m_{t,i})$, and the experimental error on this quantity is given by e_i. A numeric fit to the same data minimizes the following

$$\chi_n^2 = \sum_i \frac{(d_i - n_i)^2}{e_i^2} \tag{4.61}$$

numeric χ^2_n distribution. This may have different minima for the model parameters from the minima of χ^2_a. However, the χ^2_n distribution can be approximately reconstructed from an analytic fit, as follows:

$$\chi^2_n \simeq \chi^2_a + \delta\chi^2_a, \tag{4.62}$$

$$\delta\chi^2_a = \sum_i \frac{\delta^2 a_i}{e_i^2} = \sum_i \delta^2 A_i \frac{a_i^2}{e_i^2}, \tag{4.63}$$

where $\delta^2 a_i = (a_i - n_i)^2$ is the difference between the analytic and numeric result, and can be regarded as the systematic error of the analytic approximation, while the relative systematic error of the analytic calculation is $\delta^2 A_i = \frac{\delta^2 a_i}{a_i^2}$. (Keep in mind that a_i can be any of the analytically evaluated radius parameters or analytic result for the particle spectra). Our purpose is to obtain approximate analytical expressions for the relative error of the analytical approximations, $\delta^2 A_i$. These quantities are shown in Figs. 4.5 and 4.6.

Figs. 4.1 and 4.2 indicate large relative errors in certain regions of the (y, m_t) plane. These regions coincide with the regions where the so called small expansion parameters [Csö95a] of the model start to reach values close to 1. The analytic expressions for the observables (HBT radius parameters and single-particle spectra) were obtained in ref. [Csö95a] under the condition that the parameters $(\eta_s^L, \Delta\eta_*, r_{x,s}/\tau_0)$ are all much less than 1. This was due to the approximate nature of the solution of the saddle-point equations, and the expansion of the transcendental equations in terms of these small parameters. Figs. 4.7 and 4.8 show the (y, m_t) dependence of these small parameters and their squares. We observe the expected similarities to the distributions of the relative errors $\delta^2 A_i$, Figs. 4.5 and 4.6. The different small parameters become large in well separated domains of the momentum space (typically below 100MeV and above 1 GeV), e.g. η_s^L at small m_t and large $|y - y_0|$, $\Delta\eta_*$ at small m_t and small $|y - y_0|$, $r_{x,s}/\tau_0$ at large m_t independently of y. As a consequence, the relative errors of the analytic approximations for any radius parameter or momentum distribution can be parameterized as a

linear combination of the squared small parameters:

$$\delta^2 A = c_1^A(\eta_s^L)^2 + c_2^A \Delta\eta_*^2 + c_3^A(r_{x,s}/\tau_0)^2. \tag{4.64}$$

The three constants (c_1^A, c_2^A, c_3^A) are determined for the observables $A = R_{side}$, R_{out}, R_{long}, $R^2_{out-long}$, $N(\mathbf{p})$, $T_{eff}(y, m_t)$. Since the small parameters are expressed as a function of the model parameters or "true" source parameters, eqs. (4.37-4.39), the desired analytical formula for all the systematic errors of the evaluation of all these 6 observables is given in the form of eq. (4.64).

Note that the region, where the analytic expressions are most precise, corresponds to a curved region in the (y, m_t) plane, that at low m_t starts off-mid-rapidity and at high m_t shifts to mid-rapidity, in case of pions. This region almost exactly coincides with NA44 acceptance for pions. For heavier particles all the 3 small parameters decrease substancially. The analytic calculation is thus more precise for heavier particles than for pions.

For determining the numerical coefficients c_i^A, the distributions of the differencies on Figs. 4.5 and 4.6 the CERN optimizing package MINUIT was used [Min92]. MINUIT finds the minimum value of a multi-parameter function and it analyzes the shape of the function around the minimum. The fitted error distributions in terms of the small parameters are shown on Figs. 4.9 to 4.12 together with the best estimates of the systematic errors with the help of eq. 4.64. The coefficients c_i^A of the parameterized systematic error distributions along with their errors are shown in Tables 4.1 and 4.2.

Note that the coefficients c_i^A are found to be only weakly dependent on the source parameter sets for most of the cases, they are all smaller then the coefficents for Parameter Set 1 multiplied by 2. On Fig. 4.11, the fit of $(\delta N(p)/N(p))^2$ reflects the effect that above 0.5 MeV the calculation was forced to take the amplitudes with low weight due to the fact that the absolute values of $N(p)$ are very small in this range.

4.4 Results on the precision evaluation of analytic and numeric calculations

The first combined HBT and spectrum analysis, reported by the Buda-Lund collaboration in 1994-95, is re-visited here for the purpose of a systematic numerical and analytical evaluation of the model. We identified the regions in the rapidity - transverse mass plane where the analytic approximations and the numerical ones deviate from each other. These regions were found to coincide with the regions where the small expansion parameters of the analytic approximation start to grow significantly. The deviation between the analytical and the numerical results is characterized by positive definite quadratic polinomials built up from the small parameters. We find that the NA44 acceptance is ideally suited for the precise evaluation of the Buda-Lund model.

As a by-product we find that the parameters of the Bose-Einstein correlation functions as well as the shape and the slope parameters of the double differential invariant momentum distribution are similar within 10% for two physically very different model parameter value sets in the momentum space domain where the approximations are valid. However, these sets result in a factor of 7 - 10 difference in the absolute normalization of the single-particle spectra. Hence, it is strongly recommended to publish the experimentally measured single-particle spectra with their absolute normalization for future CERN and RHIC heavy ion experiments, for as many type of particles as possible, as a two-dimentional function of y, m_t. Figs. 4.1 and 4.4 illustrate that the y and the m_t dependence of $N(y, m_t)$ can not be factorized.

Of course, our *example* of two physically different parameter sets resulting in similar correlations and unnormalized spectra does not imply that such similarity is achieved for *any* two different parameter sets. The role of each parameter can be investigated, for instance, analytically like in ref. [Csö95a]. The typical behaviour that one expects is that for different values of the model parameters the particle correlations and spectra are different. We

would like to remind the readers that the existence of certain scaling limiting cases was pointed out also in ref. [Csö95a], where the dependence of the HBT radii on some of the model parameters was analytically shown to vanish in certain domains of the parameter space.

Note that the intercept parameter of the correlation function is included in the core/halo correction factor, hence it is also strongly recommended to publish the experimental HBT results including a momentum-dependent determination of λ_*, too.

$\delta^2 A$	c_1^A	c_2^A	c_3^A
$(\delta R_{side}/R_{side})^2$	0.015 ± 0.001	0.003 ± 0.001	0.002 ± 0.001
$(\delta R_{out}/R_{out})^2$	0.013 ± 0.001	0.001 ± 0.001	0.039 ± 0.001
$(\delta R_{long}/R_{long})^2$	0.027 ± 0.001	0.014 ± 0.001	0.032 ± 0.001
$(\delta R^2_{outl}/R^2_{outl})^2$	0.130 ± 0.001	0.208 ± 0.001	0.001 ± 0.001
$(\delta N(p)/N(p))^2$	0.014 ± 0.001	0.044 ± 0.001	0.015 ± 0.001
$(\delta T_{eff}/T_{eff})^2$	0.006 ± 0.001	0.042 ± 0.001	0.001 ± 0.001

Table 4.1: Coefficients c_i^A of the parameterized systematic error distributions for Source Parameter Set 1.

$\delta^2 A$	c_1^A	c_2^A	c_3^A
$(\delta R_{side}/R_{side})^2$	0.001 ± 0.001	0.007 ± 0.001	0.003 ± 0.001
$(\delta R_{out}/R_{out})^2$	0.008 ± 0.001	0.002 ± 0.001	0.001 ± 0.001
$(\delta R_{long}/R_{long})^2$	0.018 ± 0.001	0.024 ± 0.001	0.031 ± 0.001
$(\delta R^2_{outl}/R^2_{outl})^2$	0.154 ± 0.003	0.398 ± 0.002	0.001 ± 0.001
$(\delta N(p)/N(p))^2$	0.035 ± 0.001	0.052 ± 0.001	0.001 ± 0.001
$(\delta T_{eff}/T_{eff})^2$	0.012 ± 0.001	0.042 ± 0.001	0.001 ± 0.001

Table 4.2: Coefficients c_i^A of the parameterized systematic error distributions for Source Parameter Set 2.

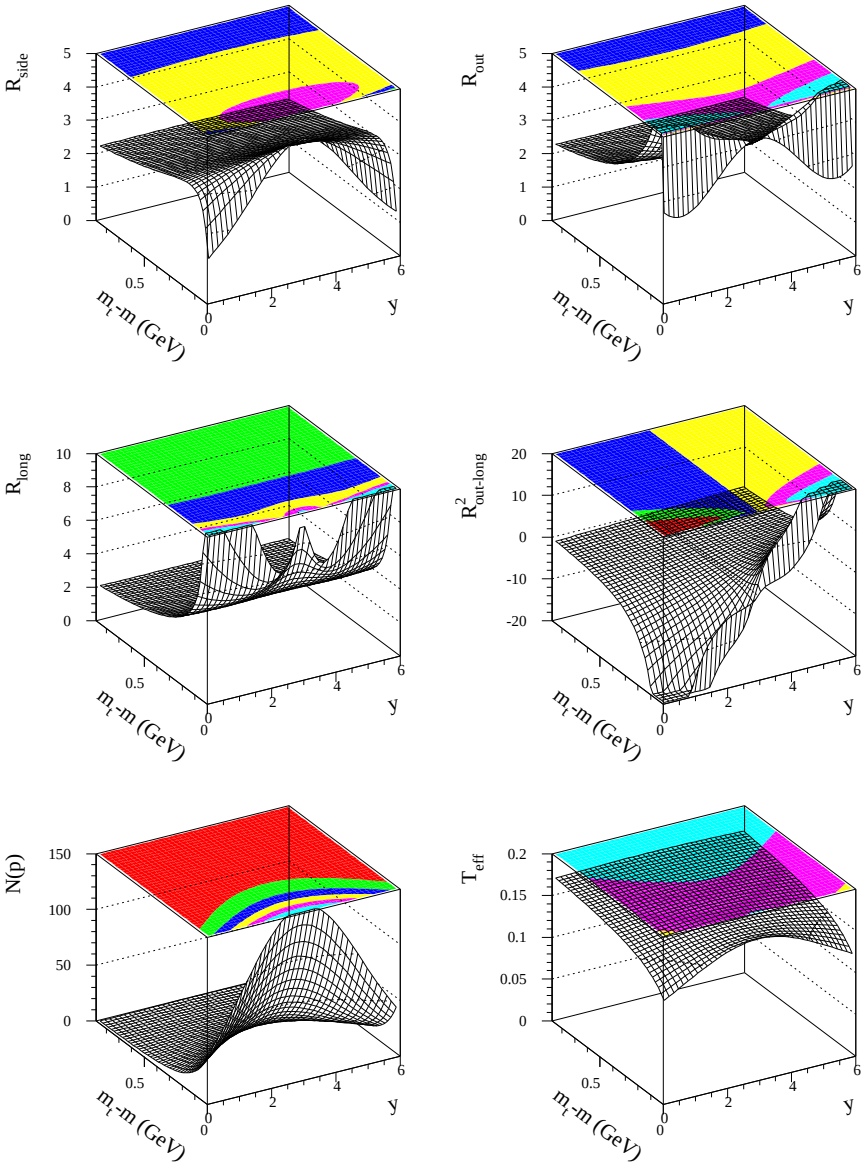

ANALYTIC Source Parameter Set 1

τ_0 = 5.1 fm/c	T_0 = 154 MeV	T_r = 106 MeV	$\Delta\eta$= 1.6
$\Delta\tau$= 0.3 fm/c	m = 140 MeV	T_t = 142 MeV	y_0 = 3
R_g = 5.4 fm	g = 3	u_t = 0.52	

Figure 4.1: Simultaneous results for particle spectra and HBT radius parameters. The analytic approximations were utilized to evaluate the model for Parameter Set 1.

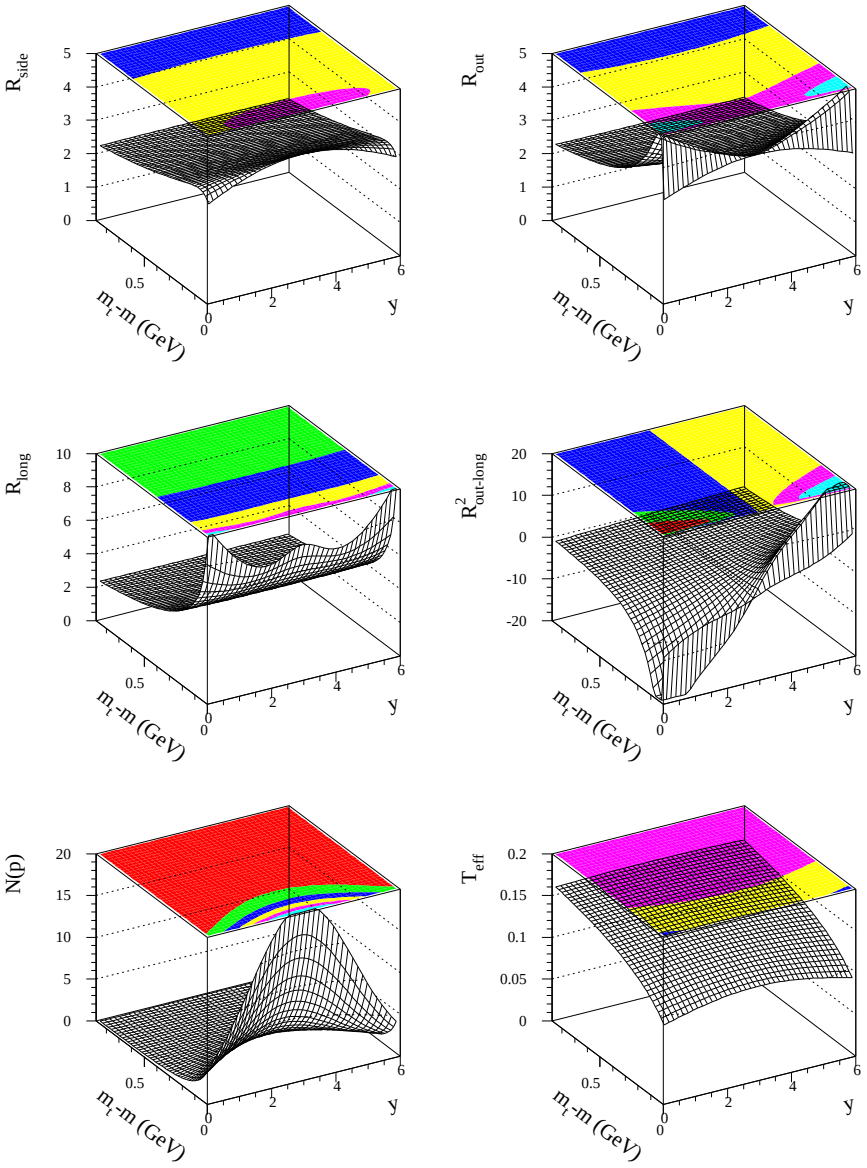

ANALYTIC Source Parameter Set 2

τ_0 =	7	fm/c	T_0 =	108	MeV	T_r = 104 MeV	$\Delta\eta$= 1.48
$\Delta\tau$=	2.34	fm/c	m =	140	MeV	T_t = 6 MeV	y_0 = 3
R_g =	4.4	fm	g =	3		u_t = 0.51	

Figure 4.2: Simultaneous results for particle spectra and HBT radius parameters. The analytic approximations were utilized to evaluate the model for Parameter Set 2.

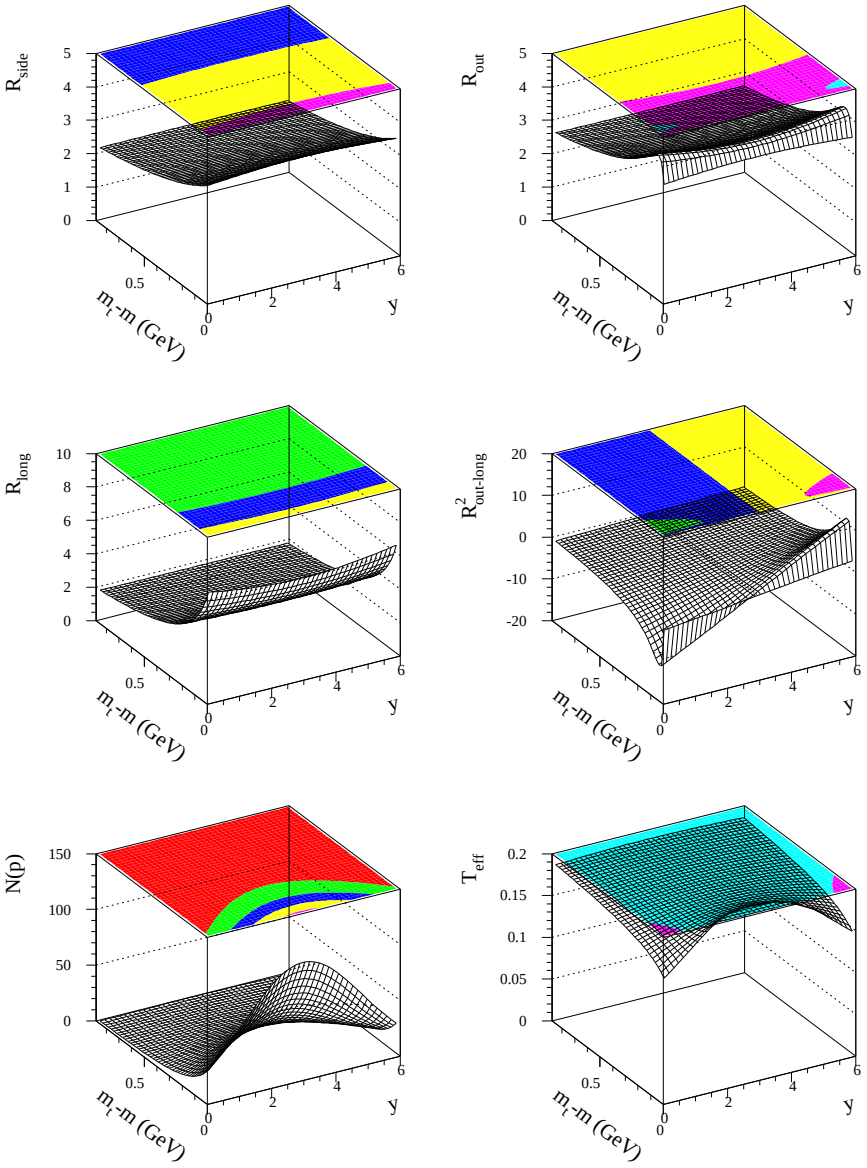

NUMERIC Source Parameter Set 1

τ_0 = 5.1 fm/c	T_0 = 154 MeV	T_r = 106 MeV	$\Delta\eta$ = 1.6
$\Delta\tau$ = 0.3 fm/c	m = 140 MeV	T_t = 142 MeV	y_0 = 3
R_g = 5.4 fm	g = 3	u_t = 0.52	

Figure 4.3: Simultaneous results for particle spectra and HBT radius parameters. The numeric approximations were utilized to evaluate the model for Parameter Set 1.

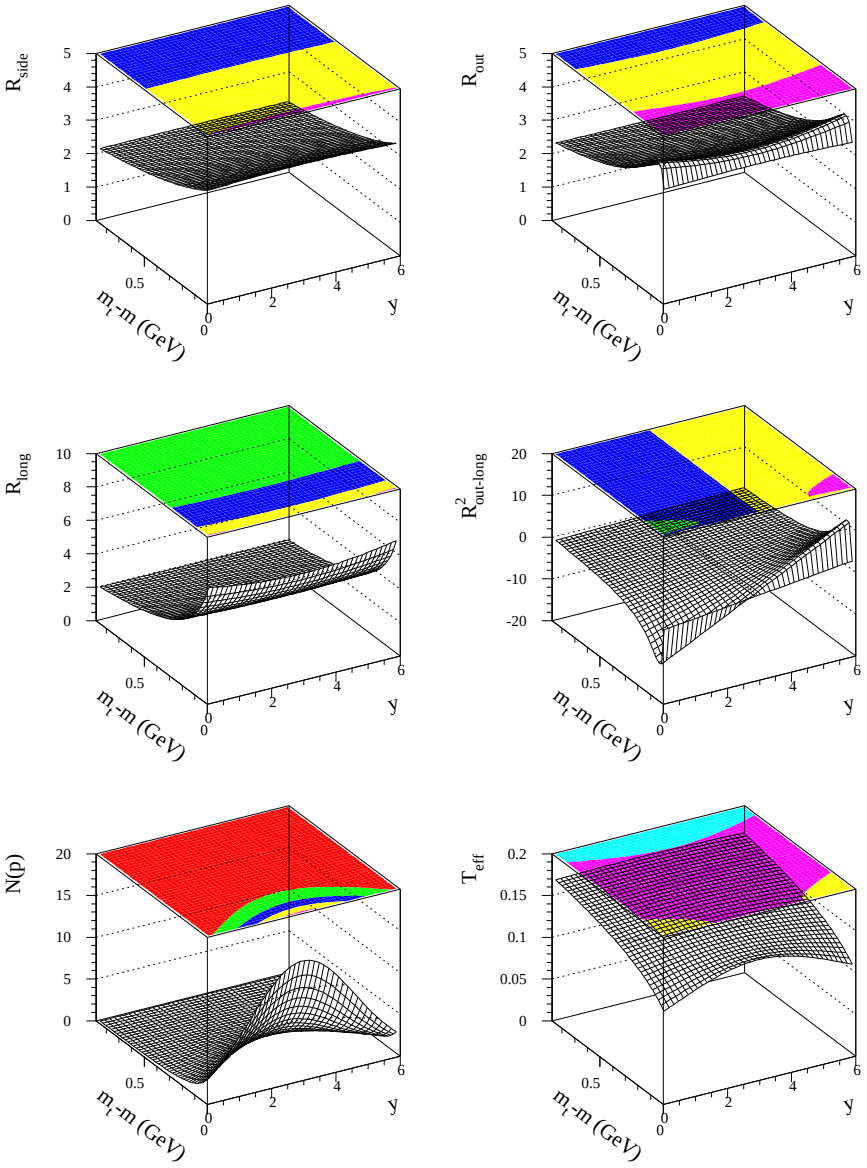

NUMERIC Source Parameter Set 2

τ_0 = 7 fm/c	T_0 = 108 MeV	T_r = 104 MeV	$\Delta\eta$ = 1.48
$\Delta\tau$ = 2.34 fm/c	m = 140 MeV	T_t = 6 MeV	y_0 = 3
R_g = 4.4 fm	g = 3	u_t = 0.51	

Figure 4.4: Simultaneous results for particle spectra and HBT radius parameters. The numeric approximations were utilized to evaluate the model for Parameter Set 2.

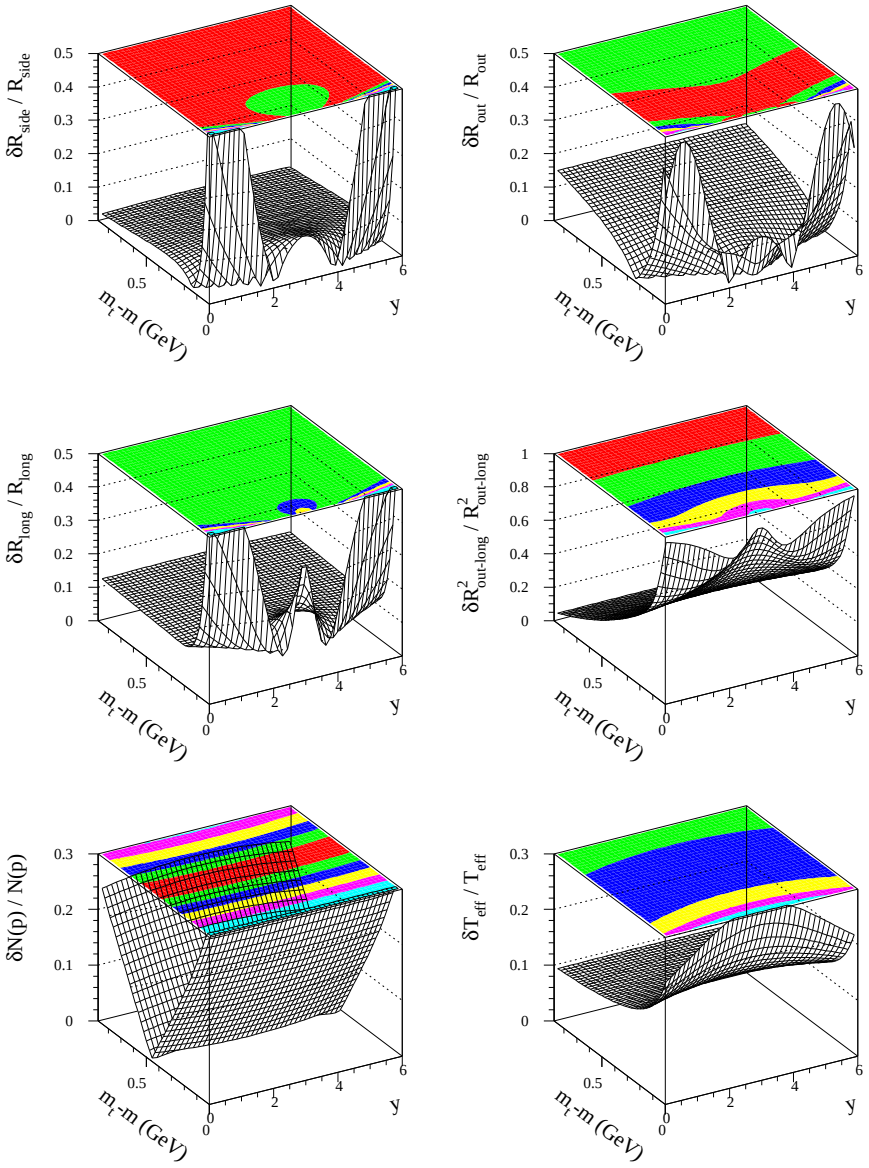

ERROR Source Parameter Set 1

τ_0 = 5.1 fm/c	T_0 = 154 MeV	T_r = 106 MeV	$\Delta\eta$= 1.6
$\Delta\tau$= 0.3 fm/c	m = 140 MeV	T_t = 142 MeV	y_0 = 3
R_g = 5.4 fm	g = 3	u_t = 0.52	

Figure 4.5: Relative deviations between the analytic and the numeric approximations to the HBT parameters and particle spectra for Parameter Set 1.

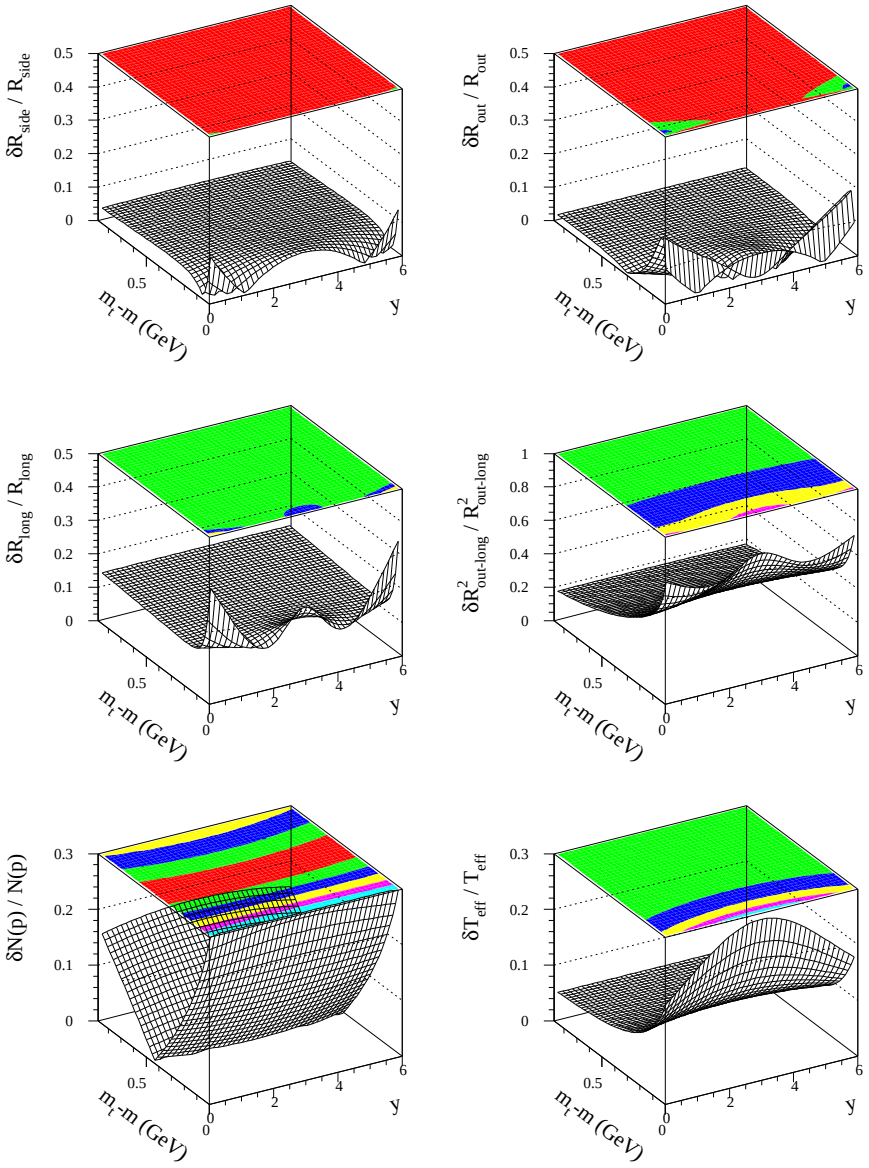

ERROR Source Parameter Set 2

τ_0 = 7 fm/c	T_0 = 108 MeV	T_r = 104 MeV	$\Delta\eta$ = 1.48
$\Delta\tau$ = 2.34 fm/c	m = 140 MeV	T_t = 6 MeV	y_0 = 3
R_g = 4.4 fm	g = 3	u_t = 0.51	

Figure 4.6: Relative deviations between the analytic and the numeric approximations to the HBT parameters and particle spectra for Parameter Set 2.

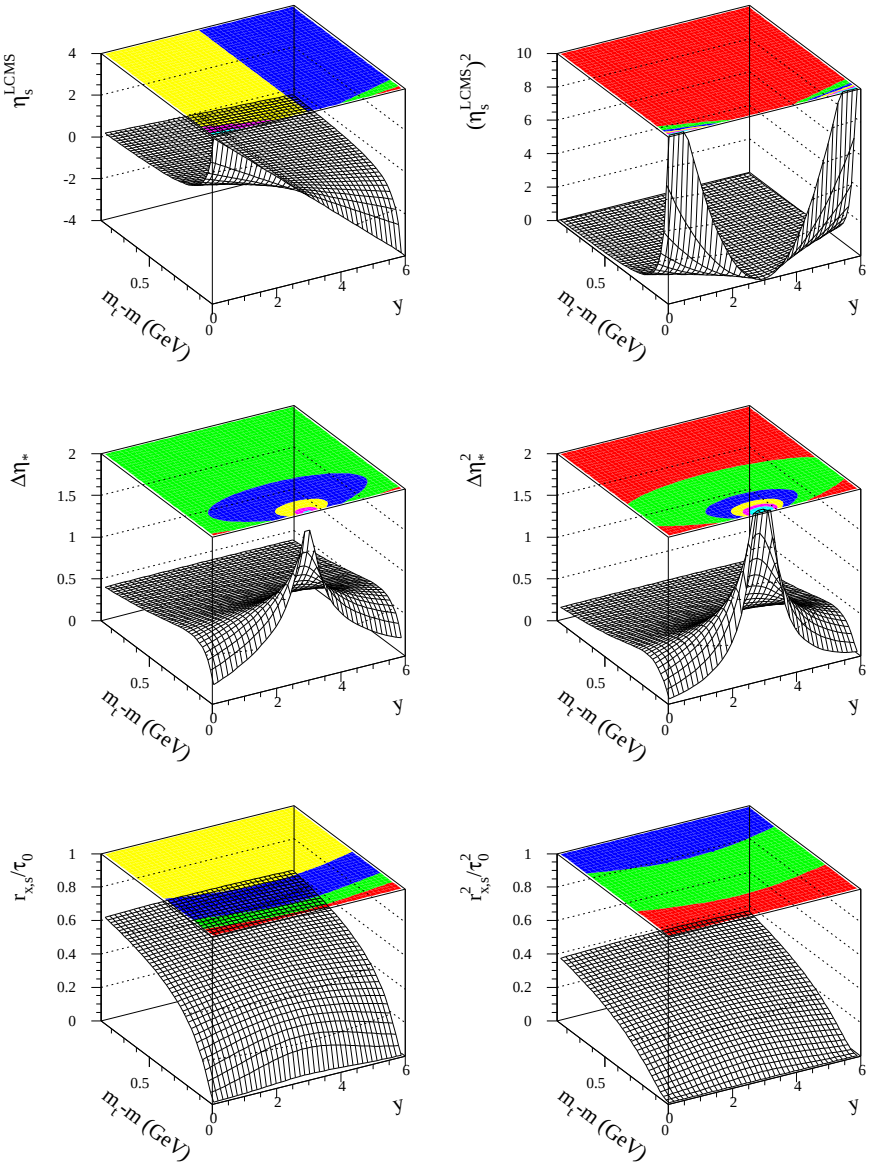

SMALLPAR Source Parameter Set 1

τ_0 = 5.1 fm/c	T_0 = 154 MeV	T_r = 106 MeV	$\Delta\eta$= 1.6
$\Delta\tau$= 0.3 fm/c	m = 140 MeV	T_t = 142 MeV	y_0 = 3
R_g= 5.4 fm	g = 3	u_t = 0.52	

Figure 4.7: Small expansion parameters of the hydrodynamic core model for Parameter Set 1.

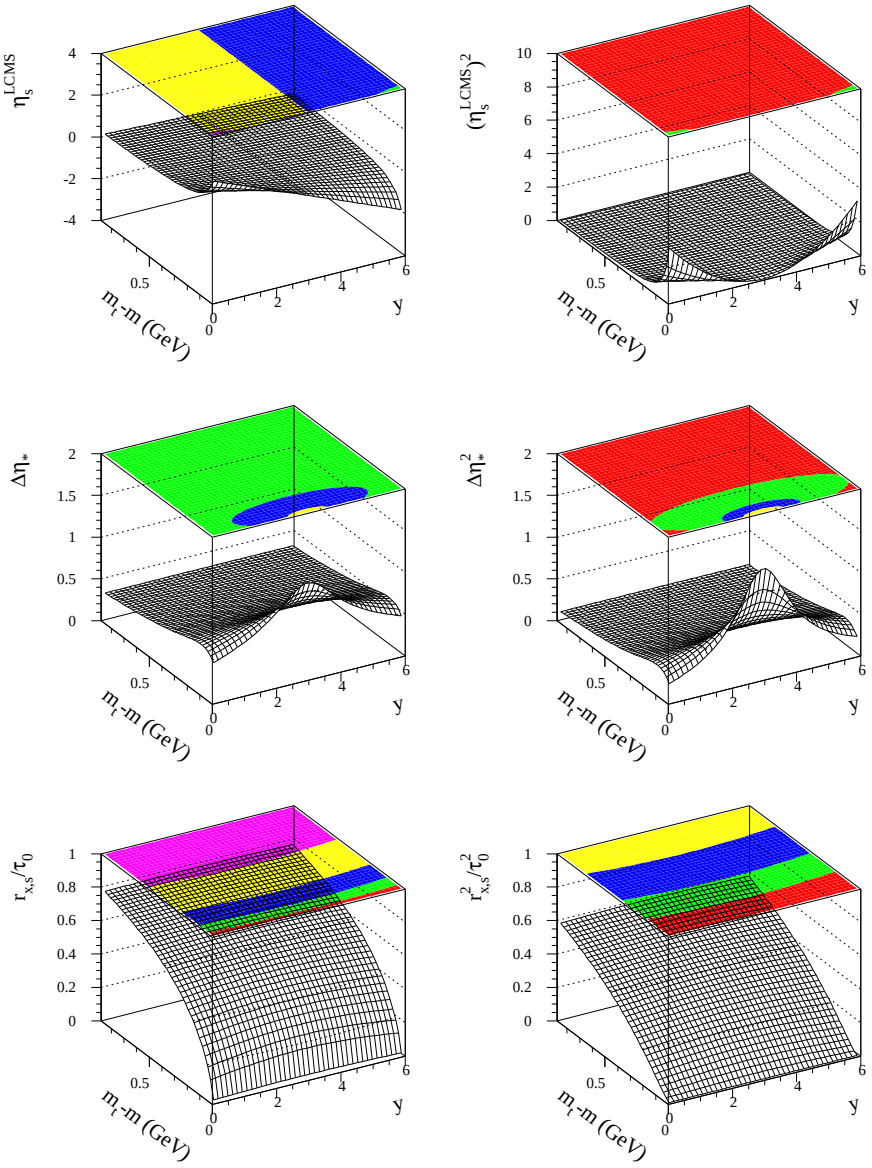

SMALLPAR Source Parameter Set 2

τ_0 =	7	fm/c	T_0 =	108	MeV	T_r = 104 MeV	$\Delta\eta$= 1.48
$\Delta\tau$=	2.34	fm/c	m =	140	MeV	T_t = 6 MeV	y_0 = 3
R_g =	4.4	fm	g =	3		u_t = 0.51	

Figure 4.8: Small expansion parameters of the hydrodynamic core model for Parameter Set 2.

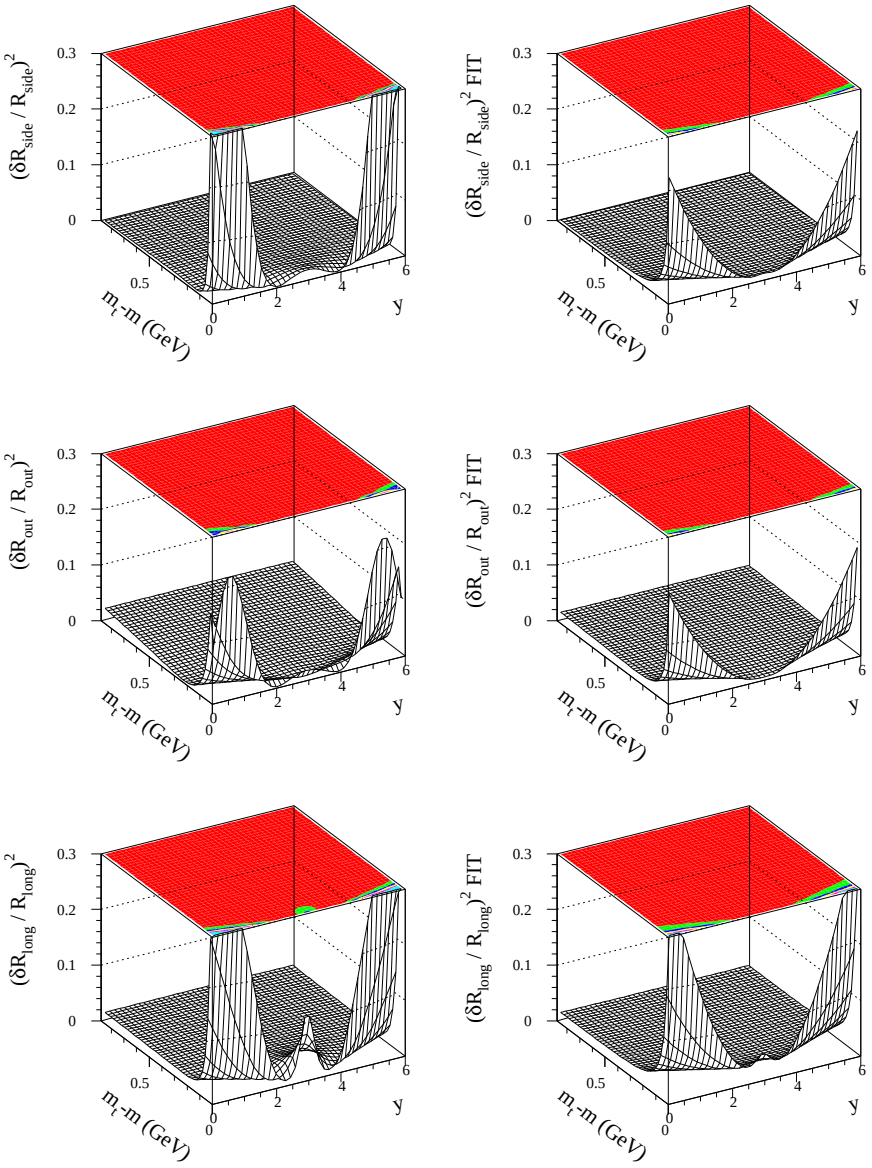

ERROR PARAMETERIZATION for Source Parameter Set 1

$$(\delta R_{side} / R_{side})^2 = 0.015 * (\eta_s^{LCMS})^2 + 0.003 * \Delta\eta_*^2 + 0.002 * r_{x,s}^2/\tau_0^2$$

$$(\delta R_{out} / R_{out})^2 = 0.013 * (\eta_s^{LCMS})^2 + 0.001 * \Delta\eta_*^2 + 0.039 * r_{x,s}^2/\tau_0^2$$

$$(\delta R_{long} / R_{long})^2 = 0.027 * (\eta_s^{LCMS})^2 + 0.014 * \Delta\eta_*^2 + 0.032 * r_{x,s}^2/\tau_0^2$$

Figure 4.9: Parametrization of the relative deviations between the analytic and the numeric approximations to the HBT parameters and particle spectra for Parameter Set 1.

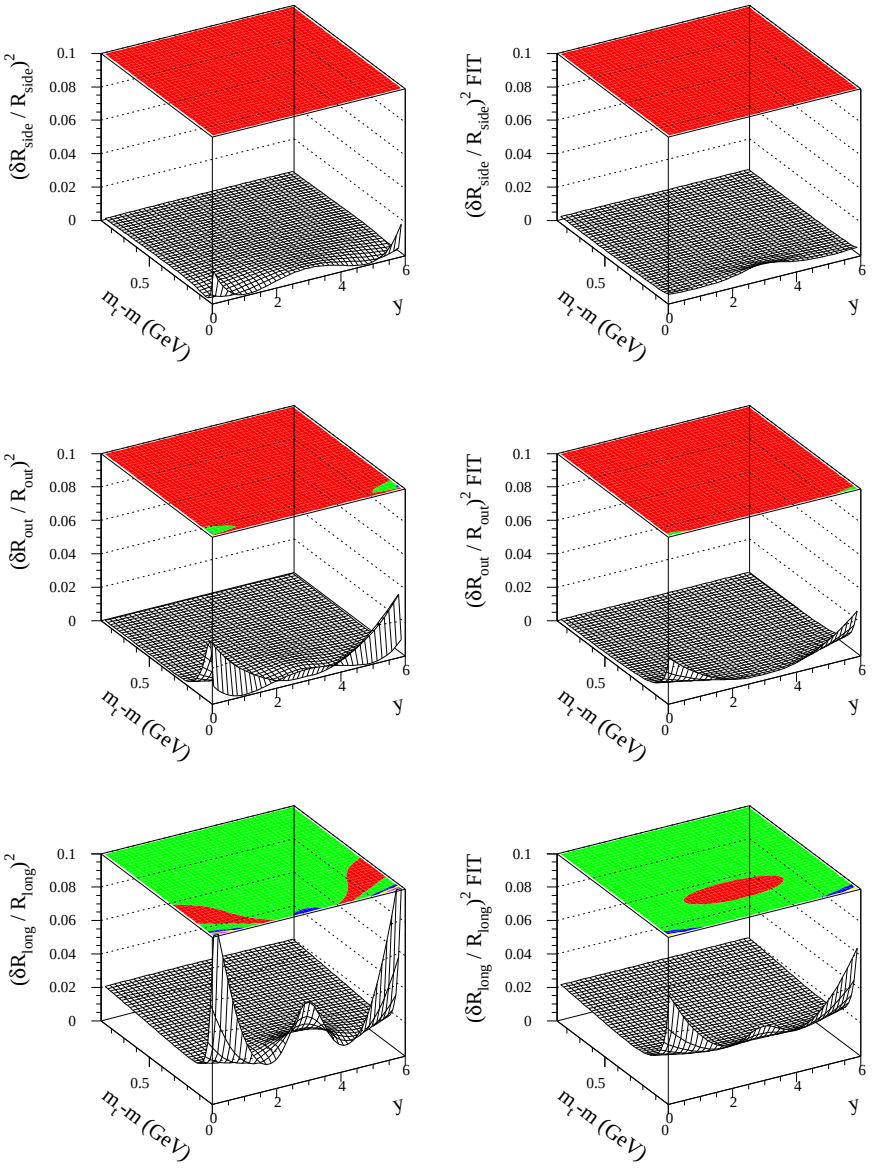

ERROR PARAMETERIZATION for Source Parameter Set 2

$$(\delta R_{side} / R_{side})^2 = 0.001 * (\eta_s^{LCMS})^2 + 0.007 * \Delta\eta_*^2 + 0.003 * r_{x,s}^2/\tau_0^2$$

$$(\delta R_{out} / R_{out})^2 = 0.008 * (\eta_s^{LCMS})^2 + 0.002 * \Delta\eta_*^2 + 0.001 * r_{x,s}^2/\tau_0^2$$

$$(\delta R_{long} / R_{long})^2 = 0.018 * (\eta_s^{LCMS})^2 + 0.024 * \Delta\eta_*^2 + 0.031 * r_{x,s}^2/\tau_0^2$$

Figure 4.10: Parametrization of the relative deviations between the analytic and the numeric approximations to the HBT parameters and particle spectra for Parameter Set 2.

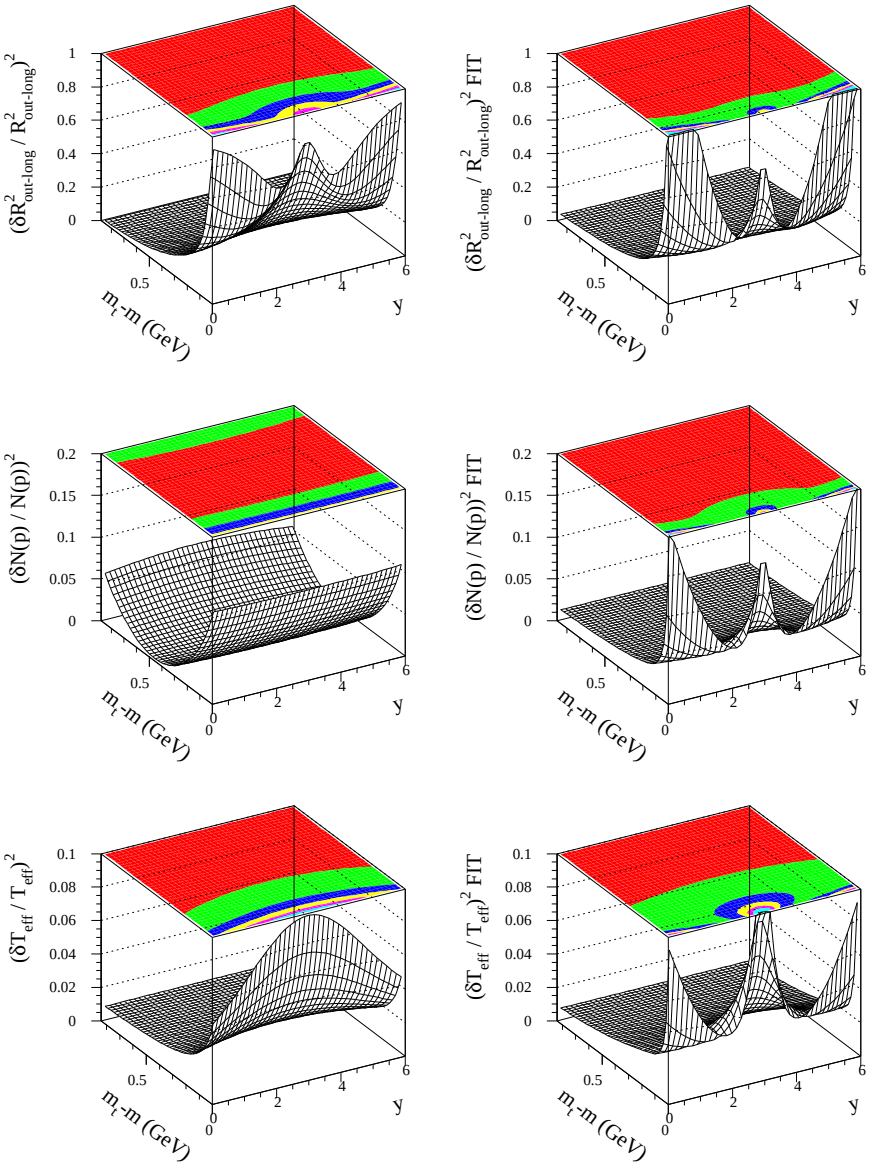

ERROR PARAMETERIZATION for Parameter Set 1

$$(\delta R^2_{outl} / R^2_{outl})^2 = 0.13 * (\eta_s^{LCMS})^2 + 0.208 * \Delta\eta_*^2 + 0.001 * r^2_{x,s}/\tau_0^2$$

$$(\delta N(p) / N(p))^2 = 0.014 * (\eta_s^{LCMS})^2 + 0.044 * \Delta\eta_*^{-2} + 0.015 * r^2_{x,s}/\tau_0^2$$

$$(\delta T_{eff} / T_{eff})^2 = 0.006 * (\eta_s^{LCMS})^2 + 0.042 * \Delta\eta_*^{-2} + 0.001 * r^2_{x,s}/\tau_0^2$$

Figure 4.11: Parametrization of the relative deviations between the analytic and the numeric approximations to the HBT parameters and particle spectra for Parameter Set 1.

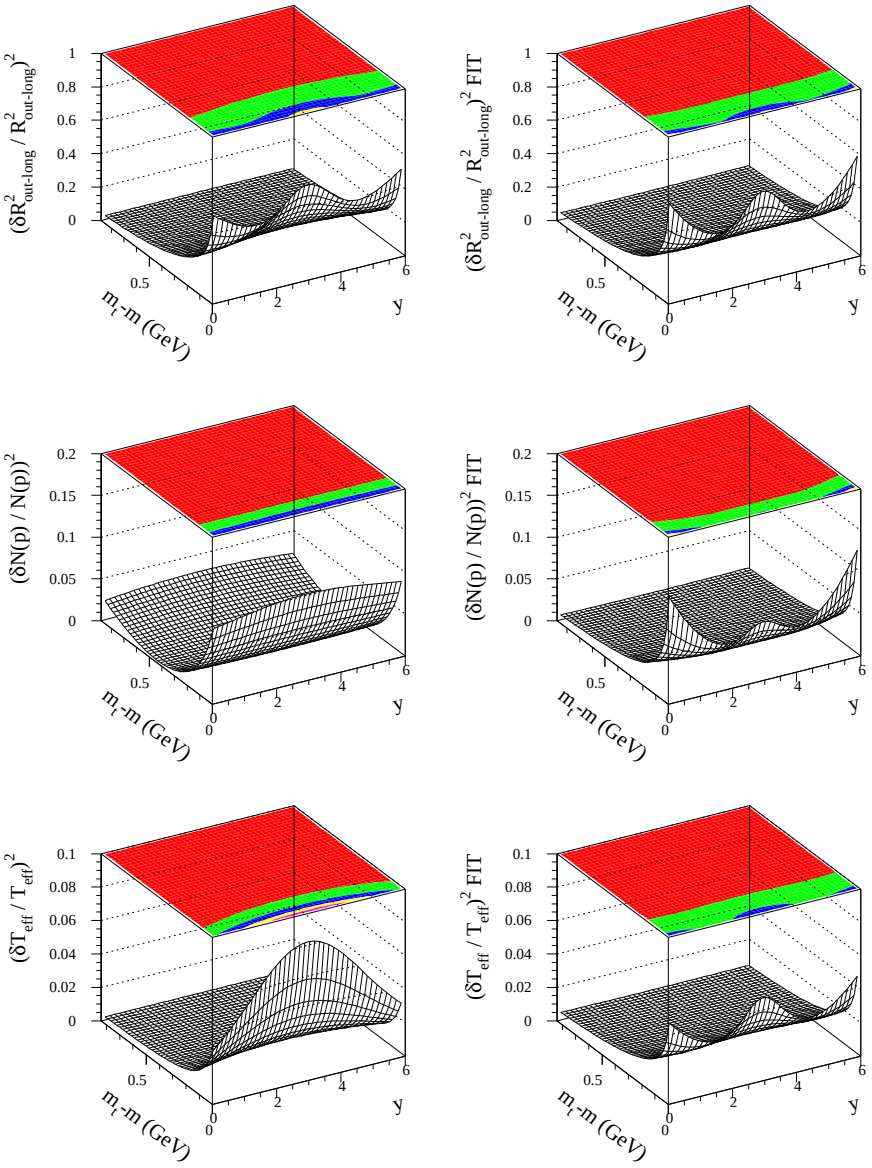

ERROR PARAMETERIZATION for Parameter Set 2

$$(\delta R^2_{outl} / R^2_{outl})^2 = 0.154 * (\eta_s^{LCMS})^2 + 0.398 * \Delta\eta_*^2 + 0.001 * r^2_{x,s}/\tau_0^2$$

$$(\delta N(p) / N(p))^2 = 0.035 * (\eta_s^{LCMS})^2 + 0.052 * \Delta\eta_*^{-2} + 0.001 * r^2_{x,s}/\tau_0^2$$

$$(\delta T_{eff} / T_{eff})^2 = 0.012 * (\eta_s^{LCMS})^2 + 0.037 * \Delta\eta_*^{-2} + 0.001 * r^2_{x,s}/\tau_0^2$$

Figure 4.12: Parametrization of the relative deviations between the analytic and the numeric approximations to the HBT parameters and particle spectra for Parameter Set 2.

Chapter 5

Application to CERN SPS energies

5.1 Introduction

In this chapter it is shown that the final state of $Pb+Pb$ reactions at CERN SPS can be reconstructed with the Buda-Lund hydro model, by performing a simultaneous fit to NA49, NA44 and WA98 data on particle correlations and spectra. This chapter is based on my work of Ref. [Ste99b]

In refs. [Csö95a, Csö95b] it was observed, for the first time, that the parameters of particle emitting sources can be determined only if *a simultaneous analysis of the momentum distributions and two-particle correlation functions* is performed. Simultaneous fitting of particle correlations and spectra were reported in refs. [Csö95b, Csö96b, Ste99, Cha98, Aga97, App98]. Here, we determine the reconstructed space-time picture of particle emission in Pb + Pb collisions at CERN SPS by fitting simultaneously the NA44 and NA49 published data [App99, Bea97] on two-particle correlations and single-particle spectra at Pb + Pb 158 AGeV central reactions at CERN SPS. Preliminary data [Ros98] from WA98 experiment are also used to check the reliability and the consistency of the fit results.

5.2 Buda-Lund hydrodynamic model

The Buda-Lund hydro parameterization characterizes with means and variances the local temperature, flow and chemical potential distributions of a cylindrically symmetric, finite hydrodynamically expanding system. The four-velocity $u^\mu(x)$ of the expanding matter is given by a scaling longitudinal Bjorken flow appended with a linear transverse flow, characterized by its mean value, $\langle u_t \rangle$. A Gaussian shape of the local density distribution is assumed both in the transverse plane and in space-time rapidity. The changes of the inverse temperature are characterized with means and variances. The freeze-out hypersurface is characterized by a mean freeze-out (proper)time τ_0 and a duration parameter $\Delta\tau$, the variance of the freeze-out propertime distribution. The model was reviewed in Chapter 4.

5.3 Fitting NA49, NA44 and WA98 Pb + Pb data

The kinematic parameters of the Buda-Lund model are fitted simultaneously to IMD and HBT radii measured by the CERN NA49, NA44 and WA98 experiments in central $Pb+Pb$ collisions at 158 AGeV. Core/halo correction $\propto 1/\sqrt{\lambda_*}$ is applied and the corresponding errors are propagated properly. Due to the these conditions unique minima are found, a good χ^2/NDF is obtained for all reactions, and the strongly coupled, normalization sensitive $\langle \frac{\Delta T}{T} \rangle_t$ and $\Delta\tau$ parameters are determined. On Figs. 5.1 and 5.2, the fits to measured data are shown together with the published data. Note that the first 5 points of the NA44 pion spectrum were contaminated [Bea97] and were not included in the fit.

Fits to preliminary data of WA98 experiment provide source parameter values and errors similar to those obtained by NA49 and NA44. The normalizations of the NA44 pion spectrum and the WA98 h^-spectrum had to be fixed manually to that of NA49.

The hypothesis that pions, kaons and protons are emitted from the same

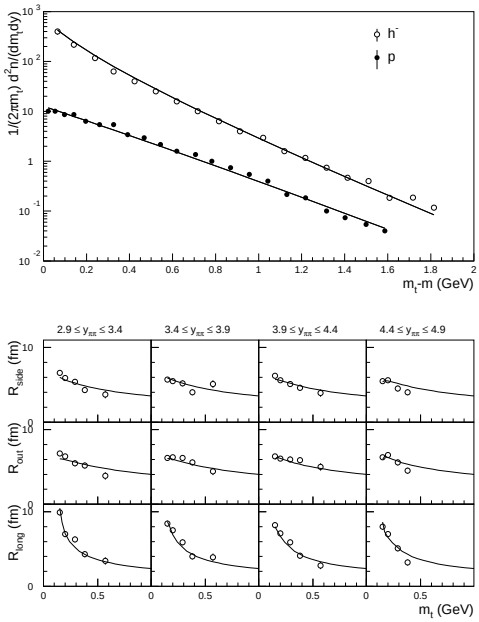

Figure 5.1: Simultaneous fits to NA49 particle spectra and HBT radius parameters.

hydrodynamical source is in a good agreement with all the fitted data. The fit parameters are summarized in Table 1, shown with statistical errors, only. The reconsructed space-time emission function $S(x)$ (which is the source function $S(x,p)$ integrated over the momentum p) is shown on Figure 3 and 4.

5.4 Summary of fit parameters

We find that the NA49, NA44 and WA98 data on single particle spectra of h^-, identified π, K and p as well as detailed rapidity and m_t dependent HBT radius parameters are consistent with each other. The final state of central Pb + Pb collisions at CERN SPS corresponds to a cylindrically symmetric, large ($R_G = 7.1 \pm 0.2$ fm) and homogenous ($T_0 = 139 \pm 6$ MeV) fireball,

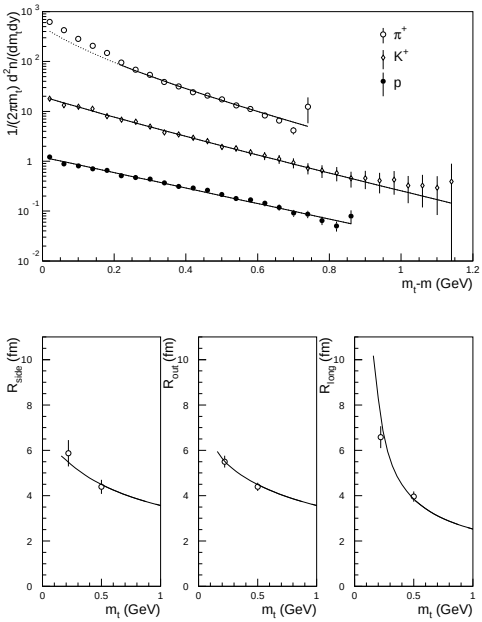

Figure 5.2: Simultaneous fits to NA44 particle spectra and HBT radius parameters.

expanding three-dimensionally with $\langle u_t \rangle = 0.55 \pm 0.06$. A large mean freeze-out time, $\tau_0 = 5.9 \pm 0.6$ is found with a short duration of emission.

Table 5.1: Source parameters from simultaneous fitting of NA49, NA44 and preliminary WA98 particle spectra and HBT radius parameters with the Buda-Lund hydrodynamical model. These characterize the hadronic freeze-out. The time dependence of these source parameters depends on the EoS.

	NA49		NA44		WA98		Averaged	
Parameter	Value	Error	Value	Error	Value	Error	Value	Error
T_0 [MeV]	134	$\pm$ 3	145	$\pm$ 3	139	$\pm$ 5	139	$\pm$ 6
$\langle u_t \rangle$	0.61	$\pm$ 0.05	0.57	$\pm$ 0.12	0.50	$\pm$ 0.09	0.55	$\pm$ 0.06
R_G [fm]	7.3	$\pm$ 0.3	6.9	$\pm$ 1.1	6.9	$\pm$ 0.4	7.1	$\pm$ 0.2
τ_0 [fm/c]	6.1	$\pm$ 0.2	6.1	$\pm$ 0.9	5.2	$\pm$ 0.3	5.9	$\pm$ 0.6
$\Delta\tau$ [fm/c]	2.8	$\pm$ 0.4	0.01	$\pm$ 2.2	2.0	$\pm$ 1.9	1.6	$\pm$ 1.5
$\Delta\eta$	2.1	$\pm$ 0.2	2.4	$\pm$ 1.6	1.7	$\pm$ 0.1	2.1	$\pm$ 0.4
$\langle \frac{\Delta T}{T} \rangle_r$	0.07	$\pm$ 0.02	0.08	$\pm$ 0.08	0.01	$\pm$ 0.02	0.06	$\pm$ 0.05
$\langle \frac{\Delta T}{T} \rangle_t$	0.16	$\pm$ 0.05	0.87	$\pm$ 0.72	0.74	$\pm$ 0.08	0.59	$\pm$ 0.38
χ^2/NDF	163/98 = 1.66		63/71 = 0.89		115/108 = 1.06		1.20	

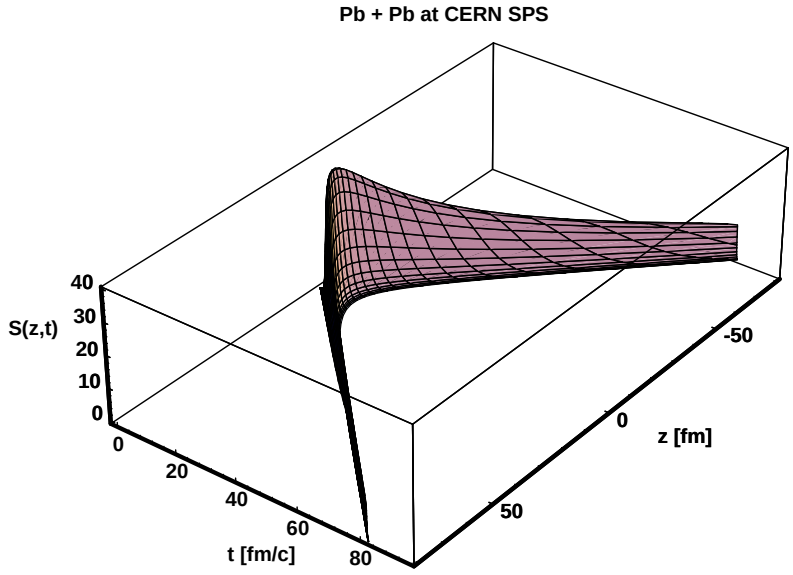

Figure 5.3: The reconstructed source function $S(t, z, x = 0, y = 0)$ in the (t, z) plane.

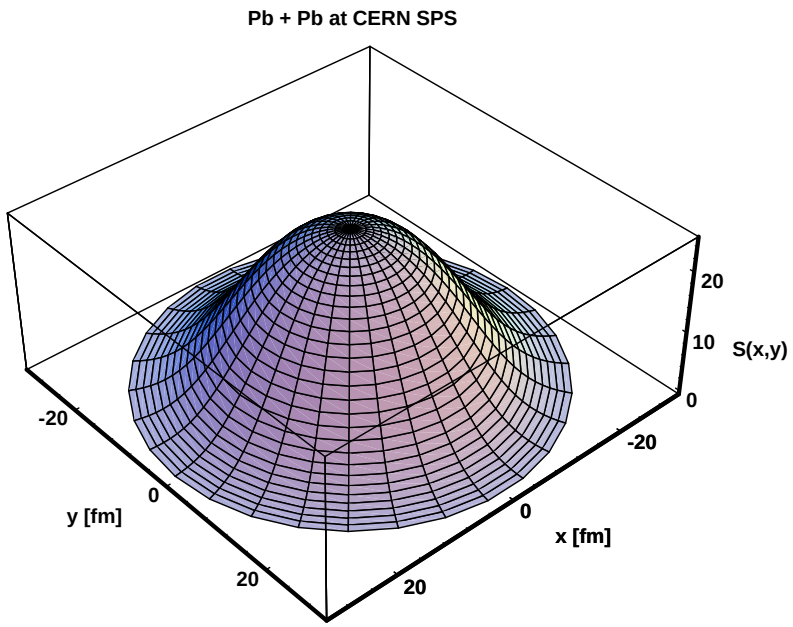

Figure 5.4: The reconstructed source function $S(x, y)$ at the mean freeze-out time.

Chapter 6

Application to RHIC energies

6.1 Introduction

In this chapter, the Buda-Lund hydro model fits are compared to BRAHMS, PHENIX, PHOBOS and STAR data on identified particle spectra, two-particle Bose-Einstein or HBT correlations, charged particle pseudorapidity distributions and pseudorapidity as well as p_t dependent elliptic flow in $\sqrt{s_{\rm NN}} = 130$ and 200 GeV Au+Au collisions at RHIC. Preliminary results indicate that 7/8-th of the particle emitting volume is rather cold, with surface temperature of 105 MeV, but the temperature has a distribution and the most central 1/8-th of the volume is superheated to $T(x) > T_c = 172 \pm 3$ MeV [Fod02, Fod04].

The Buda-Lund hydro model [Csö95a] is successful in describing the BRAHMS, PHENIX, PHOBOS and STAR data on identified single particle spectra and the transverse mass dependent Bose-Einstein or HBT radii as well as the pseudorapidity distribution of charged particles in Au + Au collisions both at $\sqrt{s_{\rm NN}} = 130$ GeV [Csa04a] and at $\sqrt{s_{\rm NN}} = 200$ GeV [Csa04c]. Recently, Fodor and Katz calculated the phase diagram of lattice QCD at finite net baryon density [Fod02]. Their results, obtained with light quark masses four times heavier than the physical value, indicated that in the $0 \leq \mu_B \leq 300$ MeV region the transition from confined to deconfined matter is not a first or second order phase-transition, but a cross-over with a nearly

constant critical temperature, $T_c = 172 \pm 3$ MeV. The result of the Buda-Lund fits to Au+Au data, both at $\sqrt{s_{\rm NN}} = 130$ and 200 GeV, indicate the existence of a very hot region. The temperature distribution $T(x)$ of this region is characterized with a central temperature T_0, found to be greater than the critical value calculated from lattice QCD: $T_0 > T_c$ [Csa03b]. The Buda-Lund fits thus indicate quark deconfinement in Au + Au collisions at RHIC. The observation of a superheated center in Au+Au collisions at RHIC is confirmed by the analysis of p_t and η dependence of the elliptic flow [Csa03b], measured by the PHENIX [Adl03a] and PHOBOS collaborations [Bac02, Man02]. A similar analysis of Pb+Pb collisions at CERN SPS energies yields central temperatures lower than the critical value, $T_0 < T_c$ [Ste99, Csö02].

Here we summarize the Buda-Lund fit results as detailed in refs. [Csa04a, Csa04c, Csa03b, Ste99]. See these papers for definitions and discussion of the results as well as more detailed references.

6.2 Buda-Lund fit results to central Au+Au data at $\sqrt{s_{\rm NN}} = 130$ and 200 GeV

Analyzing the fit parameters (Table 1) we find that $T_0 > T_c$ by more than 5σ in case of the $0 - 5(6)\%$ most central Au+Au data at $\sqrt{s_{NN}} = 130$ GeV. We interpret this as an indication of quark deconfinement. In case of the less central $(0 - 30\%)$ Au+Au data at $\sqrt{s_{NN}} = 200$ GeV, with an improved analysis we find $T_0 > T_c$ by 2σ, not a significant difference. We interpret this as a possible hint for quark deconfinement. In both cases, the flow profile within errors coincides with the three-dimensional Hubble flow, $u^\mu = x^\mu/\tau$. For details, see refs. [Csö02, Csö04]. For similar results, see refs. [Ret03, Bro01, Bro02].

6.3 Buda-Lund results for the elliptic flow in Au+Au data at RHIC

The model is evaluated in all panels with the following parameters: $T_0 = 210$ MeV, $T_s = 105$ MeV, $X_f = 8.6$ fm, $Y_f = 10.5$ fm, $Z_f = 17.5$ fm, $\dot{X}_f = 0.57$, $\dot{Y}_f = 0.45$, $\dot{Z}_f = 2.4$, $\tau_0 = 7$ fm/c, $\vartheta = 0.09$, $\mu_{0,\pi} = 70$ MeV, $\mu_{0,K} = 210$ MeV and $\mu_{0,p} = 315$ MeV. T_0 is the temperature of the center, while T_s is that of the surface, (X_f, Y_f, Z_f) are the principal axes and $(\dot{X}_f, \dot{Y}_f, \dot{Z}_f)$ the principal expansion rates of the ellipsoid at the freeze-out proper-time τ_0. For more details, see pages 3-6 of ref. [Csa03b].

Table 1, Figures 1 and 2 indicate that the Buda-Lund hydro model works well at both RHIC energies: it gives a good quality description of the transverse mass dependence of the HBT radii as well as identified particle spectra and elliptic flow, see refs. [Csö95a, Csö02b, Csö02c, Csö03] for further details.

The temperature was estimated to be above T_c in the most central 1/8th of the expanding ellipsoid [Csa03b], similarly to a fireball that is heated from inside. We interpret this result as a confirmation of the quark deconfinement and the cross-over like transition found in Buda-Lund fits to central Au+Au collisions at $\sqrt{s_{\rm NN}} = 130$ and 200 GeV.

Buda-Lund parameter	Au+Au 130 GeV	Au+Au 200 GeV
T_0 [MeV]	214 $\pm$ 7	196 $\pm$ 13
$T_{\rm e}$ [MeV]	102 $\pm$ 11	117 $\pm$ 12
μ_B [MeV]	77 $\pm$ 38	61 $\pm$ 52
R_G [fm]	28.0 $\pm$ 5.5	13.5 $\pm$ 1.7
R_s [fm]	8.6 $\pm$ 0.4	12.4 $\pm$ 1.6
$\langle u_t' \rangle$	1.0 $\pm$ 0.1	1.6 $\pm$ 0.2
τ_0 [fm/c]	6.0 $\pm$ 0.2	5.8 $\pm$ 0.3
$\Delta\tau$ [fm/c]	0.3 $\pm$ 1.2	0.9 $\pm$ 1.2
$\Delta\eta$	2.4 $\pm$ 0.1	3.1 $\pm$ 0.1
χ^2/NDF	158.2 / 180	114 / 208

Table 6.1: Buda-Lund hydro model v1.5 source parameters, corresponding to Figs. 1 and 2. The errors on the parameters are preliminary, as point-to-point and normalization errors are added in quadrature when evaluating χ^2.

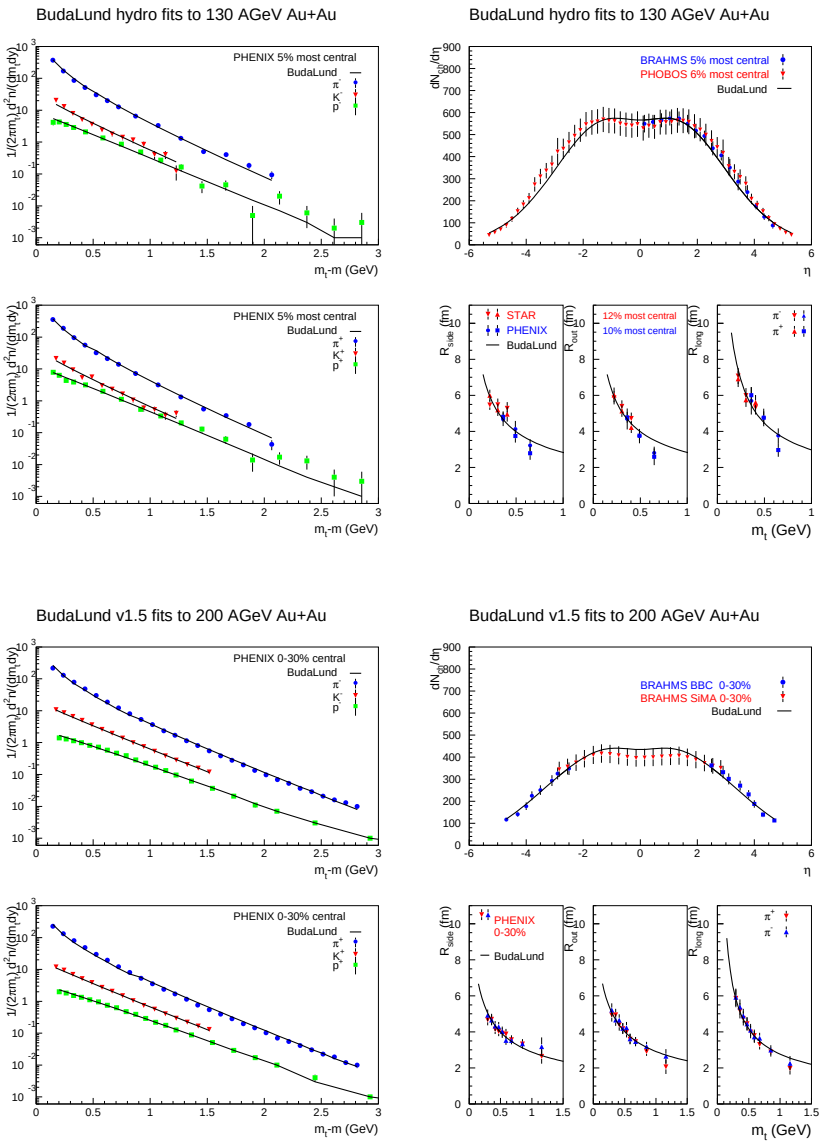

Figure 6.1: The upper four panels show a simultaneous Buda-Lund fit to 0-5(6) % central Au+Au data at $\sqrt{s_{NN}} = 130$ GeV, refs. [Bea01, Adc01a, Adc02a, Bac01, Adl01a]. The lower four panels show similar fits to 0-30 % central Au+Au data at $\sqrt{s_{\rm NN}} = 200$ GeV, refs. [Bea02, Adl03b, Adl04a]. The fit parameters are summarized in Table 1.

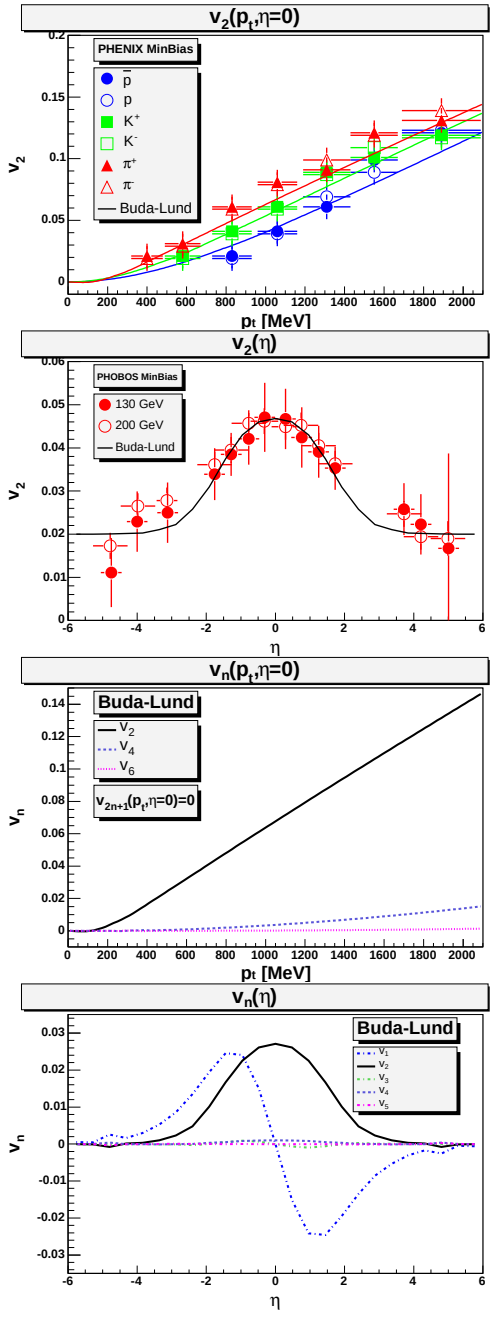

Figure 6.2: In the top panels, the ellipsoidally symmetric Buda-Lund hydro calculations are compared to PHENIX identified $v_2(p_t)$ data at 200 GeV [Adl03a] and PHOBOS $v_2(\eta)$ data at 130 and 200 GeV [Bac02, Man02]. On the top right panel, we added a constant non-flow parameter of 0.02 to the calculated values of v_2. In the lower panels, the flow coefficients, v_n-s are shown for $n = 1 \ldots 6$ as a function of transverse momentum at midrapidity, as well as a function of pseudorapidity, with integrated p_t. Note, that more precise v_2 fits are reported elsewhere in Ref. [Csa05]

6.4 RHIC vs CERN SPS results - a comparision using the Buda-Lund model

6.4.1 Introduction

In this section the space-time evolution of colliding systems are compared at energies of SPS and RHIC experiments. Previously, the Buda-Lund hydrodynamical model was able to reconstruct the final states of h+p, A+A reactions. Now, we use these hydro results, together with preliminary ones obtained from RHIC p+p collisions, to calculate the particle emission functions. Their shapes and the parameters characterizing the source of emission are shown and discussed in detail. The comparison gives that at RHIC energies we are above the critical temperature ($T_c = 172 \pm 3\ MeV$) of deconfinement. Moreover, we can see fairly different types of emission dynamics in case of hadron-hadron and heavy ion reactions.

In this section we compare the the different reactions via the particle emission probabilities for which we use the Buda-Lund hydrodinamical model parameters extracted from the final data of the above experiments. In this analyses we have included our earlier hydro results we obtained fitting data of CERN SPS experiments of Pb+Pb and h+p collisions, as well [Aga97, Ste99b]. Our preliminary hydro results on p + p collisions at $\sqrt{s_{\rm NN}} = 200$ GeV of PHENIX and STAR were also used, as an addition. However, we have made the first attempt to fit d+Au data, as well, this time those results are not part of the study because such sort of collisions represent an asymmetric case. Currently, the model describes axially or ellipsoidally symmetric cases.

6.4.2 Emission function in the Buda-Lund hydro model

The Buda-Lund hydro model was introduced in refs. [Csö95a, Csö95b]. This model was defined in terms of its emission function $S(x, k)$, for axial symmetry, corresponding to central collisions of symmetric nuclei. The observables are calculated analytically, see refs. [Csa04a, Csö02] for details and key features.

Note, that different combinations (as new fit parameters) may also be used to measure the flow, temperature and fugacity profiles [Csö95a, Csö02]: $H_t \equiv b/\tau_0 \; = \; \langle u_t \rangle / R_G \; = \; \langle u'_t \rangle / R_s$, $H_l \equiv \gamma_t / \tau_0$, where $\gamma_t = \sqrt{1 + H_t^2 r_t^2}$ is evaluated at the point of maximal emittivity, and

$$\frac{1}{R_s^2} \;=\; \frac{a^2}{\tau_0^2} \;=\; \langle \frac{\Delta T}{T} \rangle_r \frac{1}{R_G^2} \;=\; \frac{T_0 - T_s}{T_s} \frac{1}{R_G^2}, \tag{6.1}$$

$$\frac{1}{\Delta\tau_s^2} \;=\; \frac{d^2}{\tau_0^2} \;=\; \langle \frac{\Delta T}{T} \rangle_s \frac{1}{\Delta\tau^2} \;=\; \frac{T_0 - T_e}{T_e} \frac{1}{\Delta\tau^2}. \tag{6.2}$$

6.4.3 Emission functions of SPS and RHIC collisions

In this analyses this emission functions are calculated for CERN SPS Pb+Pb and h+p collisions, along with RHIC experiments BRAHMS, PHENIX, PHOBOS and STAR. All SPS and RHIC datapoints were fitted simultaneously, using the analytic expressions and the CERN Minuit fitting package. The fitting package used in this analysis is version 1.5, made public at [Csö04]. Table 6.2 shows the collected source parameters obtained from Buda-Lund hydrodynamical analysis of the data quoted. Where it was applicable, some old source parameters of SPS data have been transformed to new ones, like R_s where the temperature drops to half and the evaporation temperature (T_e). The emission probabilities $S(x, y)$ and $S(z, t)$ shown in Figs. 6.3, 6.4, 6.5, 6.6, 6.7 were calculated by equations defined in the previuos section using the the source parameters collected in Table 6.2.

The figures give comprehensive quantitative and qualitative picture about the nature of the nuclear processes in question. In general, small size systems can be characterized by ring of fire type particle emission, while in heavy ion collisions fireball like evolution takes place. The two types of behaviour is a result of two competing processes: whether the collective motion (flow) of particles is fast enough to overcome the pressure caused by the temperature gradient. Consult the corresponding radii and temperature components in the table of source parameters and the figures to recognize such relations.

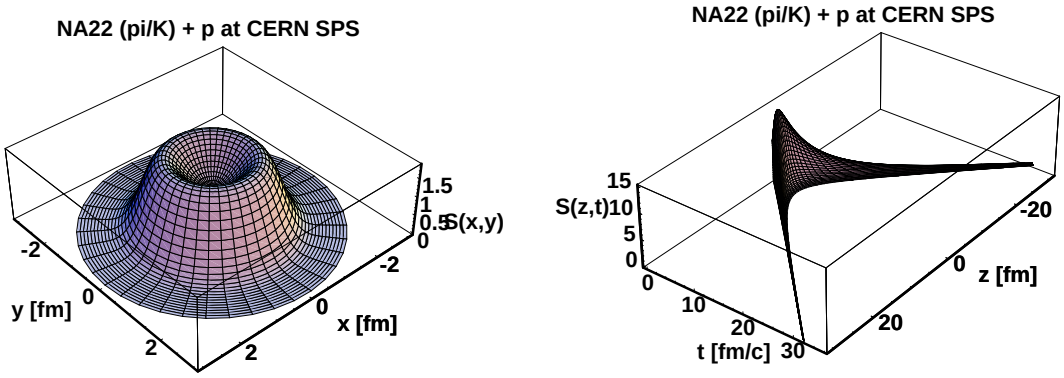

Figure 6.3: The emission function of h+p reactions at SPS. The left panel shows the value of S in plane (x,y), while the right one shows it in plane (t,z). The strong temperature gradient drives out particles in waves from the center of the emission.

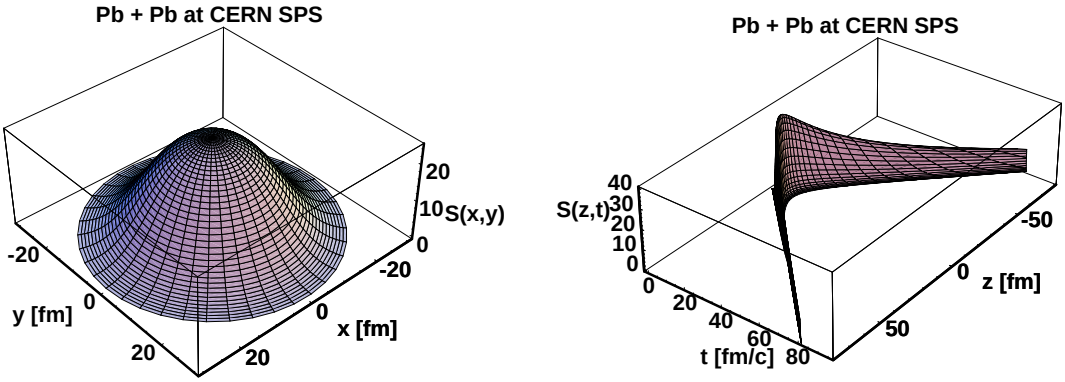

Figure 6.4: The emission function of Pb+Pb reactions at SPS. The left panel shows the value of S in plane (x,y), while the right one shows it in plane (t,z). The temperature gradient competes with the the strengh of the particle flow which results in fireball type of emission.

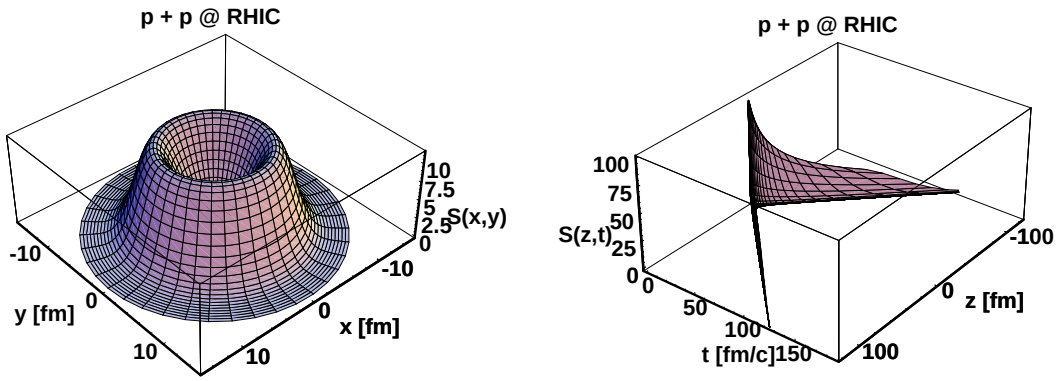

Figure 6.5: The emission function of p+p reactions at RHIC. The left panel shows the value of S in plane (x,y), while the right one shows it in plane (t,z). The very strong temperature gradient drives out particles from the emission center.

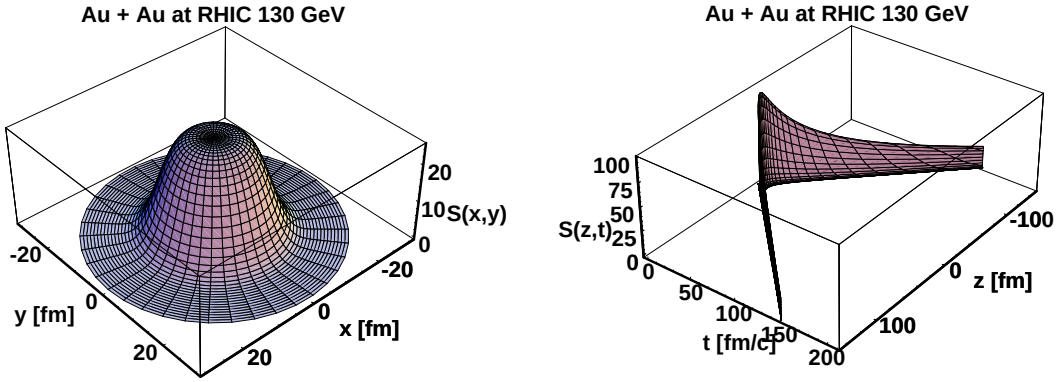

Figure 6.6: The emission function of Au+Au 130 GeV reactions at SPS. The left panel shows the value of S in plane (x,y), while the right one shows it in plane (t,z). The temperature gradient competes with the strengh of the particle flow which results in fireball type of emission.

Buda-Lund parameter	SPS h+p	SPS Pb+Pb	RHIC p+p 200 GeV	RHIC Au+Au 130 GeV	RHIC Au+Au 200 GeV
T_0 [MeV]	140 ± 3	139 ± 6	289 ± 8	214 ± 7	196 ± 13
$T_{\rm e}$ [MeV]	-	87 ± 24	90 ± 42	102 ± 11	117 ± 12
μ_B [MeV]	0 fixed	0 fixed	8 ± 76	77 ± 38	61 ± 52
R_G [fm]	0.88 ± 0.13	7.1 ± 0.2	1.2 ± 0.3	28.0 ± 5.5	13.5 ± 1.7
R_s [fm]	1.4 ± 0.3	28 ± 21	1.13 ± 0.16	8.6 ± 0.4	12.4 ± 1.6
$\langle u_t' \rangle$	0.2 ± 0.07	0.55 ± 0.06	0.04 ± 0.26	1.0 ± 0.1	1.6 ± 0.2
τ_0 [fm/c]	1.4 ± 0.1	5.9 ± 0.6	1.1 ± 0.2	6.0 ± 0.2	5.8 ± 0.3
$\Delta\tau$ [fm/c]	1.3 ± 0.3	1.6 ± 1.5	0.1 ± 0.5	0.3 ± 1.2	0.9 ± 1.2
$\Delta\eta$	1.36 ± 0.02	2.1 ± 0.4	3.0 fixed	2.4 ± 0.1	3.1 ± 0.1
χ^2/NDF	642 / 683	342 / 277	89 / 71	158 / 180	114 / 208

Table 6.2: Buda-Lund hydro model v1.5 source parameters, corresponding to fits to BRAHMS, PHENIX, PHOBOS and STAR data for Au+Au collisions at $\sqrt{s_{NN}}$ = 130 GeV and $\sqrt{s_{NN}}$ = 200 GeV shown in ref. [Csa04a], as well as, to preliminary PHENIX and STAR single particle spectra and HBT radii data for p+p collisions at $\sqrt{s_{NN}}$ = 200 GeV. Pb+Pb data were fitted in ref. [Ste99b], while h+p data at CERN SPS in ref. [Aga97]. In the latter case the parameters that were not calculated at the time of publication are left out or transformed to the new ones.

6.4.4 Summmary of comparisions

It was shown that the Buda-Lund hydrodynamical model describes single particle distributions, rapidity distributions, HBT correlation function radii without puzzle in experiments of h+p and Pb+Pb at SPS, p+p and Au+Au at RHIC.

We have calculated the emission functions of the reactions that show rings of fire in case of h+p at SPS and p+p at RHIC, whereas, for Pb+Pb at SPS and Au+Au at RHIC their space-time dependence show fireballs.

The quantitative comparison of the parameters of the emission sources extracted by Buda-Lund hydrodynamical model calculations has revealed that the freeze-out temperature in the center of the reaction zone is lower then the critical temperature of deconfinement of quarks ($T < T_c$ = 172 ± 3 MeV) both in h+p and in Pb+Pb reactions at SPS. But, it is always higher then that ($T > T_c$) by more or about 3 standard deviations at RHIC,

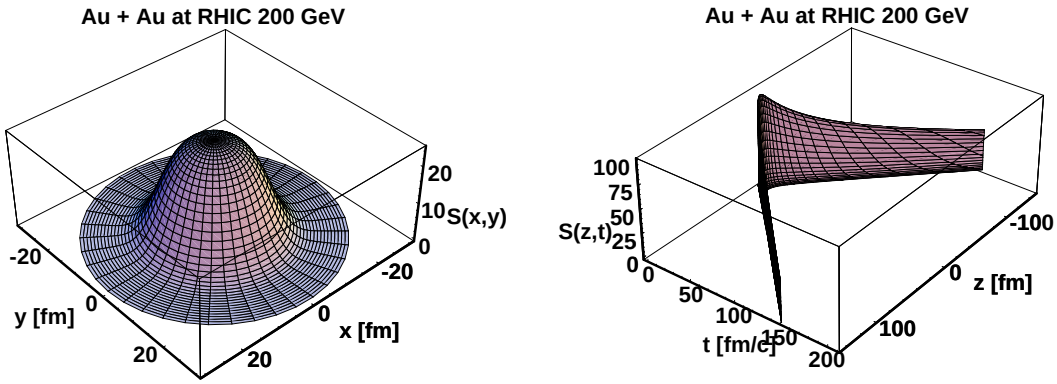

Figure 6.7: The emission function of Au+Au 200 GeV reactions at SPS. The left panel shows the value of S in plane (x,y), while the right one shows it in plane (t,z). The temperature gradient competes with the strengh of the particle flow which results in fireball type of emission.

both in p+p and in Au+Au collisions.

Chapter 7

Summary of theses

1. I have performed GEANT detector simulations of the Zero Degree Calorimeter (ZDC) for the RHIC PHENIX Au+Au experiments. I have created a coalescence model based on data of NA49 for the description of the distribution of the spectator fragments (p, n, d, He, ...) that do not participate in the collisions [Ste00] in order to estimate the ZDS signal in the simulations. I have shown by the simulations that the reactions produce large volume of forward going particle showers whose large fraction produce background noise in the ZDC. I have calculated the magnitude of the effect, for which I have found that in most of the cases it does not exceed 2% of the expected ZDC signal. I have shown that such an effect does not cause relevant errors ($<$ 1%) in determination of the centrality classes. I have given a procedure for the possible corrections. I have participated in defining the centrality classes [Adc00]. I have determined the standar deviation of the energies deposited in the ZDC during the data taking period (RUN). I have used this value for studying the ZDC time stability. I have shown that the equipment was stable during the data taking periods. Selecting Au+Au collisions by centrality classes, we have published numerous articles in journals with highest impact factors [Adc00, Adc01a, Adc01b, Adc02b, Adl03c]

2. I have performed the GEANT detector simulations of the Zero Degree Calorimeter (ZDC) for the RHIC PHENIX Cu+Cu experiments. My calcu-

lations have shown that there are differencies between the ZDC signals in the Au+Au and the Cu+Cu reactions, i.e. the standard deviations of the energies deposited in the ZDC depend on the reaction type. I have shown that it may be necessary to apply the GEANT corrections to the detector data which was not necessary in case of Au+Au collisions. The first results of PHENIX from Cu+Cu collisions were published in [Ada06]

3. I have reconstructed the final state of the CERN SPS Pb+Pb $\sqrt{s_{NN}}$ = 17.3 GeV reactions using the Buda-Lund hydrodynamical model. I have given, on the scale of 10^{-15} m és 10^{-23} sec, how the flow profile looks like when the hadrons are created, i.e. what the distributions of $u^{\mu}(x), T(x)$ and $\mu(x)$ are like, and what the distribution of $H(\tau)$ that describes the creation time of the hadrons is like. I have performed the analysis in such a way that I have simulatneously fitted the distributions predicted by the model to data of particle correlations and spectra of the NA44, NA49 and WA93 experiments. I have found that the analyses of the data of the three different measurements provide results that are consistent with each-other. The averaged figures show that the final state of central Pb+Pb collisions at the CERN SPS corresponds to axially symmetric, large ($R = 7.1 \pm 0.2$ fm) and nearly homogen ($T = 139 \pm 6$ MeV) fireball that rapidly expands in each three dimensions. The average tranvers four-velocity reaches the value of $< u >= 0.55 \pm 0.06$c. It takes surprisingly short time until the particles "freeze-out" compared to earlier estimations based on first-order transition that sometimes exceed the value of 10 fm/c: $\tau_f = 5.9 \pm 0.6$ fm/c. The duration of the emission time is even shorter, $\Delta\tau = 1.5 \pm 1.6$ fm/c. [Ste99, Csö99, Ste99b]

4. I have found indications that the quarks are deconfined from their bound states in the nucleons in Au+Au collisions at RHIC and they behave like independent strongly interacting particles characterizable by an average lifetime of 6 fm/c. For the investigation, I have used data of published single particle spectra and two particle correlations of 4 collaborations of BRAHMS,

PHENIX, PHOBOS, and STAR that were measured in central collisions of energy $\sqrt{s_{NN}} = 130$ GeV. I have applied the Buda-Lund hydrodynamical model for the description of the data. This model works well both at RHIC and at CERN SPS, i.e. it gives good quality descriptions for the transvers mass dependence of the correlation fuction radii. It is remarkable achievment, because in the literature there are about 50 theoretical articles that are unable to interpret these data within errors. According to my results the Buda-Lind model predictions agree the best with the data when the temperature of the innermost 1/8 of the reaction zone reaches $T = 214 \pm 7$ MeV that is substantioanally higher than the critacal temperature of the phase tranzition obtained from lattice QCD calculation, $T_c \simeq 170$ MeV [Csö02b, Csa04a] .

5. I have analysed the data of RHIC Au+Au collisions at higher energy of $\sqrt{s_{NN}} = 200$ GeV, too. For the analysis, I have used data of single particle spectra, two particle correlations and pseudorapidity distributions of charged particles measured by the collaborations BRAHMS and PHENIX. Since the correlation measurements cover the 0-30% centrality class I have averaged the single particle spectra meausured in finer centrality classes to this centrality class. Afterwards, applying the Buda-Lund hydrodynamical model I have fitted the data simultaneously. This way, I have determined the hydrodynamical characteristics of the reactions with high confidence level [a-10]. I have determined, that in the middle of the reaction zone the temperature took the value of $T = 200 \pm 9$ MeV that is 3 sigma higher than the characteristical $T_c \simeq 170$ MeV value of lattice QCD calculations (assuming zero bariochemical potential and a continueos transition similar to the Mott one). In addition, I have determined that the average value of the bario-chemical potential is low, $\mu_B = 61 \pm 40$ MeV. This means, we are well below the level of $\mu_B \approx 300$ MeV where the critical temperature can by considered nearly flat according to lattice QCD calculations [Fod04]. This is also an indicative result since for the the existance of the new phase I have concluded from comparisions to lattice QCD calculation rather than directly from the data.

I have shown that the space-time rapidity width is 30% bigger than at the lower RHIC energy, but in case of other parameters the characteristics of the final states of the hadron creation do not show significant difference [Csa04b].

6. I have justified that at the RHIC Au+Au experiments of the two different energies the characteristics of the observed particle flow agree with the 3 dimentional Hubble flow within errors, i.e. $u^\mu \simeq x^\mu/\tau$. Replacing the flow profile in the Buda-Lund model calculations with the Hubble one I could have reproduced the earlier results. It was predicted by the modef if the Hubble flow becomes independent of directions then the transvers mass dependence of the two particle correlation function (HBT) radii, the slope of this dependence will be the same in each direction. I have shown that within errors this condition was fulfilled for the transvers radii components at both RHIC energies. I have shown this by extrapolating the transvers mass dependence of the inverse HBT radii squares $1/R^2$ to the $m_t = 0$ point. I have calculated that the above condition for the longitudinal component is partially fulfilled, therefore the rapidity dependence of the sigle particle spectra is still relevant [Csa04b, Csa04c].

7. I have analysed the data of $p + p$ reactions of 200 GeV center of mass energy at RHIC. I have simultaneously fitted Buda-Lund model predictions to single particle spectra and two particle correlation data measured by the STAR collaboration. I have compared the results to the ones I obtained from the analyses of Au+Au reactions and to the values I obtained from the analyses of CERN SPS Pb+Pb collisions and to those calculated by the NA22 collaboration analysing hadron+p reactions. I have determined that the central temperature in $p + p$ collisions of 200 GeV at RHIC is far the highest, $T = 289 \pm 8$ MeV. But its value rapidly drops in space and time, already from $R = 1.2$ fm és $\tau = 1.1$ fm/c [Csö04b]

Acknowledgement

Thanks to my family for understanding and supporting me.

Thanks to my supervisor Tamás Csörgő. Without him this work would not have been able to be completed.

Thanks to all my colleagues for professional support. Let me thank all of my coauthors members of the PHENIX collaboration for the excellent common work.

In particular, I thank Professor Bill Zajc and Gábor Dávid for the opportunity to join PHENIX and RHIC currently the most respected physical event in the world. I also thank for the contributions to hospitality at BNL

I especially thank Professor Bengt Lörstad for the help and discussions we have had and for the hospitalities at the University of Lund.

This work was partially supported by the Hungarian NSF grants OTKA - T016206, T024094 and T026435, by the IAESTE exchange programme and by the OTKA-NWO grant N25487 as well as by the US- Hungarian Joint Fund MAKA 652/1998, and by a travel grant from the SOROS fundation.

This work was supported by following grants: OTKA T034269, T038406, the OTKA-MTA-NSF grant INT0089462, the NATO PST.CLG.980086 grant and the exchange program of the Hungarian and Polish Academy of Sciences.

Bibliography

[Ack01] K.H. Ackermann et al, Phys. Rev. Lett. **86** (2001) 402.

[Ada05] J. Adams *et al.* [STAR Collaboration], Nucl. Phys. A **757**, 102 (2005) [arXiv:nucl-ex/0501009].

[Ada06] A. Adare, ..., A. Ster *et al.* [PHENIX Collaboration], Phys. Rev. Lett. (2007) in press, [arXiv:nucl-ex/0608033].

[Adc00] K. Adcox, ..., A. Ster *et al.* [PHENIX Collaboration] Phys. Rev. Lett. **86**, 3500 (2001) [arXiv:nucl-ex/0012008].

[Adc01a] K. Adcox *et al.* [PHENIX Collaboration], Phys. Rev. Lett. **88** (2002) 242301

[Adc01b] K. Adcox, ..., A. Ster *et al.* [PHENIX Collaboration] Phys. Rev. Lett. **87**, 052301 (2001) [arXiv:nucl-ex/0104015].

[Adc02a] K. Adcox *et al.* [PHENIX Collaboration], Phys. Rev. Lett. **88** (2002) 192302

[Adc02b] K. Adcox, ..., A. Ster *et al.* [PHENIX Collaboration], Phys. Lett. B **561**, 82 (2003) [arXiv:nucl-ex/0207009].

[Adc04] K. Adcox *et al.* [PHENIX Collaboration], Nucl. Phys. A **757**, 184 (2005) [arXiv:nucl-ex/0410003].

[Adl00] C. Adler et al., Nucl. Instr. And Meth. A470, 488 (01), nucl-ex/0008005.

[Adl01a] C. Adler *et al.* [STAR Collaboration], Phys. Rev. Lett. **87** (2001) 082301

[Adl03a] S. S. Adler *et al.* [PHENIX Collaboration], nucl-ex/0305013.

[Adl03b] S. S. Adler *et al.* [PHENIX Collaboration], nucl-ex/0307022.

[Adl03c] S. S. Adler, ..., A. Ster *et al.* [PHENIX Collaboration], Phys. Rev. Lett. **91**, 072301 (2003) [arXiv:nucl-ex/0304022].

[Adl04a] S. S. Adler *et al.* [PHENIX Collaboration], nucl-ex/0401003.

[Aga97] N. M. Agababian *et al.* [EHS/NA22 Coll.], Phys. Lett. B **422** (1998) 359

[Agu01] C.E. Aguiar, T. Kodama, T. Osada, Y. Hama, J. Phys. **G27** (2001) 75-94.

[Agu02] C.E. Aguiar, Y. Hama, T. Kodama, T. Osada, Nucl. Phys. **A698** (2002) 639-642.

[Akk01] S. V. Akkelin, T. Csörgő, B. Lukács, Y. M. Sinyukov, M. Weiner, PLB **505**, 64 (2001)

[Aok06] Y. Aoki, Z. Fodor, S.D. Katz, K.K. Szabo, JHEP 0601 (2006) 089

[App98] H. Appelshauser et al, NA49 Collaboration, Eur. Phys. J. **C2** (1998) 661 - 670

[App98b] H. Appelshauser et al.[NA49 Collaboration], Eur. Phys. J. A2, 383 (1998)

[App99] H. Appelshauser et al, Phys. Rev. Lett. **82** (1999) 2471; NA49 note 150.

[Ars04] I. Arsene *et al.* [BRAHMS Collaboration], Nucl. Phys. A **757**, 1 (2005) [arXiv:nucl-ex/0410020].

[Bäc99] J. Bächler et al, Nucl. Phys. **A661** (1999) 341c.

[Bac01] B. B. Back *et al.* [PHOBOS Collaboration], Phys. Rev. Lett. **87** (2001) 102303

[Bac02] B. B. Back *et al.* [PHOBOS Coll.], Phys. Rev. Lett. **89**, 222301 (2002)

[Bac04] B. B. Back *et al.*, Nucl. Phys. A **757**, 28 (2005) [arXiv:nucl-ex/0410022].

[Bal98] A. J. Baltz C. Chasman and S. White, Nucl. Instr. And Meth. A417, 1 (98), nucl-ex/9801002

[Bea97] I.G. Bearden et al, Phys. Rev. Lett. **78** (1997) 2080; Phys. Rev. **C58** (1998) 1656.

[Bea01] I. G. Bearden *et al.* [BRAHMS Collaborations], Phys. Lett. B **523** (2001) 227

[Bea02] I. G. Bearden *et al.* [BRAHMS Collaboration], Phys. Rev. Lett. **88** (2002) 202301

[Bir00a] T.S. Biró, Phys. Lett. **B474** (2000) 21-26.

[Bir00b] T.S. Biró, Phys. Lett. **B487** (2000) 133-139.

[Bjo83] R. C. Hwa, Phys. Rev. **D10** (1974) 2260,
C. B. Chiu and K.-H. Wang, Phys. Rev. **D12** (1975) 272,
C. B. Chiu, E. C. G. Sudarshan and K.-H. Wang, Phys. Rev. **D12** (1975) 902
M. I. Gorenstein, V. I. Zhdanov and Yu. M. Sinyukov, Sov. Phys. JETP **47** (78) 435.
K. Kajantie and L. D. McLerran, Phys. Lett. B **119** (1982) 203.
K. Kajantie and L. D. McLerran, Nucl. Phys. B **214** (1983) 261.
J.D. Bjorken, Phys. Rev. **D27** (1983) 140.

[Bol93] J. Bolz et al, Phys. Rev. D **47**, 3860 (1993)

[Bon78] J. Bondorf, S. Garpman and J. Zimányi, Nucl. Phys. **A296** (1978) 320.

[Bro01] W. Broniowski and W. Florkowski, Phys. Rev. Lett. **87** (2001) 272302 [arXiv:nucl-th/0106050].

[Bro02] W. Broniowski, A. Baran and W. Florkowski, AIP Conf. Proc. **660** (2003) 185

[Cha95] S. Chapman, P. Scotto and U. Heinz, Heavy Ion Physics **1**, 1 (1995); Phys. Rev. Lett. **74**, 4400 (1995)

[Cha95b] S. Chapman, J. R. Nix, U. Heinz, Phys. Rev. C **52**, 2694 (1995)

[Cha98] S. Chapman and J. Rayford Nix, Phys. Rev. **C54** (1996) 866; J. Rayford Nix, Phys. Rev. **C58** (1998) 2303

[Chi02] M. Chiu et al. Phys. Rev. Lett. 89 (02) 012302

[Csa03b] M. Csanád, T. Csörgő and B. Lörstad, nucl-th/0310040.

[Csa04a] M. Csanád, T. Csörgő, B. Lörstad, A. Ster, Act. Phys. Pol. B**35**, 191 (2004)

[Csa04b] M. Csanád, T. Csörgő, B. Lörstad and A. Ster, J. Phys. G30 **S1079-S1082** (2004)

[Csa04c] M. Csanád, T. Csörgő, B. Lörstad and A. Ster, Nukleonika **49** S49-S55, 2004, [arXiv:nucl-th/0402037].

[Csa05] M. Csanad, T. Csorgo, A. Ster, B. Lorstad, N. N. Ajitanand, J. M. Alexander, P. Chung, W.G. Holzmann, M. Issah, R. A. Lacey, A. Taranenko nucl-th/0512078

[Csi98] P. Csizmadia, T. Csörgő and B. Lukács, Phys. Lett. **B443** (1998) 21; nucl-th/9805006.

[Cse94] L.P. Csernai, Introduction to Relativistic Heavy Ion Collisions, John Wiley and Sons, 1994.

[Cse95] L. P. Csernai and I. N. Mishustin, Phys. Rev. Lett. **74** (1995) 5005

[Cse99] L.P. Csernai and D. Röhrich, Phys. Lett. **B458** (1999) 454; nucl-th/9908034.

[Csö91] T. Csörgő and S. Pratt, preprint KFKI - 1991 - 28/A, p. 75

[Csö94a] T. Csörgő, B. Lörstad and J. Zimányi, Z. Phys. C **71** (1996) 491

[Csö94b] T. Csörgő, B. Lörstad, J. Zimányi Phys. Lett. B **338**, 134 (1994)

[Csö94c] T. Csörgő and L. P. Csernai, Phys. Lett. **B333** (1994) 494

[Csö95a] T. Csörgő and B. Lörstad, Phys. Rev. C **54** (1996) 1390

[Csö95b] T. Csörgő and B. Lörstad, Nucl. Phys. A **590** (1995) 465C

[Csö95e] T. Csörgő, Phys. Lett. B **347**, 354 (1995)

[Csö96b] T. Csörgő and B. Lörstad, Heavy Ion Physics **4**, 221 (1996).

[Csö96c] T. Csörgő, P. Lévai and B. Lörstad, Acta Phys. Slovaka **46**, 585 (1996)

[Csö97] T. Csörgő, Phys. Lett. B **409**, 11 (1997)

[Csö98] T. Csörgő, nucl-th/9809011.

[Csö99] T. Csörgő, B. Lörstad, J. Schmid-Sorensen and A. Ster, *"Partial coherence in the core/halo picture of Bose-Einstein n-particle correlations,"* Eur. Phys. J. C **9**, 275 (1999) [arXiv:hep-ph/9812422].

[Csö01] T. Csörgő, S.V. Akkelin, Y. Hama, B. Lukács, Yu.M. Sinyukov Phys.Rev. C67 (2003) 034904

[Csö01b] T. Csörgő, hep-ph/0111139.

[Csö01c] T. Csörgő, S.V. Akkelin, Y. Hama, B. Lukács and Yu.M. Sinyukov, hep-ph/0108067.

[Csö02] T. Csörgő, Heavy Ion Phys. **15** (2002) 1, hep-ph/0001233.

[Csö02b] T. Csörgő and A. Ster, Heavy Ion Phys. **17** (2003) 295

[Csö02c] T. Csörgő and J. Zimányi, Heavy Ion Phys. **17**, 281 (2003)

[Csö02d] T. Csörgő, F. Grassi, Y. Hama and T. Kodama, hep-ph/0203204; hep-ph/0204300.

[Csö03] T. Csörgő, L. Csernai, Y. Hama, T. Kodama, nucl-th/0306004.

[Csö04] `http://www.kfki.hu/~csorgo/budalund/budalund1.5.qm04.tar.gz`

[Csö04b] T. Csörgő, M. Csanád, B. Lörstad and A. Ster, Acta Phys. Hung. A **24**, 139 (2005) [arXiv:hep-ph/0406042].

[Csö07b] T. Csörgő, M. I. Nagy and M. Csanád, Braz. J. Phys. (2007) in press, [arXiv:nucl-th/0702043].

[Dan01] P. Danielewicz, Nucl. Phys. **A685** (2001) 368.

[Fod02] Z. Fodor and S. D. Katz, JHEP **0203** (2002) 014

[Fod04] Z. Fodor and S. D. Katz, JHEP **0404** (2004) 050

[Gea93] GEANT Detector description and simulation tool, Application Software Group, CERN Program Library Long Writeup D **5013** (1993)

[Gra95] F. Grassi, Y. Hama and T. Kodama, Phys. Lett. **B355** (1995) 9, Z. Phys. C **73** (1996) 153.

[Gyu84] M. Gyulassy and T. Matsui, Phys. Rev. **D29** (1984) 419

[Hel97] J. Helgesson, T. Csörgő, M. Asakawa and B. Lörstad, Phys. Rev. **C56** (1997) 2626.

[Jde78] J.N. De, S.I.A. Garpman, D. Sperber, J.P. Bondorf and J. Zimányi, Nucl. Phys. **A305** (1978) 226.

[Lan53] L.D. Landau, Izv. Akad. Nauk SSSR **17** (1953) 51; S.Z. Belenkij and L.D. Landau, Usp. Fiz. Nauk **56** (1955) 309; in "Collected papers of L.D. Landau" (ed. D. Ter-Haar, Pergamon, Oxford, 1965) p. 569-585 and p. 665-700.

[1] P. Lévai and U. Heinz, Phys. Rev. **C57** (1998) 916;
A. Peischer, B. Kämpfer, G. Soff, Phys. Rev. **C61** (2000) 045203;
A. Peischer, B. Kämpfer, G. Soff, Phys. Rev. **D66** (2002) 094003;
A. I. Tóth and K. K. Szabó, hep-ph/0302255.

[Lis00] M.A. Lisa, U. Heinz and U.A. Wiedemann, Phys. Lett. **B489** (2000) 287; nucl-th/0003022; M. A. Lisa et al, E895 Collaboration, Nucl. Phys. **A661** (1999) 444c.

[Kha54] I.M. Khalatnikov, Zhur. Eksp. Teor. Fiz. **27** (1954) 529; see also [Lan53].

[Man02] S. Manly *et al.* [PHOBOS Collaboration], Nucl. Phys. A**715**, 611 (2003)

[Min92] MINUIT Reference Manual v 92.1, Application Software Group, CERN Program Library Long Writeup D **506** (1992)

[Mis96] D. Miskowiecz, talk given at the HBT'96 conference (ECT*, Trento, Italy, September 1996)

[Nic97] S. Nickerson, T. Csörgő and D. Kiang, Phys.Rev. C57 (1998) 3251-3262, nucl-th/9712059,

[Pod83] M. I. Podgorestskii, Sov. J. Nucl. Phys. **37**, 272 (1983)

[Ret03] F. Retiere and M. A. Lisa, Phys.Rev. C70 (2004) 044907, arXiv:nucl-th/0312024.

[Rio06] M. Riordan and W. A. Zajc, Sci. Am. **294N5**, 24 (2006) [Spektrum Wiss. **2006N11**, 36 (2006)].

[Ros98] L. Rosselet, WA98, private comm., http://www.qm99.to.infn.it/paral2/ster/ster.html

[Sin94] Yu. M. Sinyukov, Nucl. Phys. **A566** (1994) 589c .

[Sin02] Yu. M. Sinyukov, S. V. Akkelin and Y. Hama, Phys. Rev. Lett. **89** (2002) 052301

[Ste98] A. Ster, T. Csörgő and B. Lörstad, hep-ph/9809571

[Ste99] A. Ster, T. Csörgő and B. Lörstad, hep-ph/9810341, Heavy Ion Phys. (1999); Proc. Correlations and Fluctuations '98 (World Sci., 1999, ed. T. Csörgő et al.) p. 137

[Ste99b] A. Ster, T. Csörgő and B. Lörstad, Nucl. Phys. A **661** (1999) 419

[Ste00] A. Ster,
How to run ZDC simulation in PISA,
PHENIX internal analysis note 478 (2000).

[Van98] S. E. Vance, T. Csörgő and D. Kharzeev, nucl-th/9802074, Phys. Rev. Lett. **81** 2205 (1998).

[Vol96] S. A. Voloshin and W. E. Cleveland, Phys. Rev. C **54**, 3212 (1996)

[Yan78] F.Yano, S. Koonin, Phys. Lett. B **78**, 556 (1978)

[Wie98] U.A. Wiedemann, Phys. Rev. **C57** (1998) 266; H. Heiselberg and A. Levy, Phys. Rev. **C59** (1999) 2716.

[Wu98] Y. F. Wu, U. Heinz, B. Tomasik, U. A. Wiedermann, Eur. Phys. J. C **1**, 599 (1998)

Összefoglaló

1. Kidolgoztam és végrehajtottam a RHIC PHENIX Au+Au kísérletei számára a Zero Degree Calorimeter (ZDC) GEANT detektor szimulációit. Kidolgoztam egy koaleszcencia modellt, NA49 adatok alapján, az ütközésekben részt nem vevő, spektátor fragmentumok (p, n, d, He, ..) koaleszcenciájának leírására [Ste00], ami a ZDC jelének megjóslásához szükséges. Az Au+Au ütközések centralitás osztályokba sorolását alkalmazva, számos PHENIX cikket publikáltunk a szakma nagy impakt faktorú folyóirataiban [Adc00, Adc01a, Adc01b, Adc02b, Adl03c].
2. Kidolgoztam és végrehajtottam a RHIC PHENIX Cu+Cu kísérletei számára a Zero Degree Calorimeter (ZDC) GEANT detektor szimulációit. A Cu+Cu ütközések első PHENIX eredményeit az [Ada06] publikáció közli.
3. Rekonstruáltam a CERN SPS Pb+Pb $\sqrt{s_{NN}} = 17.3$ GeV reakcióinak végállapotát a Buda-Lund hidrodinamikai modell segítségével. Megadtam 10^{-15} m és 10^{-23} sec skálán, hogy a hadronok keletkezéskor milyen a folyási kép, azaz az $u^\mu(x)$, a $T(x)$ és a $\mu(x)$ eloszlás, valamint milyen a hadronok keletkezési idejét leíró $H(\tau)$ eloszlás [Ste99,Csö99,Ste99b].
4. Indikációt találtam arra nézve, hogy a RHIC Au+Au ütközésekben a kvarkok kiszabadulnak a nukleonokban kötött állapotukból és 6 fm/c-vel jellemezhető átlagos élettartamig erősen kölcsönható önálló részecskékként viselkednek [Csö02b,Csa04a]].
5. Megvizsgáltam a RHIC Au+Au ütközések adatait magasabb, $\sqrt{s_{NN}} =$ 200 GeV energián is. Megállapítottam, hogy a középpontban a hőmérséklet $T = 200 \pm 9$ MeV értéket ért el, ami 3 szigma értékkel nagyobb, mint a rács QCD számolásokból kiolvasható $T_c \simeq 170$ MeV-es jellemző értéke (nulla bariokémiai potenciálnál, és a Mott átmenethez hasonló folytonos átalakulásnál) [Csa04b].
6. Bebizonyítottam, hogy a két különböző energiájú RHIC Au + Au kisérletben a megfigyelt kollektív részecske áram jellege hibán belül egyezik a 3 dimenziós Hubble folyással, azaz $u^\mu \simeq x^\mu/\tau$ [Csa04b,Csa04c].
7. Analizáltam a RHIC 200 GeV tömegközépponti energiájú p+p reakciók adatait. Megállapítottam, hogy a középponti hőmérséklet ezekben a RHIC 200 GeV-es p+p ütközésekben a legmagasabb, $T = 289 \pm 8$ MeV. Értéke azonban gyorsan esik térben és időben, már $R = 1.2$ fm és $\tau = 1.1$ fm/c értékektől [Csö04b].

Summary

1. I have performed GEANT detector simulations of the Zero Degree Calorimeter (ZDC) for the RHIC PHENIX Au+Au experiments. I have created a coalescence model based on data of NA49 for the description of the distribution of the spectator fragments (p, n, d, He, ...) that do not participate in the collisions [Ste00] in order to estimate the ZDS signal in the simulations. Selecting Au+Au collisions by centrality classes, we have published numerous articles in journals with highest impact factors [Adc00, Adc01a, Adc01b, Adc02b, Adl03c].
2. I have performed the GEANT detector simulations of the Zero Degree Calorimeter (ZDC) for the RHIC PHENIX Cu+Cu experiments. The first results of PHENIX from Cu+Cu collisions were published in [Ada06].
3. I have reconstructed the final state of the CERN SPS Pb+Pb $\sqrt{s_{NN}}$ = 17.3 GeV reactions using the Buda-Lund hydrodynamical model. I have given, on the scale of 10^{-15} m és 10^{-23} sec, how the flow profile looks like when the hadrons are created, i.e. what the distributions of $u^\mu(x), T(x)$ and $\mu(x)$ are like, and what the distribution of $H(\tau)$ that describes the creation time of the hadrons is like [Ste99,Csö99,Ste99b].
4. I have found indications that the quarks are deconfined from their bound states in the nucleons in Au+Au collisions at RHIC and they behave like independent strongly interacting particles characterizable by an average lifetime of 6 fm/c [Csö02b,Csa04a].
5. I have analysed the data of RHIC Au+Au collisions at higher energy of $\sqrt{s_{NN}} = 200$ GeV, too. I have determined, that in the middle of the reaction zone the temperature took the value of $T = 200 \pm 9$ MeV that is 3 sigma higher than the characteristical $T_c \simeq 170$ MeV value of lattice QCD calculations (assuming zero bariochemical potential and a continueos transition similar to the Mott one) [Csa04b].
6. I have justified that at the RHIC Au+Au experiments of the two different energies the characteristics of the observed particle flow agree with the 3 dimentional Hubble flow within errors, i.e. $u^\mu \simeq x^\mu/\tau$ [Csa04b,Csa04c].
7. I have analysed the data of p+p reactions of 200 GeV center of mass energy at RHIC. I have determined that the central temperature in p+p collisions of 200 GeV at RHIC is far the highest, $T = 289 \pm 8$ MeV. But its value rapidly drops in space and time, already from $R = 1.2$ fm és $\tau = 1.1$ fm/c [Csö04b].